Evidence of partial melting in metabasic and meta-andesitic rocks from the Highland Complex, Sri Lanka

Abstract

Partial melting of metamorphic rocks is a common phenomenon in high-temperature zones of mountain belts and its products have been observed in many Precambrian basement areas. While granulites of the Highland Complex of Sri Lanka have been widely studied, remelting of metabasites in the Highland Complex has not yet been documented. Building on the UHT conditions reported in the literature, the aim of this study is to demonstrate whether a set of metabasites and meta-andesites from the Highland Complex, Sri Lanka, record evidence for partial melting. These metabasites and meta-andesites comprise garnet-pyroxene-feldspar-amphibole/biotite granulites with leucosomes parallel to the gneissic layering. Detailed petrographic analysis combined with microprobe and trace element data shows dehydration reactions to have occurred. These reactions induced the formation of a tonalitic melt (now leucosome), together with the peritectic minerals garnet, clinopyroxene, orthopyroxene and K-feldspar. Formation of melt is also supported by the loss of albite at triple points and grain boundaries of plagioclase. Relative enrichment of Rb and Ba into leucosomal K-feldspar and Ba and La into leucosomal quartz provide further evidence for melting. Peak metamorphism was reached at 810 – 925 °C and pressures of 8 – 9.8 kbar (dependent on sample), based on geothermobarometry and Perple_X modelling. Zircon analysis by both CL (cathodoluminescence) and LA-ICP-MS shows the onset of partial melting induced partial dissolution of xenocrystic zircons. Furthermore, the crystallization of melt caused the formation of new zircons and the overgrowth of older cores with low trace element concentrations. Additionally, euhedral biotite grains with a relatively low Ti concentration are formed during melt crystallization. Analyses of Th/U values combined with textural observations in zircons infer a single long metamorphic event, with 585 ± 10 Ma as the timing just after peak metamorphism and 536 ± 6 Ma as the timing of final crystallization of melt.

Merijn van Logtestijn

Supervisors:

Dr. L.M. Kriegsman, Naturalis and UU

Prof. Dr. M.R. Drury, UU

1 Introduction

Partial melting of metamorphic rocks is a common phenomenon in high-temperature zones of mountain belts and its products have been observed in many Precambrian basement areas. Together with melt loss, partial melting is fundamental to crustal differentiation. Partial melting and melt loss cause the creation of a largely mafic and minimally hydrated lower crust and a more felsic and hydrated upper crust (e.g. Brown & Rushmer 2006). While partial melting is reported frequently in metapelites and quartzo-feldspathic rocks (e.g. Breton & Thompson 1988; Stevens et al. 1997; Bea & Montero 1999; Sawyer, 2008), petrological studies with evidence for remelting of rocks with a mafic crustal protoliths are rare (Sawyer 1991; Johnson et al. 2012; Kunz et al. 2014). The reason for this is partly due to the much higher temperatures needed to produce significant quantities of melt in metabasites relative to e.g. metapelites, especially when external fluids are absent (e.g. Rushmer 1991).

Tonalitic to trondhjemitic melts have been generated in a variety of higher temperature (>900 °C) experiments on mafic protoliths (Johnston 1986; Beard & Lofgren 1991; Rapp et al. 1991; Rushmer 1991; Sen & Dunn 1994; Wolf & Wyllie 1994; Rapp 1995; Springer & Seck 1997; Sisson et al. 2005). These kinds of experiments have produced peritectic phases such as garnet and orthopyroxene. Geochemical evidence suggests that melting of hydrated basalts in the presence of garnet can explain massive TTG gneisses in the Archaean (e.g., Taylor & McLennan 1995; Kröner 1985; Jahn et al. 1988; Rapp et al. 1991; Foley et al. 2002), so at least in that period it must have been a very common process. Minerals like garnet, rutile, biotite and amphibole are known to induce strong fractionation of inter alia the rare earth elements (REE) when partial melting occurs.

The pelitic granulites of the Highland Complex of Sri Lanka have been widely studied (e.g. Osanai et al. 2006; Faulhaber & Raith 1991; Kriegsman & Schumacher 1999; Sajeev & Osanai 2004; Sajeev & Osanai 2005; Hiroi et al. 1994; Raase & Schenk 1994), whereas detailed petrological studies of mafic granulites are less common and are focused on geothermobarometry (e.g. Faulhaber & Raith 1991; Faulhaber, R. Schumacher 1994; Sajeev et al. 2007; Takamura et al. 2015). While remelting of metabasites in the Highland Complex has not yet been documented by these authors, studies of partial melting in metabasites of other areas of the world have been performed (e.g. Sawyer 1991; Nehring et al. 2009; Johnson et al. 2012; Kunz et al. 2014) and have led to a good understanding of the P-T conditions required. These studies are key to gaining a better understanding of the formation of the early continental crust. In addition, remelting of metabasites can reconciliate the dominance of mafic melts in many settings with the overall felsic to intermediate composition of the continental crust (e.g., Taylor & McLennan 2010), especially when combined with delamination of the dense restite.

Building on the UHT conditions reported in the literature, the aim of this study is to demonstrate whether a set of metabasites and meta-andesites from the Highland Complex, Sri Lanka, record evidence for partial melting. These metabasites and meta-andesites comprise garnet-pyroxene-feldspar-amphibole/biotite granulites with leucosomes parallel to the gneissic layering. We follow the hypothesis that the leucosome, which is tonalitic in composition, has originated via partial melting processes. Evidence to support this finding should come from linking and comparing petrographical, mineralogical and geochemical data together with P-T modelling data. Based on mineral textures and microprobe analyses, prograde, peak and retrograde minerals can be identified. Combining petrographical data, mineralogical compositions, models and trace element data will provide multiple lines of data to be able to draw constructive conclusions about the origin of the leucosome. Furthermore, zircon U/Pb dating will be used to constrain the time window.

Evidence for partial melting in high-grade metamorphic rocks can come from various sources. Firstly, petrographic textures can provide information about possible dehydration reactions which can only be

balanced in the presence of melt. Microprobe analysis and mapping can support these textures and reactions chemically. Moreover, mineral composition from microprobe analysis can be used to calculate pressure and temperature conditions of multiple assemblages present in the rock. This method relies on chemical equilibrium between different minerals in a single assemblage. Calculating P-T conditions can be done by both geothermobarometry and chemical modelling. However, it may be ineffective to use major elements to monitor partial melting processes in high-grade rocks. Fe-Mg exchange reactions and similar continuous reactions are easily reset during retrograde processes, whereas solvus thermometry and discontinuous reactions involving breakdown of phases are more reliable. Major elements may thus re-equilibrate during peak and retrograde conditions, destroying compositional evidence of the earlier history of the rock (e.g. Tracy, 1982). This is especially true for retrograde melt-consuming reactions (e.g., Kriegsman & Hensen 1998; Cenki et al. 2002). Recent studies show trace elements, such as the Rare Earth Elements (REE), to be better suited to provide information about high-grade metamorphic processes (Otamendi et al. 2002; Hermann & Rubatto 2003). This is supported by experimental studies which indicate diffusion of elements has a large dependence of ionic charge: trivalent REE diffuse at least two orders of magnitude slower than divalent elements such as Mg and Fe (Van Orman et al. 2002). Trace element data from LA-ICP-MS analysis can also be used to study partitioning of elements. In a system composed of mesosome/melanosome and leucosome, compatible elements will partition into the melanosome, if considered as restite, whereas incompatible elements will partition into the melt. Both elements with a high ionic radius and elements with a high ionic charge are incompatible, as they are not easily incorporated into the crystal structure of most minerals. Incompatible elements include the High Field Strength Elements (HFSE) and the Large Ion Lithophile Elements (LILE).

1.2 Geological setting

Sri Lanka formed a small but essential part of the Gondwana supercontinent (figure 1), as the island was located close to East Antarctica, India, Madagascar and East Gondwanaland (e.g. Kriegsman 1995). Due to this position, Sri Lanka has been in focus to give insights into the history of the assembly of supercontinents in general and Gondwana in particular (Kriegsman 1993; Kriegsman 1995; Braun & Kriegsman 2003. The widely accepted classification of Cooray (1994), subdivides its Precambrian metamorphic basement into four major complexes: the Wanni Complex (WC) in the west and northwest, the Highland Complex in the center and south, the Kadugannawa Complex (KC) in the center between the WC and the HC, and the Vijayan Complex (VC) in the east (figure 1). This division is largely based on Nd-model age mapping and regional structural interpretations (Milisenda et al. 1988; Milisenda et al. 1994; Kröner & Williams 1993).

The oldest part of Sri Lanka is the eastern part of the Highland Complex, which has a 2000-3000 Ma provenance age (Milisenda et al. 1988). The rest of the country has a model (or provenance) age of 1000-2000 Ma, supported by U-Pb zircon ages of multiple studies (e.g. Hölzl et al. 1994; Kröner et al. 1994). The Sri Lankan basement is composed of upper amphibolite- to granulite-facies metamorphic rocks, with the highest grade located in the Highland Complex. These metamorphic rocks record both magmatic events and (high-grade) metamorphism from Early to Late Neoproterozoic events during the assembly of Gondwana, (Kröner et al. 1994; Santosh et al. 2014).

The dominant lithologies in the Highland Complex are metasedimentary rocks, comprising meta-quartzites, marbles, calc-silicates and metapelites, closely associated with meta-igneous rocks, which are mostly charnockites and mafic granulites (e.g. Cooray 1994; Kröner et al. 1994; Braun & Kriegsman 2003). The pressure and temperature conditions of this region have been relatively well studied. A P-T zonation in the HC has been found, which increases from approximately 5-6 kbar and 700 °C in the northwest, to

approximately 9-10 kbar and 830 °C in the southeast (Faulhaber & Raith 1991; Faulhaber & Schumacher 1994). Based on the sequence of kyanite and staurolite, subsequently sillimanite, and finally andalusite in pelitic rocks, a clockwise P-T path is established by multiple studies (Hiroi et al. 1994; Raase & Schenk 1994; Kriegsman & Schumacher 1999). Pigeonite exsolution in meta-igneous rocks suggests (isobaric) cooling prior to uplift (Schenk & Raase 1988; Schumacher et al. 1990), and this stage has recently been supported by late reaction in pelitic rocks (Dharmapriya et al. 2015. Ultrahigh-temperature metamorphism has been reported from several localities, with temperatures of 900-1150 °C and pressures of 9-12.5 kbar (Kriegsman & Schumacher 1999; Malaviarachchi & Dharmapriya 2015; Dharmapriya et al. 2015).

Milisenda et al. 1988 and Milisenda et al. 1994 reported Sm-Nd model ages of 3.4-2.2 Ga in the highland complex. Rb-Sr whole rock indicate ages of around 2 Ga (Hölzl et al. 1994). Garnet-whole rock Sm-Nd data reveal a metamorphic age of ~600 Ma (Hölzl et al. 1991; Milisenda et al. 1991). U-Pb chronology of detrital metasedimentary zircons shows ages of 3.2-2.4 Ga, and meta-igneous rocks show intrusion ages around 1.1 Ga and new zircon growth at 550 Ma (Kröner et al. 1987). Baur et al. 1991 reported U-Pb zircon ages of 1940 Ma, interpreted as magmatic, and a Pb loss event at 560-550 Ma, indicating high-grade metamorphism. Kröner & Williams (1993) found similar ages, namely 1.9 Ga for the crystallization of magmatic zircons and 531 Ma for time of peak metamorphism. Discordant single zircons and zircon fractions gave a lower intercept age of 550-610 Ma in concordia plots, and multigrain fractions of metamorphic zircon, monazite and rutile gave concordant U–Pb and $^{207}Pb/^{206}Pb$ ages of 541–608 Ma (Baur et al. 1991; Hölzl et al. 1994; Kröner et al. 1994). Malaviarachchi & Takasu (2011) reported ages of metamorphism of 728-460 Ma from monazites, but these are based on so-called chemical ages using microprobe measurements and are therefore less reliable than isotopic analyses. In addition, monazite is considered less resistant to partial resetting than zircon (Rubatto et al. 2013). Sajeev et al. 2007 obtained zircon metamorphic ages of circa 580 Ma from metabasites. Sajeev et al. 2010 suggested that (near) peak metamorphism of about 570 Ma is related to a collisional orogeny during the assembly of Gondwana, recorded by zircon overgrowths in quartz-saturated granulites which also record partial melting. This was followed by isothermal decompression during fast extensional exhumation, recorded by 550 Ma zircons and monazites. Santosh et al. (2014) reports 206Pb/238U ages of zircons from the HC from 579 ± 10 Ma up to 511 ± 6 Ma (garnet charnockite) and 553 ± 3 Ma from a mafic granulite, and suggests two thermal events to have occurred. Santosh et al. (2014) also reports Lu-Hf ages of 1847–1978 Ma (metagabbro), and between 2263 and 2790 Ma (mafic granulite), suggesting reworking of Neoarchean-Paleoproterozoic crust. Takamura et al. (2015) reports zircon U–Pb ages of a metagabbro of 574 ± 28 Ma and 534 ± 14 Ma, and also suggests two thermal events to have occurred.

2 Methods

Fieldwork was done by L.M. Kriegsman in the Highland Complex of Sri Lanka in the period 1988-1992 (Kriegsman 1993; Kröner et al. 1994; Kriegsman & Schumacher 1999) and again in the period 2013-2015. Thin and thick sections were prepared at Utrecht University, the Netherlands. Firstly, thin sections were analyzed with optical microscopy. The three most representative and promising samples were selected for further analysis, each with a different chemistry and mineralogy. Mineral abbreviation from Whitney & Evans (2010) are used in this study, which is an updated version of Kretz (1983). Semi-quantitative analyses (EDS) for first order analysis of phases and chemical maps were carried out with a JEOL JSM-7600F at Naturalis Biodiversity Center, Leiden. Quantitative chemical analyses (WDS) were carried out at Utrecht University, using a JEOL JXA-8530F microprobe. The analyses were performed with an accelerating voltage of 15.0 keV and a current of 1.0 nA. Chemical maps were acquired by both the SEM in Leiden and the

microprobe in Utrecht. Element maps were made of the following elements: Si, Al, Fe, Mg, Ca, K, Mn, Na, Ti and Cr. Bulk rock compositions of samples for thermodynamic modeling purposes were attained using image analysis techniques together with microprobe mineralogy data.

Zircon grains were separated from the rock samples in the mineral separation lab at the VU, Amsterdam. Firstly, samples were crushed and sieved into several fractions ranging from 30 to 250 µm. Grains smaller than 30 µm were removed using a wet sieve, as larger grains are needed for analysis. A Carpco roll magnet was used to remove the majority of magnetically susceptible grains. Separation then continued by using heavy liquid separation; a 3.0 $g.cm^{-3}$ solution of diiodomethane was used. To remove residual magnetically susceptible grains, a Franz magnetic separator was used. A 3.3 $g.cm^{-3}$ solution of diiodomethane was used to further remove grains with a density lower than zircon. Finally, zircon grains were purified by hand picking under an optical microscope. Zircon grains were mounted in epoxy resin in fractions of 60-90 µm, 90-120 µm, 120-180 µm and 180-250 µm. The grains were polished to reveal the grain centers. To reveal the zircon grains' internal structure, cathodoluminescence (CL) images were made using the JEOL JXA-8530F microprobe at Utrecht University. The Laser Ablation Inductively Coupled Plasma-Mass Spectrometry (LA-ICP-MS) laboratory of Utrecht University was used for age determination. This lab is equipped with ThermoFischer Scientific Element 2 magnetic sector ICP-MS and a Lambda Physik excimer laser (193 nm) with GeoLas optics. A spot size of 30 µm was used, with a pulse energy of 8.8 J/cm^2 and a repetition rate of 7 Hz. An analysis time of 1 minute and 30 seconds was used, of which 30 seconds with the laser off was used for the gas blank and a minute for laser ablation. The zircon standard ZR91500 was used for quantification.

Thick sections (80-100 µm) were made for trace element analysis. The same LA-ICP-MS laboratory was used for trace element analysis (see above). A spot size of 60 µm was used, with a pulse energy of 8.8 J/cm^2 and a repetition rate of 10 Hz. The analysis time was 2 minutes and 30 seconds, of which 1 minute was used for the gas blank and a minute and a half for laser ablation. For quantification, the following standards were used: NIST SRM 612 (trace elements in glass) and BRC-2G (basaltic glass).

3 Results

3.1 Petrology

A description of the petrological features and mineralogy of the samples analyzed in this study is given below. Mineralogy of the samples is given in table 1. Representative mineral compositions from electron microprobe analyses are given in tables 2 and 3. In this study three samples are discussed in detail. The first, sample 787, is intermediate in composition and is classified as a meta-andesite. It contains biotite and K-feldspar, and lacks amphibole, whereas the other samples contain amphibole but lack K-feldspar. The other two samples, 968 and 280, are classified as metabasites.

3.1.1 Sample 787

This sample consists of plagioclase (~36%), quartz (~18%), orthopyroxene (~14%), garnet (~10%), clinopyroxene (~9%) and biotite (~4%). Ilmenite, magnetite, K-feldspar, rutile, zircon and apatite are accessory phases. On the large scale it consists of leucosome and dark bands (interpreted as mesosome by analogy to migmatites). Garnets are porphyroblasts, up to 7 mm diameter in size, surrounded by orthopyroxene + plagioclase symplectites. Plagioclase and orthopyroxene coronas surround the symplectites in most places, particularly where symplectites border leucosomes (see below). This suggest a change from high diffusion rates, when plagioclase and orthopyroxene could form separate layers around the garnet, to

lower diffusion rates, causing the formation of orthopyroxene + plagioclase symplectites. Figure 2 shows the transition from garnet to plagioclase + orthopyroxene symplectites to a plagioclase corona to an orthopyroxene corona. Garnet contains minor inclusions of quartz, plagioclase, apatite, zircon, ilmenite, magnetite and rutile, probably as relict (prograde) minerals (figure 13). K-feldspar, magnetite and ilmenite are also present in the symplectites. The mesosome consists of predominantly intergrown an- to subhedral orthopyroxene, clinopyroxene, biotite and plagioclase (figure 9). Plagioclase inclusions are present in orthopyroxene and clinopyroxene. Plagioclase grains in the mesosome have an increasing anorthite content from core to rim ($Ab_{54}An_{46}$ to $Ab_{48}An_{52}$). As visible in figure 9, the center of plagioclase grains have a relatively uniform composition, and the zonation is predominantly located near triple points of grains. Biotite throughout the mesosome is subhedral, but it is euhedral near symplectites. Fine idiomorphic biotite needles are also present within the symplectite, which may have formed during the reintroduction of fluids during exhumation or during final melt crystallization (rehydration reaction). Coexisting ilmenite and magnetite are present throughout the entire sample (figure 9, 10 and 11), except for the leucosome, typically forming magnetite exsolution lamellae in ilmenite.

In the mesosome well aligned biotite grains separated by pyroxene and plagioclase are abundant (figure 9). Moreover, the relict minerals present as inclusions within garnet porphyroblasts suggest garnet to have grown as a peritectic mineral over preexisting minerals. Plagioclase zoning in the mesosome is consistent with the loss of Ab, which is the plagioclase component with the lowest melting temperature, to a melt phase. Together with the vicinity and abundance of leucosome, this indicates a dehydration reaction. This reaction can produce either subsolidus quartz and feldspar bands or a leucosome (i.e. melt). Although no clear textural evidence of melt has been found, e.g. former melt films, pressure and temperature conditions (see section 3.3 and 3.4) are well above melting conditions, so here the formation of melt is assumed. The following dehydration melting reaction may have caused the formation of garnet porphyroblasts and simultaneous melt:

(1) Bt + Pl + Qtz --> Grt + Melt + Cpx

The orthopyroxene and K-feldspar present in the mesosome may be due to the following reaction:

(2) Bt + Pl + Qtz --> Opx + Kfs + Grt + Melt

Reaction 1 is widely reported as a dehydration occurring in high-grade metamorphic rocks (Weinberg and Hasalová 2015 and references therein). Reaction 2 (Roberts and Finger 1997 and Bhowmik 2014), shows the creation of peritectic K-feldspar. This may be the result of the dehydration reaction of biotite releasing more K_2O than can be accommodated in the melt, therefore forming K-feldspar (Carrington and Watt, 1995). This depends on the K_2O/H_2O ratio of the melt. K-feldspar also exists as an exsolution phase in plagioclase in the mesosome as well as the leucosome (figures 9+12); this was a ternary feldspar at higher temperature that exsolved into plagioclase and orthoclase during cooling.

The abundant symplectites and plagioclase + orthopyroxene coronas suggest the following decomposition reaction of garnet:

(3) Grt + Qtz ± Cpx --> Pl + Opx ± Mt;

Reaction (3) has been reported from many high-grade terranes worldwide (e.g. Harley 1989; Mengel & Rivers 1991; Thost et al. 1991), and suggests near-isothermal decompression or decompressional cooling after the peak metamorphism. Although this reaction does not involve a melt phase, some melt may, however, still be present in the system at high temperatures, which can facilitate reaction progress. The clinopyroxene in this reaction contributed to the formation of minor magnetite in the symplectites, due to

the transfer of ferric iron (Fe^{3+}). It is this equilibrium that has been used extensively for thermobarometry in Sri Lanka (Sandiford et al. 1988; Faulhaber & Schumacher 1994; Faulhaber & Raith 1991; Kriegsman, 1996).

Kfs is found bordering both biotite and garnet in the symplectites (figure 10 and 11), denoting the transfer of K from biotite to Kfs. Another product of the decomposition of biotite is ilmenite, which formed due to the transfer of Ti. Figure 11 shows ilmenite with magnetite exsolution lamellae largely surrounded by orthopyroxene, denoting the transfer of ferric iron from biotite to ilmenite and magnetite. These observations together suggest the following reaction:

(4) Grt + Bt + Qtz => Opx + Ilm ± Mt + Kfs + V/Liq

Due to the breakdown of biotite and the absence of a hydrous phase on the product side of the reaction, this reaction also produces vapor or a liquid. Biotite has a similar X_{Mg} as orthopyroxene, limiting the role of garnet and its decomposition.

A plagioclase-quartz leucosome (+/- 5 mm wide) transects the sample. The leucosome is tonalitic in composition and contains quartz, plagioclase and K-feldspar. It consists of a single broad euhedral quartz band (large grained, up to 2 cm), which splits at the top of the thin section, and feldspar grains adjacent to the quartz band. The feldspar grains have a smaller grain size (<1mm) and have an increasing anorthite content from core to rim, similar to the mesosome. Patches of quartz and Ca-richer plagioclase ($Ab_{25}An_{75}$) are present in the leucosome, as well as with mesoperthites (Kfs blebs - $Ab_{05\text{-}02}An_0K_{95\text{-}98}$). Mesoperthites can be explained by high-T ternary feldspars from which Kfs exsolves when the temperature decreases; a large (>1 cm) mesoperthite patch (70% pl, 30% Kfs) is present at the top of the thin section and smaller mesoperthites occur in the rest of the feldspar band. The quartz band is deformed in a ductile manner in some locations, and is wrapping around a garnet porphyroblast (figure 3).

3.1.2 Sample U968

This sample consists of plagioclase (~50%), quartz (~25%), orthopyroxene (~10%), clinopyroxene (~10%), amphibole (~3%) and garnet (~2%). The high content of plagioclase and quartz is due to the leucosome covering approximately two thirds of the thin section. Rutile, ilmenite, magnetite, zircon and apatite are accessory phases. The mesosome (interpreted by analogy to migmatites) consists of predominantly intergrown an- to subhedral orthopyroxene, clinopyroxene, amphibole and plagioclase (figure 14). Plagioclase inclusions are present in orthopyroxene and clinopyroxene. Plagioclase grains in the mesosome have an increasing anorthite content from core to rim ($Ab_{45}An_{55}$ to $Ab_{28}An_{72}$).

Similar to sample 787, well aligned amphibole grains (instead of biotite) separated by pyroxene and plagioclase are abundant in the mesosome (figure 4). Also, the relict minerals present as inclusions within garnet porphyroblasts suggest garnet to have grown as a peritectic mineral over preexisting minerals. Plagioclase zoning in the mesosome is consistent with the loss of Ab, which is the plagioclase component with the lowest melting temperature, to a melt phase. Together with the vicinity and abundance of leucosome, this indicates a dehydration reaction. This reaction can produce either subsolidus quartz and feldspar bands or a leucosome (i.e. melt). Although no clear textural evidence of melt has been found, e.g. former melt films, pressure and temperature conditions (see section 3.3 and 3.4) are well above melting conditions, so here the formation of melt is assumed. The following dehydration melting reaction may have caused the formation of garnet porphyroblasts and melt:

(5) Amp + Pl + Qtz = Opx + Cpx + Grt + melt

Reaction 5 is widely reported as a dehydration reaction occurring in high-grade metamorphic rocks (Weinberg and Hasalová 2015 and references therein). This reaction actually consists of two consecutive reactions: first the main pyroxene it produces is clinopyroxene, and at higher temperatures orthopyroxene is the main product (see section 3.3 for details).

The leucosome comprises the bottom 2/3 of the thin section and is tonalitic in composition. It consists of alternating bands of quartz and plagioclase. The quartz band (ribbon) has a large grain size (up to 2 cm) and the feldspar band a smaller grain size (<1 mm). In contrast to the mesosome, plagioclase grains in the leucosome have a decreasing anorthite from core to rim ($Ab_{45}An_{55}$ to $Ab_{49}An_{51}$). Garnet porphyroblasts are "suspended" in the leucosome. The leucosome bends around the garnet porphyroblasts where present. A sheared quartz band is also present in the leucosome, indicating minor later deformation.

Garnet is only present in the leucosome, although orthopyroxene + plagioclase pseudomorphs after garnet occur in the mesosome. Garnets are completely surrounded by plagioclase and orthopyroxene symplectites and an orthopyroxene corona, which formed due to reaction (3), the same reaction as in sample 787 (figures 5+15). Magnetite is also present in the symplectites. Inclusions in garnet are similar to those in sample 787.

3.1.3 Sample U280

Amphibole comprises most of this sample (+/-41%), the remaining consists of mostly plagioclase (~25%), quartz (~17%) and garnet (~5%). Most garnet porphyroblasts have been decomposed to predominantly plagioclase, orthopyroxene and magnetite, although some garnet porphyroblasts have remained largely intact (figure 17). The mesosome consists of mostly amphibole with plagioclase and quartz (figure 16.A). Biotite, apatite, magnetite, ilmenite and titanite are present as accessory phases. Plagioclase grains have an increasing anorthite content from core to rim, consistent with preferred breakdown of the Ab component during prograde metamorphism. All amphiboles have a similar composition, and are unzoned. Euhedral biotite needles, which occur predominantly near garnet relicts, have a slightly lower Ti and higher X_{Mg} than larger grains of biotite. Inclusions in amphibole are apatite and quartz. Magnetite exsolution lamellae are present in ilmenite.

Most garnets are relatively small (+/-3mm) and altered, and some pseudomorphs after garnet are present (figure 16.B). Inclusions in garnet are titanite, plagioclase and quartz. These inclusions suggest garnet to have grown as a peritectic mineral over preexisting minerals. Hence, I infer that garnets formed through the following reaction:

(6) Amp + Pl + Qtz ± Bt = Grt + melt ± Ttn

The pseudomorphs after garnet consist primarily of plagioclase and orthopyroxene, but biotite, titanite, amphibole, magnetite and ilmenite are also present. Orthopyroxene and plagioclase rarely form symplectites in this texture, but instead form separate grains, which suggests higher diffusion rates. Titanite is present as very small, anhedral grains. One large (1 cm) garnet porphyroblast is present (figure 17), which is relatively unaltered although it is broken down in cracks across the entire grain. This large porphyroblasts is located in a thin (2 mm wide) quartz and feldspar band in which quartz and plagioclase form a foam texture of relatively small grains (figures 6+7), also seen by the abundant 120° triple junctions. This band is unlike the leucosome in the other samples studied, as it lacks the size and alternating bands of quartz and feldspar. The small grain size together with the relatively undecomposed garnet suggests this former melt zone crystallized later than the larger leucosomes. Thus, garnet occurring in early crystallized melt can

decompose (now seen as the pseudomorphs after garnet, see figures 8 and 16B), whereas breakdown of garnet in the youngest leucosome may have been hampered by declining temperatures.

3.2 Mineral chemistry

Representative mineral compositions from electron microprobe analyses are given in table 2 and 3.

3.2.1 Garnet

Garnet occurs as porphyroblasts in all samples. In samples 787 and 968 symplectites surround garnets; only in sample 968 the symplectites are partly surrounded by orthopyroxene coronas. In sample 280, most garnet is replaced, although large and fragmented porphyroblasts remain with very minor symplectites. Garnet is almandine-rich, with significant pyrope and grossular contents and minor spessartine, which varies depending on difference in assemblage and position in garnet grain. The zonation pattern of garnets in all samples is equivalent, with increasing spessartine and almandine content and decreasing pyrope and grossular content from core to rim. Decreasing grossular towards the rim is consistent with plagioclase growth, and increasing spessartine content is a clear sign of breakdown. As most of the garnet is replaced by other minerals in sample 280, there is little difference in composition between core and rim in this sample. Minor biotite, K-feldspar, apatite, magnetite and ilmenite are also present in the symplectites. Inclusions in garnet are: quartz, plagioclase, apatite, zircon, ilmenite and rutile. Titanite occurs as inclusions in garnet only in sample 280.

3.2.2 Feldspars

Plagioclase shows a high variation in composition depending on textural setting and within single crystals, also depending on the assemblage. Plagioclase is found in the mesosome of all samples, where it is often zoned. This zonation is observed primarily near the edges and at triple points of crystals, rather than gradually from core to rim. In sample 787, exsolved ternary feldspars occur in the mesosome (figure 9). In symplectites, single plagioclase crystals are often zoned similarly to the mesosome plagioclase. The zonation pattern is similar in the mesosome and symplectites of all samples: plagioclase shows an increasing anorthite content from core to rim in the mesosome and a decreasing anorthite content from the garnet side to the other side of the symplectitic domain. However, the anorthite content decreases from core to rim in plagioclase grains located in the leucosome of sample 968, while in sample 787 the anorthite content increases from core to rim in leucosome plagioclase. See section 4.1.2 for a detailed discussion on plagioclase zoning.

K-feldspar is only found in sample 787, where it occurs as patches exsolved from ternary feldspars in the mesosome, and as mesoperthites in the leucosome. Furthermore, it is found bordering both biotite and garnet in symplectites.

3.2.3 Pyroxenes

Orthopyroxene has an X_{Mg} of 0.48-0.65. In sample 787, orthopyroxene has an X_{Mg} of 0.57, varying slightly throughout the sample, while the X_{Mg} of orthopyroxenes in symplectites and coronas in sample 968 is slightly lower than in those in the mesosome (0.60 and 0.65 respectively). In sample 280 orthopyroxene is present only in minor amounts, and has the lowest X_{Mg} (0.48) of all samples. The Al content in the mesosome is 0.08

and 0.07 p.f.u. in samples 787 and 968 respectively. In the symplectites the Al content in sample 787 and 968 is 0.08-0.15 p.f.u. and 0.10-0.15 p.f.u. respectively. This concentration varies locally, and is generally larger near garnet porphyroblasts. In sample 280, the Al content is the lowest with 0.05 p.f.u. There is no compositional variation in single grains.

All clinopyroxenes are classified as augite, as their Na content is very low and their composition mainly varies between samples in X_{Mg} value. X_{Mg} is circa 0.68 in sample 787 and circa 0.75 in sample 968 and does not vary significantly both between various grains nor position in a single grain. Clinopyroxene is not present in sample 280.

3.2.4 Amphibole

Amphibole is a major phase in samples 968 and 280. There is no significant compositional variation between amphiboles in either sample. Amphibole in both samples is high in Ca (1.84-1.77 p.f.u.), and Ti (0.31-0.24 p.f.u.). X_{Mg} in sample 968 is 0.62, and the amphibole in this sample is classified as pargasite. X_{Mg} in sample 280 is 0.48, and the amphibole in this sample is classified as ferro-pargasite.

3.2.5 Biotite

Biotite is present in samples 787 and 280. Biotite in sample 787 occurs in the mesosome (subhedral), as larger grains in and around the symplectites (euhedral) and as fine needles in the symplectites. Biotite in the mesosome is zoned; from the core to the rim the X_{Mg} increases from 0.60 to 0.73 and the amount of Ti p.f.u. decreases from 0.68 to 0.50. The biotite located in the symplectites has a relatively constant X_{Mg} of 0.71 and 0.75 and a Ti content of 0.54 and 0.27 p.f.u., for the larger grains and fine needles respectively. In sample 280, biotite is present mostly near (largely decomposed) garnet grains. It occurs as fine needles and as larger euhedral grains, both similar to the biotite occurring in sample 787.

3.2.6 Accessory phases

Magnetite and ilmenite occurs in all samples, both in the mesosome and in the symplectitic domains. It also occurs as exsolution lamellae in ilmenite in sample 787, whereas in sample 280 ilmenite occurs as lamellae in magnetite. Apatite occurs throughout the mesosome and symplectitic domains in all samples as well. Zircon occurs in small grains throughout the samples, especially as inclusions in garnet. Titanite only occurs in sample 280, both throughout the mesosome and as inclusions in garnet.

3.3 Pressure and Temperature modelling with Perple_X

P-T pseudosections were calculated using Perple_X version 6.6.8 (Connolly 1990, 2002, 2009). Solid solution models of garnet (Holland & Powell 1998), orthopyroxene (Powell & Holland 1999), clinopyroxene (Holland & Powell 1996), melt (Holland & Powell 2001), biotite (Tajčmanová et al. 2009), plagioclase (Newton et al. 1981), feldspar (Benisek et al, 2010), sanidine (Thompson and Hovis 1979), ilmenite coexisting with magnetite (Andersen & Lindsley 1988), olivine (Holland & Powell 1998) and clino- and orthoamphibole (Diener et al. 2011) were used. See table 4 for the composition used as input for the pseudosections.

3.3.1 Sample 787

A pseudosection for this sample is given in figure 18. The X_{Mg} of garnet, orthopyroxene, biotite and clinopyroxene, the X_{An} of feldspar and the Al content of orthopyroxene are plotted over the graph to visualize this samples' phase compositions. Light and dark red shows peak and rim composition of garnet respectively. Of biotite, the X_{Mg} of mesosome (dark orange), symplectite (yellow) and retrograde needles (light orange) are shown. Garnet core, plagioclase core and clinopyroxene compositions cross at about 925 °C and 9.8 kbar, with Opx-Bt-Melt-Fsp-San-Ilm-Grt-Cpx-Qtz as the assemblage in the pseudosection. This may represent (near) peak conditions. Orthopyroxene X_{Mg} crosses this field about 1 kbar lower. This field also fits with reaction 2, as biotite abundance decreases in this field until it is gone at the right side of the field. As not all biotite is consumed, this field fits with the petrological observations. Melt is found in the assemblage from about 870 °C and higher, which is slighter higher than data in e.g. Weinberg & Hasalova (2015) and references therein. As garnet breaks down into orthopyroxene and plagioclase, retrograde conditions may be represented by garnet rim and orthopyroxene conditions, which cross at 840 °C and 8.3 kbar. The composition of feldspar in symplectites cannot be found on this pseudosection, therefore a pseudosection using a local bulk of the patch where garnet broke down is shown in figure 19. This figures gives constrains on the breakdown reaction of garnet. Figure 21, using Al content in Opx together with Opx and plagioclase abundance, shows decomposition of garnet to occur from ~8 kbar and ~780 °C. Decompressional cooling occurs afterwards, as seen from decreasing garnet abundance with lower pressure and change in diffusion rates from coronas to symplectites. As no new rutile growth is observed, the prograde path presumably stays below this border (line runs from 600 °C and 7.8 kbar to 920 °C and 13 kbar). Figure 20.A shows garnet abundance of figure 19, and gives an indication of the prograde path where garnet abundance increases. Figure 20.B shows the gradual increase in clinopyroxene abundance with increasing temperatures, whereas figure 20.C shows the abundance of orthopyroxene stays similar with increasing temperature and rapidly increases near peak conditions.

Biotite composition does not match with the composition of other minerals in the pseudosection, which may be due to its relative complexity in modelling. Orthopyroxene is known to be stable only at relatively high temperature and pressure, while it is present in the entire pseudosection. Moreover, garnet has relatively high abundance as seen in figure 20.A, especially during early prograde and retrograde conditions.

3.3.2 Sample 968

A pseudosection for this sample is given in figure 21. The X_{Mg} of garnet, orthopyroxene and clinopyroxene, the Al content of orthopyroxene and the X_{An} of feldspar are plotted over the graph to visualize this sample's phase compositions as a function of P and T. Light and dark red shows peak and rim composition of garnet respectively. Amphibole compositions obtained from microprobe analysis did not fit the values in this pseudosection. Garnet core, clinopyroxene and feldspar compositions cross at about 875 °C and 9.2 kbar, with Opx-Bt-Melt-Fsp-Ilm-Grt-Cpx-Qtz as the mineral assemblage in the pseudosection. Melt comes into the system at about 790 °C, which is lower than the 850-900 °C suggested in Weinberg & Hasalova (2015) and references therein. As suggested in section 3.1.2, reaction 5 consists of two consecutive reactions, the first producing mostly clinopyroxene at around 700 °C (figure 22.B), the second producing mostly orthopyroxene at around 800 °C (figure 22.C), as observed from abundance plots. Similar to sample 787, retrograde conditions may be represented by garnet rim and orthopyroxene conditions, which is at about 735 °C and 6 kbar. Garnet breakdown during retrograde metamorphism suggests strong decompression, also seen in garnet abundance plots (figure 22.A). As modelled garnet endmember compositions from core to rim do not all match the transition from peak to retrograde conditions, the exact

retrograde path is unclear, although modelled spessartine and pyrope contents are in accordance with breakdown during decompression.

Rutile starts growing in relatively high pressure conditions, its border running from 600 °C and 7 kbar to 1000 °C and 10.8 kbar. As no new rutile growth is observed, the prograde path presumably stays below this border. The pargasite present in this sample is a clinoamphibole, which is only present below ~700 °C in the pseudosection. On the other hand, orthoamphibole, though not present in the sample, is present in the pseudosection until melting starts.

3.3.3 Sample 280

A pseudosection for this sample is given in figure 23. The X_{Mg} of garnet and biotite and the X_{An} of feldspar are plotted over the graph to visualize this sample's conditions. Light and dark red shows peak and rim composition of garnet respectively. Amphibole and orthopyroxene compositions from microprobe analysis do not occur on this pseudosection. The peak assemblage of Opx-Bt-Cam-Melt-Fsp-Ilm-Grt occurs at 810 °C and approximately 8 kbar (marked with pink). This field fits the feldspar composition; biotite X_{Mg} is also bordering this field. However, the garnet composition plots at a far lower temperature of approximately 580 °C. This may be due to retrograde resetting with bordering minerals during cooling. There is only little orthopyroxene formed in this sample, which coincides with the marked field, as this is just past the line where orthopyroxene comes into the system in the pseudosection. The retrograde path of this sample is unclear, as there is no mineral composition or mineral assemblage available on the pseudosection that fits the sample. However, garnet breakdown concurs with garnet abundance in this pseudosection (figure 24)

The compositions of amphibole, garnet and orthopyroxene do not fit with this pseudosection. This causes difficulty with interpretation and may be the result of either problems with the thermodynamic data (see section 4.3) or due to a problem with the input.

3.4 Geothermobarometry

The garnet-clinopyroxene thermometer is applied to garnet-clinopyroxene pairs in samples 787 and 968. This method uses experimental calibration of Mg-Fe fractionation between garnet and clinopyroxene. The estimated temperatures are 790 ± 40 °C for sample 787 and 810 ± 40 °C for sample 968, based on the method of Ellis & Green (1979) which is widely accepted as a thermometer for mafic granulites (Faulhaber & Raith 1991; Santosh et al. 2014; Takamura et al. 2015). These temperatures are possibly lower than peak conditions due to high-temperature homogenisation of garnet, which is observed widely in high-temperature zones (Tracy, 1982; Barnes & Carlson 2001). Using rim compositions of garnet, the estimated temperatures are: 701 ± 40 °C for sample 787 and 663 ± 40 °C for sample 968, which are likely to reflect initial retrograde conditions.

Temperatures obtained by the Grt-Opx thermometer by Sen & Bhattacharya (1984) are much higher: 993 ± 40 °C, 923 ± 40 °C and 746 ± 40 °C for the core and 801 ± 40 °C, 695 ± 40 °C and 714 ± 40 °C for the rim of samples 787, 968 and 280 respectively. These temperatures are similar to temperatures obtained by the biotite-garnet thermometer of Ferry & Spear (1978): 978 ± 30 °C and 735 ± 30 °C for the garnet core and all biotites except the needles and 831 ± 30 °C and 711 ± 30 °C for the garnet rim and biotite needles of samples 787 and 280 respectively.

The zirconium in rutile thermometer of Zack et al. (2004) gives a temperature of 725 ± 20 °C for sample 787. The Ti in biotite thermometer of Henry et al. (2005) gives a temperature of ~800 °C for all

biotites in sample 787, except the small needles, which give a temperature of 725 ± 30 °C. For sample 280, it gives a temperature of 785 ± 30 °C, and a temperature of 749 ± 30 °C for the small needles.

Barometry is done by the method of Moecher et al. (1988), which uses the assemblage of garnet + clinopyroxene/orthopyroxene + plagioclase + quartz to estimate the pressure. This method gives a pressure range of 9.2 ± 0.5 to 11 ± 0.5 kbars (Hedenbergite (HD) barometer) and 8 ± 0.5 to 9.5 ± 0.5 kbars (Diopside (DI) barometer) for samples 787 and 968 respectively. The Ferrosillite (FS) barometer, which uses orthopyroxene instead of clinopyroxene, gives pressures of 11 ± 0.5, 11 ± 0.5 and 10 ± 0.5 kbar for samples 787, 968 and 280 respectively.

3.5 Zircon geochronology

The results of zircon dating by LA-ICP-MS are given in appendix 1 & 2 for samples 968 and 280 respectively. Due to lack of rock sample available, sample 787 could not be analysed. Baddeleyite grains were not found in any samples. Cathodoluminescence (CL) images were taken of all zircons, and representative images are given in figure 25 for sample 968 and figure 26 for sample 280. Of sample 968, 90 spots were analyzed on 50 zircons; of sample 280, 106 spots were analyzed on 54 zircons. Figure 27 and 29 are Tera-Wasserburg Concordia diagrams (Tera & Wasserburg 1972) of samples 968 and 280 respectively. Histograms of zircons from samples 968 and 280 are given in figures 30 and 31 respectively.

3.5.1 Sample 968

Although multiple types of zircons occur in sample 968 and zoning is common, most zircons have a relatively similar age. Moreover, multiple analyses in single zircon grains show no clear correlation to the degree of cathodolumiscence. Both the MSWD and the average discordance (5.75%) are low in this sample. The upper intercept age of 558 ± 15 Ma fits well with the mean $^{238}U/^{206}Pb$ age of 555 ± 7 Ma. Th/U ratios of this sample generally lie around the mean value, which is 0.27. This value lies at the boundary between typical values for either metamorphic or igneous origin. A small group lies further below the average and ranges from 0.01 to 0.07, well within metamorphic values (Rubatto, 2002). This group comprises all analyses of dark cores (figure 25.B and C), which have a slightly older mean $^{238}U/^{206}Pb$ age than the rest of the zircons of this sample (585 ± 10 Ma). A Tera-Wasserburg Concordia diagram of this group is given in figure 28. This diagram shows a poorly defined upper intercept age of 1058 ± 670 Ma, which may represent an earlier metamorphic event. Moreover, another small group has a slightly higher Th/U ratio, ranging from 0.51 to 1.49. This group comprises analyses of either very bright uniform grains (figure 25.E) or very bright rims (figure 25.C). The age of this group is slightly younger than the rest of the sample, and has a mean $^{238}U/^{206}Pb$ age of 536 ± 6 Ma. The histogram of this sample (figure 27), shows a single, though broad, peak, which signifies a single growth stage or stages overlapping in time.

Zircons of this sample are generally rounded (figures 25.A and B) or subrounded (figures 25.D and G), although irregular and fragmented grains also occur (figures 25.C, E and F) and in the majority of zircons no zircon crystal shape can be distinguished. Within some zircons a vague shape reminiscent of a euhedral zircon crystal is visible (see the transition of light to dark blue in the rim and the outside of figure 25.D). Irregular sector zoning is quite common, see core of figure 25.A, B and C and figures 25.F and G, which is very common in granulite facies metamorphic zircons (Corfu et al. 2003). Uniformly bright zircons, like figure 25.E, are likely to have uniform, very low trace element contents (Corfu et al. 2003).

3.5.2 Sample 280

As with sample 968, multiple types of zircons occur in sample 280 and zoning is common, while zircons and multiple measurements in single zircons have a relatively similar age. Both the MSWD and the average discordance (7.79%) are low in this sample. The lower intercept age of 573 ± 9 Ma is equal to the mean $^{238}U/^{206}Pb$ age of 573 ± 6 Ma. Th/U ratios of this sample are generally around the mean value, which is 0.18. A small group lies further below the average and ranges from 0.01 to 0.08. Most of this group resembles figure 26C. However, this group does not differ in age with respect to the rest of the analyses. The poorly defined upper intercept age of 2471 ± 990 Ma may represent an igneous protolith age of some zircons, although this age has a large uncertainty as it is based on essentially two analyses. It does fit with the 2.3 Ga upper intercept reported by Hölzl et al. (1991, 1994) on metabasites. Similar to sample 968, the histogram of this sample (figure 31) shows a single broad peak, indicating a single growth stage.

Zircons of this sample are generally subrounded, with a vague zircon crystal shape sometimes present. (Irregular) sector zoning occurs both in dark cores (figure 26.A) and across entire zircons (figure 26.E). Concentric zoning (figure 26.F) also occurs, but is uncommon. Firtree zoning occurs in some zircons in this sample (figure 26.G), which reflects strong fluctuations of growth rates (Vavra et al. 1996). Oscillatory zoning (figure 26.H) is rare.

3.6 Trace elements

The results of LA-ICP-MS trace element analyses are given in table 4 for sample 787 and table 5 for sample 968. Chondrite normalized REE plots per mineral are given in figures 29 and 30 for sample 787 and 968 respectively. Due to the relatively small spot size, small minerals (e.g. biotite needles and zircon grains) could not be analyzed. Moreover, some analyses may be contaminated by other minerals, as the laser beam may be going through the desired grain. This occurs especially in micas, as they are generally thin minerals (in this case: biotite).

3.6.1 Sample 787

Garnets have typical HREE enriched chondrite normalized REE patterns. A small negative Eu anomaly is present, and the rims have a slightly higher negative Eu anomaly than the cores. The rim of garnet 1 is less enriched in HREE than the core: see the transition from dark to light blue in figure 32.A. The rim of garnet 2 is enriched in REE with respect to the core, except for its larger negative Eu anomaly. This could be due to an underlying mineral (probably plagioclase ± orthopyroxene symplectite) contaminating the analysis.

Apatite has a significant negative Eu anomaly and is enriched in LREE and depleted in HREE. Magnetite has very low REE abundance, and the only REE detected are La to Nd and Tb. Ilmenite + magnetite exsolution bands are low in REE as well, have a negative Eu anomaly and are slightly enriched in HREE.

The plagioclase located in the mesosome is enriched in HREE and slightly depleted in LREE in comparison to the leucosome. Plagioclase in symplectites are slightly enriched in LREE with respect to plagioclase in the rest of the sample, and highly enriched in HREE. Plagioclase in symplectites have a slightly smaller Eu peak than plagioclase occurring in the leucosome and the mesosome. Ternary feldspars and mesoperthites have a similar REE pattern and trace element content as the plagioclase the mesosome and leucosome respectively, except for higher amount of Rb and Ba. Symplectites (Pl + Opx) are similar to plagioclase except for a relative enrichment in HREE. The reason for this is the low REE abundance in orthopyroxene, making the symplectite contribution only visible at the heavier REE's, in which plagioclase is relatively depleted.

Biotite has very diverse REE patterns. As multiple analyses are very similar to other mineral's analyses (e.g. to feldspar in the red analysis in figure 32.D), it is likely an underlying mineral contaminated these analyses. The light blue analysis in figure 32.D appears free of contamination, and has a flat, slightly enriched profile. Biotite is high in Ti, V, Nb, Ba, Rb and Ta. As some types of biotite (described in section 3.2) are relatively small they could not be analyzed, therefore no comparison could be made between these types. However, one analysis has been made from symplectic biotite (seen in dark blue in figure 32.D), which has a very low REE abundance.

Clinopyroxene is enriched in REE, has a negative Eu anomaly and a slight negative anomaly with the heavier REE. Different crystals have a very similar pattern but highly variable degree of enrichment. Orthopyroxene has low REE contents with a slight positive Eu anomaly and minor enrichment in HREE.

Quartz in the leucosome is high in the incompatible elements Ba and Ta, but is otherwise depleted in trace elements.

3.6.2 Sample 968

Garnet rims are more enriched in HREE than cores, and the rim of garnet 2 (see figure 33.A) is also more enriched in the elements La to Nd. In the other garnet, the core is more enriched in LREE than the rim. Garnet 2 has relatively high negative Eu anomalies, while in the core of garnet 1 an Eu anomaly is barely noticeable.

Rutile is highly enriched in especially Nb, and also Hf, Ta and U. It is depleted in all other trace elements. Magnetite is rich in Ti in the mesosome only, and relatively depleted in most trace elements. Magnetite in the symplectite is enriched in LREE and depleted in HREE with respect to magnetite in the mesosome. Magnetite has a positive Eu anomaly. Note the depletion in Ce, part of the incompatible HFSE, in the symplectitic magnetite relative to the mesosome magnetite.

Symplectites have large positive Eu anomalies, except for the one depicted in orange in figure 33.C. These are relatively enriched in HREE with respect to the other symplectites. The analyses further away from the garnet porphyroblast in the symplectites depicted in orange are less enriched in all REE's than analyses close the garnet. In the symplectites depicted in blue, the analyses further away from the garnet are less enriched in HREE, and more enriched in LREE and Eu. This matches the decreasing Ca observed when going from Grt breakdown sites to the mesosome.

Plagioclase in the leucosome is slightly more enriched in HREE, depleted in LREE and has a lower negative Eu anomaly with respect to the mesosome. Symplectites are enriched in REE with respect to the plagioclase in the rest of the sample, and are especially enriched in HREE close to the garnet. The rim of leucosome grains are very similar to the core, but slightly enriched in HREE and depleted in less LREE. In the mesosome, one grain analyzed has a REE enriched core, while another has a REE enriched rim.

Amphiboles have rather flat REE patterns but highly variable degrees of enrichment. A negative Eu anomaly is present in 3 out of 4 analyses.

Clinopyroxenes are enriched in REE and have a negative Eu anomaly. They are relatively depleted in HREE. Orthopyroxenes in the mesosome have a slightly positive Eu anomaly, are slightly enriched in HREE and depleted in Ce. Orthopyroxenes in the symplectites are depleted in LREE, have negative Eu anomalies and are enriched in are enriched in HREE. Two analyses of coronas are similar to orthopyroxene in the symplectites, while one is similar to orthopyroxene in the mesosome. Orthopyroxene from symplectites and coronas also have negative Ce anomaly.

Quartz is high in La and very low in other trace elements.

4 Discussion

4.1 Assemblages and reactions: evidence for partial melting from textures, reactions and mineral chemistry.

4.1.1 Prograde

The prograde assemblage of the samples studied is quartz + plagioclase ± amphibole ± biotite, dependent on the composition of the rock. This is visible from both quartz and plagioclase inclusions in pyroxene and garnet, and from well aligned biotite/amphibole grains separated by pyroxene (figures 9 and 14). Both features represent prograde relicts. Increasing X_{Mg} of biotite also supports prograde biotite breakdown, as decomposition of biotite enriches the remaining biotite in the magnesium rich component which has a higher melting temperature.

4.1.2 Peak

The transition between prograde and peak metamorphism is represented by reactions 1, 2, 5 and 6. These reactions created the peritectic minerals garnet, clinopyroxene, orthopyroxene and K-feldspar. Another product of these reactions is a fluid or melt phase by a dehydration reaction, in this case the breakdown of amphibole and/or biotite. The presence of a quartz + plagioclase leucosomes suggests that a tonalitic melt was produced. As visible in figures 9 and 14, zonation in plagioclase occurs especially near grain boundaries and triple points, leaving the center of, especially the larger, grains unscathed. This suggests melting to have occurred at these sites, as melting generally starts at junctions between reactant phases, and forms thin films along grain boundaries and edges and cuspate pockets at the corners of melting minerals (e.g. Mehnert et al. 1973). These films then form tubes segregating into sites that later become patches of leucosome. Supporting this is the zonation pattern of plagioclase grains. During the partial dissolution of plagioclase, the albite component fractionates into the melt (Bowen 1913). This leaves the restitic plagioclase with an increased anorthite content, which fits with the studied samples.

It would thus be logical for the plagioclase in the leucosome to be more albitic than the plagioclase in the mesosome. However, in the samples studied the anorthite content between the mesosome and the leucosome is very similar. This finding is actually quite common (Sawyer 2008). Various theories could explain this. For example, the leucosome seen in the samples could be only part of the melt migration pathway, meaning the albitic proportion of the plagioclase could have been transported elsewhere, thus making the leucosome observed in the sample not representative of the melt. Consequently, leucosomes may not reflect actual melt composition, while they do give evidence for the presence of a melt during peak metamorphism (Nehring 2010). Another reason could be the rate of dissolution of plagioclase, as Johannes (1978, 1980, 1984) and Acosta-Vigil et al. (2006) have shown that the kinetics of dissolution of intermediate plagioclase is very slow at temperatures up to 800 °C. This would lead to a similar composition of the leucosome and mesosome plagioclase.

In contrast to sample 787, plagioclase grains in the leucosome of sample 968 show a decreasing anorthite content from core to rim, which is this is typical for melt crystallization from high to low temperature where low-T albite crystallizes after high-T anorthite. The varying zonation patterns of

plagioclase in the leucosome may be a local effect. As described in section 4.1.3, garnet decomposition may cause local sodium diffusion from plagioclase in the leucosome to symplectitic domains, causing a decreasing Na from core to rim. These effects may thus cause slight variation in zonation patterns of plagioclase in the leucosome. Moreover, the composition of liquidus plagioclase has been subject of debate in more studies, as it depends on many parameters, e.g. the content of Ca, Al, H_2O in the melt and the crystallization pressure (Panjasawatwong 1995), and may also be affected by reorientation of vein arrays or stress fields (Simakin and Talbot 2001 a,b).

Typically, recrystallization tends to increase grain size and produce euhedral crystals (Sawyer 2008). When looking at the leucosome of samples 787 and 968, the leucosome consists of quartz with a very large grain size and plagioclase with a varying but smaller grain size. Recrystallization and static mineral growth also involve solid state diffusion, which is much slower in plagioclase than in quartz. In sample 280, leucosome exhibits a foam texture of relatively small plagioclase and quartz grains, which is a classical equilibrium texture that is common at high temperatures.

It is common for partially molten rocks to show former films of melt in the mesosome. However, in slowly cooled rocks the evidence for these films is generally removed. As particularly samples 787 and 968 experienced limited back reaction, i.e. the products of the dehydration reaction have been preserved through retrograde metamorphism, the majority of the melt formed has probably migrated away from the system (Storkey 2005). In sample 280 the water content is much higher due to the high amount of amphibole present, which resulted in a larger amount of back reaction. This is particularly visible from the pervasively corroded nature of the garnets.

4.1.3 Retrograde

Garnets have a relatively flat compositional profiles in their cores, which is most likely due to high-temperature homogenization, which is observed widely in high-temperature rocks (Tracy 1982; Barnes & Carlson 2001). The increase of almandine content and decrease in pyrope content near the rim are likely due to volume diffusion resetting during cooling by Fe-Mg exchange with clinopyroxene ± amphibole ± biotite (Tracy 1982). This process represents the transition from peak to the initial retrograde stage and suggests that the calculated temperatures from Fe-Mg exchange thermometry (section 3.4) may underestimate peak temperatures. The increase in spessartine component (Mn) at the garnet rim is typical for garnet breakdown, as Mn is not easily incorporated into other minerals during retrogression, creating an Mn enrichment in the garnet rim (e.g. Tucillo et al. 1990). Moreover, REE diffusion rates are much slower than of e.g. Mn, so REE are transferred to symplectitic plagioclase rather than being concentrated in the Grt rim. Reaction 3 represents the transition from initial retrograde to the retrograde stage, in which garnet is broken down into symplectites or pseudomorphs after garnet. This reaction first causes formation of the orthopyroxene and plagioclase coronas, denoting high diffusion rates. Plagioclase grows on the aluminum rich side (garnet), whereas orthopyroxene grows on the silica rich side (leucosome). When temperatures start to drop, diffusion rates decrease as well, causing garnet breakdown to symplectites instead of coronas. Plagioclase composition also indicates declining diffusion rates (and thus temperatures). As garnet and clinopyroxene lack the sodium present in the plagioclase coronas, the only (and most proximate) source of sodium is the leucosome. Thus the system strives to homogenize the local plagioclase compositions by breaking down the rim of leucosome plagioclase, releasing sodium, and growing new plagioclase in two places at the same time: plagioclase in the symplectitic domain and a plagioclase rim on the older leucosome plagioclase (also causing the zoning pattern in the leucosome as discussed in 4.1.2). The reason is the notoriously slow major element diffusion in plagioclase that has been reported by experimental petrologists

(e.g. Johannes and Holtz, 1996). When temperatures and diffusion rates started to drop, the plagioclase incorporated a decreasing amount of sodium, from X_{Ab} of ~0.50 in the corona to ~0.13 close to the garnet (figure 12).

When the temperature of a metamorphic terrain starts to drop, the remaining melt crystallizes, driving out the fluids contained in the melt. This leads to rehydration reactions: garnet reacts with the crystallizing melt to produce biotite (reversed of reactions 1, 2 and 6). In samples 787 and 280 the rehydration reaction caused the formation of biotite needles in symplectic domains. As the titanium content is generally low in the melt, these biotite needles have a lower Ti content. Additionally, magnetite and ilmenite formed from biotite breakdown lowered the amount of Ti available for new biotite growth. Additional evidence for crystallization from melt comes from the euhedral shape of the biotite needles (Kriegsman and Álvarez-Valero, 2010).

4.2 Trace element patterns

Garnets have fairly typical REE patterns, with slightly negative Eu anomalies. The moderate Eu anomalies may be due to Eu partitioning into a plagioclase-rich melt. The difference in zoning patterns between porphyroblasts may be due to local variation, resulting in complex zoning (Storkey 2005). This is predominantly the consequence of a lack of equilibrium between garnet and the mesosome due to slow diffusion rates of REE (Nehring 2010). This results in the garnet composition to be dependent on its immediate surroundings.

The REE pattern of ilmenite-magnetite solid solution in sample 787 fits reaction 4 very well, as it has a negative Eu anomaly, due to the coexistence with plagioclase during symplectite formation, and is slightly enriched in HREE, due to garnet breakdown. Magnetite in 968 has lower amount of Ti in symplectites with respect to mesosome, because Grt breakdown does not release any Ti, whereas mesosome magnetite formed by breakdown of Ti-rich Bt is enriched in Ti.

The only systematic difference in trace element patterns between plagioclase in the leucosome and mesosome is a slight enrichment in HREE in the mesosome (sample 787). The reason for this probably is that garnet formed together with the melt that later formed the leucosome, causing the melt to be slightly depleted in HREE. Moreover, this is reversed in sample 968, similar to the reversed Ca/Na zoning in this sample compared to 787, which is probably related to each other and has similar causes (see section 4.1.2). Furthermore, symplectitic plagioclase clearly has a higher HREE content, which it inherited from garnet during retrograde garnet breakdown. As REE are slowly diffusing elements, they probably had no time to diffuse back into relict garnet. Additionally, the Rb and Ba content of mesoperthites relative to ternary feldspar from the mesosome is increased, as these incompatible elements partition into the melt. Especially Ba is highly compatible with K-feldspar and thus provides a good measure of its involvement in melting reactions (Zeng et al. 2005). The analyses further away from the garnet porphyroblast in the symplectites are less enriched in all REEs than analyses close the garnet, which is due to REE being gradually released from garnet during breakdown.

Comparing the light blue and dark blue REE patterns of biotite (figure 32.D), which probably are the only biotite analyses unaffected by other minerals' contamination, the symplectitic biotite has a much lower trace element abundance. A reason for this may be that incompatible elements partition into the melt, lowering the trace element content of the symplectitic biotite which formed during retrograde back reaction.

Clinopyroxene shows a clear depletion in HREE relative to the rest of its pattern, probably due to its coexistence with garnet. The negative Eu anomaly is due to simultaneous plagioclase growth. Orthopyroxene has a higher relative abundance of HREE, which suggests it (mostly) did not form during garnet formation, but rather before or after. From orthopyroxene abundance plots in the pseudosection we known the majority of orthopyroxene grew at around 800 °C, making it probable it grew after most of the garnet porphyroblasts did. Orthopyroxene in the symplectites are relatively depleted in LREE compared to mesosome orthopyroxene, and also have negative Eu anomalies and are enriched in HREE. This is due to their formation as a result of the breakdown of garnet, together with plagioclase.

Amphibole has a relatively flat REE pattern, although a slight negative Eu anomaly is common which is a result of its coexistence with plagioclase.

In sample 787, quartz is clearly enriched in Ba and La, which are elements that partition into the melt. In sample 968, quartz in enriched in La, which like the LILE and HFSE is an incompatible element known to partition into the melt. Moreover, both orthopyroxene and magnetite have a significantly lower Ce concentration in the symplectite relative to the mesosome (sample 968). Ce is also part HFSE, known to partition into the melt.

4.3 Geothermobarometry comparison

Table 6 shows a comparison between geothermobarometry results and Perple_X pseudosections. Estimates of peak metamorphic temperatures vary significantly, especially for sample 787. However, Perple_X modelling results fall right in between these values, except for sample 280 which shows a slightly higher temperature in the model than in geothermometers. Reasons for the variation in thermometry results may be higher temperatures of formation of the mineral pairs or a difference in diffusion rates between these minerals. Also, a small variation in mineral composition may cause a significant change in temperature. Moreover, the thermometer of Sen & Bhattacharya (1984) is considered to typically give higher than average values (e.g. Sajeev & Osanai 2004). Considering volume diffusion resetting during cooling and probable overestimation of the Grt-Opx thermometer, I suggest that Perple_X results best indicate peak pressure and temperature conditions.

Biotite needles in samples 787 and 280 are a clear indicator of retrograde conditions, and probably mark the timing of melt crystallization (see section 4.1.3). Therefore, I suggest the use of Grt_{rim} and Bt_{needle} with the thermometer of Ferry & Spear (1978) to be the best indicator of the timing of melt crystallization. For sample 787, this temperature fits with Perple_X modelling.

Several significant differences were found between textural observations and pseudosections made by Perple_X. Orthopyroxene was found in high abundances and already at low temperatures in pseudosections for both sample 787 and 968. Moreover, garnet is present throughout the entire pseudosections and also has a high abundance, especially in prograde conditions. Biotite compositions in pseudosections of both 787 and 280 do not fit microprobe data; garnet compositions in the pseudosection of 280 do not fit with geothermobarometry and textural observations. Finally, the occurrence of melt starts at temperatures higher than expected from literature data in sample 787 and lower than expected from literature data in samples 968 and 280 (e.g. Weinberg and Hasalová 2015). The above described discrepancies may be due to the lack of a well-developed thermodynamic database for partial melting of basic and intermediate rocks (R.W. White, personal communication 2014). Recently efforts have been made to improve this database by Green et al. (2016) and Palin et al. (2016). The rock compositions used in these studies are similar to the input used in this study. However, the results of these studies have not yet been

implemented in Perple_X. When these thermodynamic databases are updated, the results of modelling by Perple_X will probably be improved.

4.4 Zircon analysis

The timing of metamorphism in the HC has been shown to be in the range of 610-530 Ma (e.g. Baur et al. 1991; Hölzl et al. 1994; Kröner, Jaeckel, et al. 1994; Sajeev et al. 2007). My lower intercept ages of 558 ± 15 Ma and 573 ± 9 Ma fit well with other studies, e.g. Sajeev et al. (2010) which suggest (near) peak conditions at about 570 Ma. Moreover, both upper intercept ages (1058 ± 670 Ma in sample 968 and 2471 ± 990 Ma in sample 280) suggest a trace of an old component, which fits with other studies (e.g. Hölzl 1991 and Hölzl 1994). However, due to the large uncertainty, these ages cannot be fitted to a part of the history of the zircons. Both upper intercept ages may thus be a trace of the complex history of the rock.

Generally, zircons from both samples are (sub)rounded, have a Th/U of slightly higher than typical of metamorphic zircons, and show complex zoning patterns. From the abundant differentiated cores and traces of old upper intercept ages, I infer the majority of zircons to be reworked xenocrystic zircons. The trace element composition of these zircons has been largely altered in the last metamorphic event due to high temperatures, thereby causing little preservation of previous (metamorphic) events. The sector zoning commonly seen in the samples studied, together with their multi-faceted habit (figure 25.F and G; figure 26.E), have also been called ‘soccerball’ zircons; these types of zircons have previously been interpreted as zircons grown from partial melts (Kelly and Harley 2005; Harley 2007; Vavra 1996).

In both samples there is a group of zircons with a distinct core and low (<0.1) Th/U values, inferring a metamorphic origin. These cores could have been formed by either dissolution and reprecipitation of the former core (Bhowmik et al. 2014) or by new zircon growth. Other studies found new zircon growth during metamorphism to be limited to rocks that underwent anataxis, with increasing amounts of zircon with increasing metamorphic grade (Vavra et al. 1999; Rubatto et al. 2001). The round shapes of the cores may be due to dissolution in melt after formation (Bhowmik et al. 2014). The probable timing of this event is during dehydration reactions of biotite/amphibole, causing dissolution of (part of) existing zircons at the onset of partial melting. The first occurrence of zircon overgrowths happens when temperatures start to drop after peak metamorphism, which is when part of the melt starts to crystallize again. As solubility of zirconium increases with increasing temperature, zircons will start to form when temperatures decrease (Watson and Harrison 1983; Rubatto 2001). Therefore, the oldest zircon ages found likely correlate with near-peak conditions. In sample 968, the age of this group clearly differs from the rest of the zircons analysed, with an 238U/206Pb age of 585 ± 10 Ma, which I correlate with near peak conditions just after peak metamorphism. However, in sample 280 this group does not differ in age from the rest of the analyses. As the low Th/U group of zircons clearly differs from other zircons, I conclude this group to have formed just after peak metamorphism.

Another group of zircons from sample 968 with somewhat higher Th/U values than the rest of the zircons from the same sample, has a mean 238U/206Pb age of 536 ± 6 Ma and comprises bright rims and bright uniform grains. The timing of formation of these zircons may be during final crystallization of anatectic melt. When temperatures in a metamorphic terrain start to drop, any melt that is not yet extracted will crystallize. This will lead to the production of fluids, hydrating the current mineral assemblage. Hydration reactions involved can induce zircon growth, as retrogressing phases may release the zirconium they contain (Nyström & Kriegsman, 2003; Harley 2007). Moreover, grains or rims with bright CL patterns are known to be low in trace elements (Corfu et al. 2003). As incompatible trace elements partition into the melt, this is also evidence for formation after most of the melt was extracted. Consequently, I suggest this group to either

have overgrown an older core (bright rims), or to have grown completely (bright uniform grains) during final crystallization of melt.

Takamura et al. (2015) and Santosh et al. (2014) both suggest 2 separate events, as their zircon geochronology data has two peaks of about 570 and 530 Ma. However, my analyses of Th/U values combined with textural observations rather suggest a single longer event, with 585 Ma as the timing just after peak conditions and 536 Ma as the timing of final retrograde overgrowth during crystallization from melt. Using figure 21, the difference in temperature from peak conditions up to the last occurrence of melt is about 100 °C, which results in a cooling rate of ~2 °C/Ma. This concurs with the cooling age of 2-3 °C/Ma between 560 and 480 Ma found by Hölzl et al. (1991) using Sm-Nd garnet ages.

5 Conclusions

Dehydration melting reactions created the peritectic minerals garnet, clinopyroxene, orthopyroxene and K-feldspar and caused the formation of a tonalitic melt. This is supported by petrographic textures as well as microprobe and trace element data. Evidence for formation of melt includes the formation of leucosomes, parallel to the gneissic layering, and melt remnants at triple points and grain boundaries of plagioclase grains. Plagioclase zoning is also consistent with the loss of albite, the plagioclase component with the lowest melting temperature, to the melt phase.

When temperatures started to drop, the remaining melt crystallized. This is supported by a decreasing anorthite content in leucosomal plagioclase, which is typical for melt crystallization where low-T Ab crystallizes after high-T An. However, this did not occur near garnet porphyroblasts, as garnet breakdown caused diffusion of albite from the leucosome to plagioclase coronas. Melt crystallization also induced rehydration reactions, particularly in symplectic domains, as testified by the formation of euhedral biotite grains with a relatively low Ti concentration, locally intergrown with plagioclase, at garnet rims.

Relative enrichment of Rb and Ba, typical incompatible elements, into leucosomal K-feldspar and Ba and La into leucosomal quartz provide further evidence for melting.

The majority of zircons are xenocrystic zircons which are reworked during partial melting. The onset of partial melting induced dissolution of zircons, visible from the “soccerball” habit and low Th/U values. When temperatures started to drop, the crystallization of melt and decreased Zr solubility caused the formation of new zircons and the overgrowth of older cores.

Analyses of Th/U values combined with textural observations in zircons infer a single long metamorphic event, with 585 ± 10 Ma as the age just after peak metamorphism and 536 ± 6 Ma as the timing of final retrograde overgrowth during crystallization from melt.

Geothermobarometry gives a peak temperature of 810 – 925 °C and pressures of 8.0 – 9.8 kbar, depending on the sample. Retrograde conditions using biotite needles crystallized from melt are in the order of 735 – 840 °C and 6.0 – 8.3 kbar.

References

Acosta-Vigil, A., London, D. Morgan, G.B., 2006. Experiments on the kinetics of partial melting of a leucogranite at 200 MPa H2O and 690–800 °C: compositional variability of melts during the onset of H2O-saturated crustal anatexis. Contributions to Mineralogy and Petrology 151(5), 539-557.

Barnes, J. D., Carlson, W. D., 2001. Major-and trace-element zoning as a function of garnet crystallization temperature. Geological Society of America Abstracts with Programs 33(5), 56.

Baur, N., Kröner, N.A., Liew, T.C., Todt, W., Williams, I.S., Hofmann, A.W., 1991. U-Pb Isotopic Systematics of Zircons from Prograde and Retrograde Transition Zones in High-Grade Orthogneisses. The Journal of Geology 99(4), 527–545.

Bea, F., Montero, P., 1999. Behavior of accessory phases and redistribution of Zr, REE, Y, Th, and U during metamorphism and partial melting of metapelites in the lower crust: An example from the Kinzigite Formation of Ivrea-Verbano, NW Italy. Geochimica et Cosmochimica Acta 63(7–8), 1133–1153.

Beard, J.S., Lofgren, G.E., 1991. Dehydration melting and water-saturated melting of basaltic and andesitic greenstones and amphibolites at 1, 3, and 6. 9 kb. Journal of Petrology 32(2), 365–401.

Bhowmik, S.K., Wilde, S.A., Bhandari, A., Sarbadhikari, A.B., 2014. Zoned monazite and zircon as monitors for the thermal history of granuliteterranes: An example from the Central Indian Tectonic Zone. Journal of Petrology 55(3), 585–621.

Bowen, N.L., 1913. The melting phenomena of the plagioclase feldspars. American Journal of Science 210, 577-599.

Braun, I., Kriegsman, L.M., 2003. Proterozoic crustal evolution of southernmost India and Sri Lanka. Geological Society, London, Special Publications 206(1), 169–202.

Breton, N.L. Thompson, A.B., 1988. Fluid-absent (dehydration) melting of biotite in metapelites in the early stages of crustal anatexis. Contributions to Mineralogy and Petrology 99(2), 226–237.

Büsch, W., Schneider, G., Mehnert, K.R., 1974. Initial melting at grain boundaries. Part II: Melting in rocks of granodioritic, quartzdioritic and tonalitic composition. Neues Jahrbuch für Mineralogie, Monatshefte 8, 345-370.

Carrington, D.P., Watt, G.R., 1995. A geochemical and experimental study of the role of K-feldspar during water-undersaturated melting of metapelites. Chemical Geology 122, 59–76.

Cenki, B., Kriegsman, L.M., Braun, I., 2002. Melt-producing and melt-consuming reactions in the Achankovil cordierite gneisses, South India. Journal of Metamorphic Geology, 20(6), 543-561.

Cooray, P.G., 1994. The precambrian of Sri Lanka: a historical review. Precambrian Research 66(1–4), 3–18.

Cordani, U., Cooray, P.G., 1989. Rb-Sr ages of granites and gneisses from the Precambrian of Sri Lanka. Journal of the Geological Society of Sri Lanka 2, 35-43.

Corfu, F., Hanchar, J.M., Hoskin, P.W.O., Kinny, P., 2003. Atlas of Zircon Textures. Reviews in Mineralogy & Geochemistry 53(1).

Dharmapriya, P.L., Malaviarachchi, S.P.K., Galli, A., Su, B., Subasinghe, N.D., Dissanayake, C.B., 2015. Rare evidence for formation of garnet+corundum during isobaric cooling of ultrahigh temperature metapelites: New insights for retrograde P-T trajectory of the Highland Complex, Sri Lanka. Lithos 220–223, 300–317.

Ellis, D.J., Green, D.H., 1979. Contributions to Mineralogy and An Experimental Study of the Effect of Ca Upon Garnet-Clinopyroxene Fe--Mg Exchange Equilibria. Contributions to Mineralogy and Petrology 22, 13–22.

Faulhaber, R., Schumacher, S., 1994. Summary and discussion of P-T estimates from garnet- pyroxene-plagioclase-quartz-bearing granulite-facies rocks from Sri Lanka. Precambrian Research, Elsevier Science B.V. 66, 295–308.

Faulhaber, S., Raith, M., 1991. Geothermometry and Geobarometry of High-Grade Rocks: A Case Study on Garnet-Pyroxene Granulites in Southern Sri Lanka. Mineralogical Magazine 55(378), 33–56.

Ferry, J.M., Spear, F.S., 1978. Experimental Calibration of the Partitioning of Fe and Mg Between Biotite and Garnet. Contributions to Mineralogy and Petrology 66, 113–117.

Foley, S.F., Tiepolo, M., Vannucci, R., 2002. Growth of early continental crust controlled by melting of amphibolite in subduction zones. Nature 417(6891), 837–840.

Green, E.C.R., White, R.W., Diener, J.F.A., Powell, R., Holland, T.J.B., Palin, R.M., 2016. Activity–composition relations for the calculation of partial melting equilibria in metabasic rocks. Journal of Metamorphic Geology, 34(9), 845-869.

Harley, S.L., 1989. The origin of granulites: a metamorphic perspective. Geological Magazine 126, 215-247

Harley, S. L., Kelly, N. Möller, A., (2007). Zircon behaviour and the thermal histories of mountain chains. Elements 3, 25-30.

Hermann, J., Rubatto, D., 2003. Relating zircon and monazite domains to garnet growth zones: age and duration of granulite facies metamorphism in the Val Malenco lower crust. Journal of Metamorphic Geology, 21(9), 833-852.

Hiroi, Y., Ogo, Y., Namba, K., 1994. Evidence for prograde metamorphic evolution of Sri Lankan pelitic granulites, and implications for the development of continental crust. Precambrian Research 66(1–4), 245–263.

Hölzl, S., Köhler, H., Kröner, A., Jaeckel, P., Liew, T. C. 1991. Geochronology of the Sri Lankan basement. In The Crystalline Crust of Sri Lanka, Part I. Summary of Research of the German-Sri Lankan Consortium 5, 237-257.

Hölzl, S., Hofmann, A.W., Todt, W., Köhler, H., 1994. U-Pb geochronology of the Sri Lankan basement. Precambrian Research 66(1–4), 123–149.

Jahn, B. M., Auvray, B., Shen, Q. H., Liu, D. Y., Zhang, Z. Q., Dong, Y. J., ... & Mace, J.,1988. Archean crustal evolution in China: the Taishan complex, and evidence for juvenile crustal addition from long-term depleted mantle. Precambrian Research 38(4), 381-403.

Johannes, W., 1978. Melting of plagioclase in the system Ab − An − H2O and Qz − Ab − An − H2O at P_{H2O} =5 kbars, an equilibrium problem. Contributions to Mineralogy and Petrology 66(3), 295-303.

Johannes, W., 1980. Metastable melting in the granite system Qz-Or-Ab-An-H2O. Contributions to Mineralogy and Petrology 72(1), 73-80.

Johannes, W., 1984. Beginning of melting in the granite system Qz-Or-Ab-An-H2O. Contributions to Mineralogy and Petrology 86(3), 264-273.

Johannes, W., Holtz, F., 2012. Petrogenesis and experimental petrology of granitic rocks (Vol. 22). Springer Science & Business Media.

Johnson, T. E., Fischer, S., White, R. W., Brown, M., Rollinson, H. R., 2012. Archaean intracrustal differentiation from partial melting of metagabbro-field and geochemical evidence from the central region of the Lewisian complex, NW Scotland. Journal of Petrology 53(10), 2115–2138.

Johnston, A.D., 1986. Anhydrous P-T phase relations of near-primary high-alumina basalt from the South Sandwich Islands - Implications for the origin of island arcs and tonalite-trondhjemite series rocks. Contributions to Mineralogy and Petrology 92(3), 368–382.

Kelly, N.M., Harley, S.L., 2005. An integrated microtextural and chemical approach to zircon geochronology: refining the Archaean history of the Napier Complex, east Antarctica. Contributions to Mineralogy and Petrology 149(1), 57-84.

Kretz, R.,1983. Symbols of rock-forming minerals. American Mineralogist 68, 277–279.

Kriegsman, L.M., 1993. Geodynamic evolution of the Pan-African lower crust in Sri Lanka: structural and petrological investigations into a high-grade gneiss terrain. Faculty of Earth Sciences, Utrecht.

Kriegsman, L.M., 1995. The Pan-African event in East Antarctica: a view from Sri Lanka and the Mozambique belt. Precambrian Research, 75(3-4), 263-277.

Kriegsman L.M. 1996. Divariant and trivariant reaction line slopes in FMAS and CFMAS: Theory and applications. Contributions to Mineralogy and Petrology 126, 38-50.

Kriegsman, L.M., Hensen, B. J., 1998. Back reaction between restite and melt: implications for geothermobarometry and pressure-temperature paths. Geology 26(12), 1111-1114.

Kriegsman, L.M., Schumacher, J.C., 1999. Petrology of Sapphirine-bearing and Associated Granulites from Central Sri Lanka. Journal of Petrology 40(8), 1211–1239.

Kriegsman, L.M., Álvarez-Valero, A.M., 2010. Melt-producing versus melt-consuming reactions in pelitic xenoliths and migmatites. Lithos, 116(3), 310-320.

Kröner, A., 1985. Evolution of the Archean continental crust. Annual Review of Earth and Planetary Sciences 13, 49–74.

Kröner, A., Williams, I.S., Compston, W., Baur, N., Vitanage, P.W., Perera, L.R.K., 1987. Zircon Ion Microprobe Dating of High-Grade Rocks in Sri Lanka. The Journal of Geology 95(6), 775–791.

Kröner, A., Jaeckel, P., Williams, I.S., 1994. Pb-loss patterns in zircons from a high-grade metamorphic terrain as revealed by different dating methods: UPb and PbPb ages for igneous and metamorphic zircons from northern Sri Lanka. Precambrian Research 66(1–4), 151–181.

Kröner, A., Kehelpannala, K.V.W., Kriegsman, L.M., 1994. Origin of compositional layering and mechanism of crustal thickening in the high-grade gneiss terrain of Sri Lanka. Precambrian Research 66(1–4), 21–37.

Kröner, A., Williams, I.S., 1993. Age of Metamorphism in the High-Grade Rocks of Sri Lanka. The Journal of Geology 101(4), 513–521.

Kunz, B.E. Johnson, T.E., White, R.W., Redler, C., 2014. Partial melting of metabasic rocks in Val Strona di Omegna, Ivrea Zone, northern Italy. Lithos 190–191, 1–12.

Malaviarachchi, S.P.K., Dharmapriya, P.L., 2015. Revisiting Ultrahigh Temperature Granulites of Sri Lanka: New Prograde and Retrograde Mineral Textures from the Highland Complex. Journal of the Indian Institute of Science 95(2), 159-172.

Malaviarachchi, S.P.K., Takasu, A., 2011. Electron microprobe dating of Monazites from Sri Lanka : implications on multiple thermal events related to Gondwana. Journal of the Geological Society of Sri Lanka 14, 81–90.

Mehnert, K.R., Büsch, W., Schneider, G., 1973. Initial melting at grain boundaries of quartz and feldspar in gneisses and granulites. Neues Jahrbuch für Mineralogie, Monatshefte 4, 165-183.

Mengel, F. and Rivers, T., 1991. Decompression Reactions and P—T Conditions in High-grade Rocks, Northern Labrador: P—T—t Paths from Individual Samples and Implications for Early Proterozoic Tectonic Evolution. Journal of Petrology 32(1), 139-167.

Milisenda, C.C. Liew, T.C., Hofmann, A.W., Kröner, A., 1988. Isotopic Mapping of Age Provinces in Precambrian High-Grade Terrains : Sri Lanka. The Journal of Geology 96(5), 608–615.

Milisenda, C.C. Liew, T.C., Hofmann, A.W., Kröner, A., 1994. Nd isotopic mapping of the Sri Lanka basement: update, and additional constraints from Sr isotopes. Precambrian Research 66(1–4), 95–110.

Moecher, D.P., Essene, E.J., Anovitz, L.M., 1988. Calculation and application of clinopyroxene-garnet-plagioclase-quartz geobarometers. Contributions to Mineralogy and Petrology 100(1), 92–106.

Nehring, F. Foley, S.F., Hölttä, P., Van Den Kerkhof, A.M., 2009. Internal differentiation of the archean continental crust: Fluid-controlled partial melting of granulites and TTG - Amphibolite associations in Central Finland. Journal of Petrology 50(1), 3–35.

Nehring, F., Foley, S.F., Hölttä, P., 2010. Trace element partitioning in the granulite facies. Contributions to Mineralogy and Petrology 159(4), 493-519.

Nyström, A.I., Kriegsman, L.M., 2003. Prograde and retrograde reactions, garnet zoning patterns, and accessory phase behaviour in SW Finland migmatites, with implications for geochronology. Geological Society, London, Special Publications, 220(1), 213-230.

Van Orman, J.A., Grove, T.L., Shimizu, N., Layne, G.D., 2002. Rare earth element diffusion in a natural pyrope single crystal at 2.8 GPa. Contributions to Mineralogy and Petrology 142(4), 416-424.

Osanai, Y. Sajeev, K., Owada, M., Kehelpannala, K.W., Prame, W.B., Nakano, N., Jayatileke, S., 2006. Metamorphic evolution of high-pressure and ultrahigh-temperature granulites from the Highland Complex, Sri Lanka. Journal of Asian Earth Sciences 28(1), 20–37.

Otamendi, J. E., Jesús, D., Douce, A. E. P., & Castro, A., 2002. Rayleigh fractionation of heavy rare earths and yttrium during metamorphic garnet growth. Geology, 30(2), 159-162.

Palin, R.M., White, R.W., Green, E.C., Diener, J.F., Powell, R., Holland, T.J., 2016. High-grade metamorphism and partial melting of basic and intermediate rocks. Journal of Metamorphic Geology, 34(9), 871-892.

Panjasawatwong, Y., Danyushevsky, L.V., Crawford, A.J., Harris, K.L., 1995. An experimental study of the effects of melt composition on plagioclase-melt equilibria at 5 and 10 kbar: implications for the origin of magmatic high-An plagioclase. Contributions to Mineralogy and Petrology 118(4), 420-432.

Raase, P., Schenk, V., 1994. Petrology of granulite-facies metapelites of the Highland Complex, Sri Lanka: implications for the metamorphic zonation and the P-T path. Precambrian Research 66(1–4), 265–294.

Rapp, R.P., Watson, E.B., Miller, C.F., 1991. Partial melting of amphibolite/eclogite and the origin of Archean trondhjemites and tonalites. Precambrian Research 51(1–4), 1–25.

Rapp, R.P., 1995. Amphibole-out phase boundary in partially melted metabasalt, its control over liquid fraction and composition, and source permeability. Journal of Geophysical Research 100(B8), 15601-15610.

Rapp, R.P., Shimizu, N., Norman, M.D., 2003. Growth of early continental crust by partial melting of eclogite. Nature 425(October), 605.

Roberts, M. P., Finger, F. (1997). Do U-Pb zircon ages from granulites reflect peak metamorphic conditions? Geology 25, 319-322.

Robin, P.Y.F., 1979. Theory of metamorphic segregation and related processes. Geochimica et Cosmochimica Acta 43, 1587–1600.

Rubatto, D., Williams, I.S., Buick, I.S., 2001. Zircon and monazite response to prograde metamorphism in the Reynolds Range, central Australia. Contributions to Mineralogy and Petrology 140(4), 458-468.

Rubatto, D., Hermann, J., Buick, I.S., 2006. Temperature and bulk composition control on the growth of monazite and zircon during low-pressure anatexis (Mount Stafford, central Australia). Journal of Petrology 47(10), 1973-1996.

Rubatto, D., Chakraborty, S. Dasgupta, S., 2013. Timescales of crustal melting in the Higher Himalayan Crystallines (Sikkim, Eastern Himalaya) inferred from trace element-constrained monazite and zircon chronology. Contributions to Mineralogy and Petrology, 165(2), 349-372.

Rushmer, T., 1991. Partial melting of two amphibolites: contrasting experimental results under fluid absent conditions. Contributions to Mineralogy and Petrology 107, 41–59.

Sajeev, K., Osanai, Y., 2004. Ultrahigh-temperature metamorphism (1150°C, 12 kbar) and multistage evolution of Mg-, Al-rich granulites from the central Highland Complex, Sri Lanka. Journal of Petrology 45(9), 1821–1844.

Sajeev, K., Osanai, Y., 2005. Thermal gradients in the Sri Lankan granulite terrane: A garnet-biotite thermometric approach. Journal of Metamorphic Geology 23(5), 383–397.

Sajeev, K. Osanai, Y., Connolly, J.A.D., Suzuki, S., Ishioka, J., Kagami, H., Rino, S., 2007. Extreme Crustal Metamorphism during a Neoproterozoic Event in Sri Lanka: A Study of Dry Mafic Granulites. The Journal of Geology 115(5), 563–582.

Sajeev, K., Williams, I.S., Osanai, Y., 2010. Sensitive high-resolution ion microprobe U-Pb dating of prograde and retrograde ultrahigh-temperature metamorphism as exemplified by Sri Lankan granulites. Geology 38(11), 971–974.

Sandiford, M., Powell, R., Martin, S.F. Perera, L.R.K., 1988. Thermal and baric evolution of garnet granulites from Sri Lanka. Journal of Metamorphic Geology, 6(3), 351-364.

Santosh, M. Tsunogae, T., Malaviarachchi, S.P., Zhang, Z., Ding, H., Tang, L., Dharmapriya, P. L., 2014. Neoproterozoic crustal evolution in Sri Lanka: Insights from petrologic, geochemical and zircon U-Pb and Lu-Hf isotopic data and implications for Gondwana assembly. Precambrian Research 255(P1), 1–29.

Sawyer, E.W., 1991. Disequilibrium melting and the rate of melt-residuum seperation during migmatization of mafic rocks from the Greenville Front Quebec. Journal of Petrology 32, 701–738.

Sawyer, E.W., 2008. Atlas of migmatites (Vol. 9). NRC Research Press.

Sen, C., Dunn, T., 1994. Dehydration melting of a basaltic composition amphibolite at 1.5 and 2.0 GPa: implications for the origin of adakites. Contributions to Mineralogy and Petrology 117(4), 394–409.

Sen, S.K., Bhattacharya, A., 1984. An orthopyroxene-garnet thermometer and its application to the Madras charnockites. Contributions to Mineralogy and Petrology 88(1–2), 64–71.

Simakin, A., Talbot, C., 2001. Tectonic pumping of pervasive granitic melts. Tectonophysics 332(4), 387-402.

Simakin, A., Talbot, C., 2001. Transfer of melt between microscopic pores and macroscopic veins in migmatites. Physics and Chemistry of the Earth, Part A: Solid Earth and Geodesy 26(4), 363-367.

Sisson, T.W. Ratajeski, K., Hankins, W.B., Glazner, A.F., 2005. Voluminous granitic magmas from common basaltic sources. Contributions to Mineralogy and Petrology 148(6), 635–661.

Springer, W., Seck, H.A., 1997. Partial fusion of basic granulites at 5 to 15 kbar: implications for the origin of TTG magmas. Contributions to Mineralogy and Petrology 127, 30–45.

Stevens, G., Clemens, J.D., Droop, G.T.R., 1997. Melt production during granulite-facies anatexis: Experimental data from "primitive'' metasedimentary protoliths. Contributions to Mineralogy and Petrology 128(4), 352-370.

Storkey, A.C., Hermann, J., Hand, M., Buick, I.S., 2005. Using in situ trace-element determinations to monitor partial-melting processes in metabasites. Journal of Petrology 46(6), 1283-1308.

Takamura, Y. Tsunogae, T., Santosh, M., Malaviarachchi, S.P., Tsutsumi, Y., 2015. Petrology and zircon U-Pb geochronology of metagabbro from the Highland Complex, Sri Lanka: Implications for the correlation of Gondwana suture zones. Journal of Asian Earth Sciences 113, 826–841.

Thost, D.E., Hensen, B.J., Motoyoshi, Y., 1991. Two-stage decompression in garnet-bearing mafic granulites from Sostrene Island, Prydz Bay, East Antarctica. Journal of Metamorphic Geology 9(3), 245-256.

Tracy, R.J., 1982. Compositional zoning and inclusions in metamorphic minerals. Reviews in Mineralogy and Geochemistry 10(1), 355-397.

Tuccillo, M.E., Essene, E.J., Van Der Pluijm, B.A., 1990. Growth and retrograde zoning in garnets from high-grade, metapelites: Implications for pressure-temperature paths. Geology,18(9), 839-842.

Vavra, G., Gebauer, D., Schmid, R., Compston, W., 1996. Multiple zircon growth and recrystallization during polyphase Late Carboniferous to Triassic metamorphism in granulites of the Ivrea Zone (Southern Alps): an ion microprobe (SHRIMP) study. Contributions to Mineralogy and Petrology 122(4), 337-358.

Vavra, G., Schmid, R., Gebauer, D., 1999. Internal morphology, habit and U-Th-Pb microanalysis of amphibolite-to-granulite facies zircons: geochronology of the Ivrea Zone (Southern Alps). Contributions to Mineralogy and Petrology 134(4), 380-404.

Watson, E.B., Harrison, T.M., 1983. Zircon saturation revisited: temperature and composition effects in a variety of crustal magma types. Earth and Planetary Science Letters, 64(2), 295-304.

Williams, I.S., 2001. Response of detrital zircon and monazite, and their U–Pb isotopic systems, to regional metamorphism and host-rock partial melting, Cooma Complex, southeastern Australia. Australian Journal of Earth Sciences, 48(4), 557-580.

Whitney, D.L., Evans, B.W., 2010. Abbreviations for names of rock-forming minerals. American Mineralogist 95, 185–187.

Wolf, M.B., Wyllie, P.J., 1994. Dehydration-melting of amphibolite at 10 kbar: the effects of temperature and time. Contributions to Mineralogy and Petrology 115(4), 369–383.

Xiong, X.L., 2006. Trace element evidence for the growth of early continental crust by melting of rutile-bearing hydrous eclogite. Geology 34(11), 945–948.

Zack, T., Moraes, R. Kronz, A., 2004. Temperature dependence of Zr in rutile: Empirical calibration of a rutile thermometer. Contributions to Mineralogy and Petrology 148(4), 471–488.

Zeng, L., Asimow, P.D., Saleeby, J.B., 2005. Coupling of anatectic reactions and dissolution of accessory phases and the Sr and Nd isotope systematics of anatectic melts from a metasedimentary source. Geochimica et Cosmochimica Acta 69(14), 3671-3682.

Figure captions

Figure 1: Geological map of Sri Lanka, copied from Takamura et al. (2015).

Table 1: Mineralogy of the samples studied.

Table 2: Microprobe (WDS) analyses of main phases. Total Fe listed as FeO and Fe. Oxides are listed in wt%; elements in a.p.f.u. (atom per formula unit); mes. is mesosome; sympl. is symplectite. Number of oxygen p.f.u. used for normalization is given in brackets behind the phase. X_{Mg} is defined as Mg/(Mg+Fe); Almandine as Fe/(Fe+Mg+Ca+Mn); Pyrope as Mg/(Fe+Mg+Ca+Mn); Spessartine as as Mn/(Fe+Mg+Ca+Mn); Grossular as Ca/(Fe+Mg+Ca+Mn).

Table 3: Microprobe (WDS) analyses of feldspar. Total Fe listed as FeO and Fe. Oxides are listed in wt%; elements in a.p.f.u. (atom per formula unit). Number of oxygen p.f.u. used for normalization is given in brackets behind the phase. Anorthite is defined as Ca/(Ca+Na+K); albite as Na/(Ca+Na+K); orthoclase as K/(Ca+Na+K). The remark "garnet" means the grain is located near the garnet porphyroblast; the remark "edge" means the grain is located on the other end of the symplectites (i.e. far from the garnet porphyroblast); incl. is short for inclusion; mes. is mesosome. Est. is an estimation of the composition of the mesoperthite before exsolution of K-feldspar.

Figure 2: An optical microscope image (PPL) of the transition from garnet to mesosome in sample 787. From the garnet porphyroblasts, first plagioclase + orthopyroxene symplectites occur, followed by a plagioclase and an orthopyroxene corona. The scale bar represents 200 µm.

Figure 3: Sample 787. An optical microscope image (PPL) showing deformation of a quartz band in the leucosome around a garnet porphyroblast located in the upper middle part of the image. The scale bar represents 200 µm.

Figure 4: An optical microscope image (PPL) showing the mesosome of sample 968. Note the well aligned amphibole grains (in dark brown) separated by pyroxene and plagioclase. The scale bar represents 200 µm.

Figure 5: An optical microscope image (PPL) of a retrogressed garnet porphyroblast in the leucosome in sample 968. Note the plagioclase + orthopyroxene symplectites surrounded by an orthopyroxene corona. The scale bar represents 200 µm.

Figure 6: An optical microscope image (PPL) of the foam textured leucosome in sample 280. Note the relatively small plagioclase and quartz grains with abundant 120° triple junctions. The scale bar represents 200 µm.

Figure 7: Sample 280. An optical microscope image (PPL) of a part of a large relatively unaltered garnet porphyroblast next to leucosome and mesosome. The scale bar represents 200 µm.

Figure 8: An optical microscope image (PPL) showing a pseudomorph after garnet in sample 280. The scale bar represents 200 µm.

Figure 9: Images of the matrix of sample 787. (A) is an electron backscatter map; (B) (C) and (D) are element maps (WDS) of Ca, Fe and K respectively. Minerals are listed in (A). Scale bar in the lower right corner is 1 mm. Note the zoning of plagioclase (B), especially near triple points of grains. In (C), note the difference between Opx, which is light blue, Cpx, which is dark blue, and biotite, which is slightly lighter in color than Cpx. Moreover, note the magnetite (green) exsolution in ilmenite (pink) visible in (C). In (D), note the exsolution of K-feldspar (pink) in plagioclase and subhedral biotite (green).

Figure 10: Images of garnet and adjacent symplectites in sample 787. (A) and (F) are electron backscatter maps; (B), (C), (D), (E) and (G) are element maps (WDS) of Ca, Fe, Mg, Mn and K respectively. Minerals are listed in (A) and (F). The scale bar in the lower right corner is 1 mm for all images except (F), where it is 0.2 mm. In (A), note the biotite needles in the lower left corner. In (B) the decrease in anorthite content in plagioclase from the garnet porphyroblast to the matrix is clearly visible. Moreover, note the K-feldspar in the symplectites, bordering both garnet and biotite (dark blue). Apatite is visible in white. In (C), note the slight outward increase in almandine content in the garnet. Furthermore, note the ilmenite both as an inclusion in garnet and with magnetite exsolution lamellae in the matrix (green). (D) shows the outward decrease in pyrope content in garnet; (E) shows the outward increase in spessartine content in garnet. (F) shows the K-feldspar located near garnet and biotite. (G) shows the K-feldspar bordering garnet and biotite, the large biotite grain and the biotite needles.

Figure 11: Images of garnet breakdown in sample 787. (A) is an electron backscatter map; (B), (C), (D), (E) and (F) are element maps (WDS) of Ca, Fe, K, Mg and Ti respectively. Minerals are listed in (A); the scale bar in the lower right corner is 1 mm. In (B), note apatite in pink. (C) shows magnetite in pink, ilmenite in green with magnetite exsolution lamellae. Ilmenite is surrounded by orthopyroxene in most places (see reaction 4). Moreover, note the slightly increased potassium content (D) and the decreased calcium content (B) in the course grained plagioclase with respect to symplectic plagioclase. In (D) K-feldspar is shown in light blue, bordering garnet, and biotite is shown in green.

Figure 12: A cross section through the leucosome in sample 787. (A) is an electron backscatter map; (B) and (C) are element maps (WDS) of Ca and K respectively. Minerals are listed in (A); the scale bar in the lower right corner is 1 mm. In (B), note the decrease in anorthite content in plagioclase from the garnet to the leucosome; the increase in anorthite content near the edge of plagioclase grains in the leucosome. In (C), note the antiperthite with K-feldspar in pink.

Figure 13: Electron backscatter image of inclusions in garnet, sample 787. The scale bar represents 0.5 mm. All the dark grey inclusions are quartz.

Figure 14: Images of the matrix of sample 968. (A) is an electron backscatter map; (B) (C), (D), (E), (F) and (G) are element maps (WDS) of Al, Ca, Fe, Na, Mg and Ti respectively. Minerals are listed in (A). Scale bar in the lower right corner is 0.5 mm. In (B), plagioclase is green, amphibole is blue and pyroxene is black, while in (C) plagioclase and amphibole are blue, while clinopyroxene is green and orthopyroxene is black. In (C), note the zoning of plagioclase, especially near triple points of grains, while amphibole is uniform in composition. Apatite is shown in pink. In (D), orthopyroxene is depicted in green, amphibole in light blue and clinopyroxene in dark blue. (G) shows ilmenite in green and rutile in pink.

Figure 15: An electron backscatter image (EDS) of garnet and surrounding symplectites and corona in the leucosome of sample 968. The scale bar represents 2 mm.

Figure 16: (A) is a representative optical microscope image (PPL) of the matrix of sample 280. (B) is an optical microscope image (PPL) of a typical garnet relict in sample 280. The scale bars represent 1 mm.

Figure 17: An optical microscope image (PPL) of a large and relatively intact garnet porphyroblast. The scale bar represents 4 mm.

Table 4: Shows the input for the pseudosections modelled with Perple_X in moles.

Figure 18: Pseudosection of sample 787 with overlain isopleths modelled using Perple_X. Microprobe mineral compositions have been used for the isopleths. Light and dark red indicates core and rim of garnet respectively; dark and light green indicates core and rim of feldspar respectively; dark and light purple

indicates mesosome orthopyroxene and maximum Al in orthopyroxene content in symplectites respectively. The box represents the change in phases with increasing temperature across the underlying lines.

Figure 19: Pseudosection of the symplectitic domains of sample 787, with overlain isopleths and modelled using Perple_X. Light and dark red indicates core and rim of garnet respectively; dark and light purple indicates mesosome orthopyroxene and maximum Al in orthopyroxene content in symplectites respectively.

Figure 20: Abundance of garnet (A), clinopyroxene (B) and orthopyroxene (C) in figure 18, in volume %.

Figure 21: Pseudosection of sample 968 with overlain isopleths modelled using Perple_X. Microprobe mineral compositions have been used for the isopleths. Light and dark red indicates core and rim of garnet respectively dark and light purple indicates mesosome orthopyroxene and maximum Al in orthopyroxene content in symplectites respectively. The boxes represent the changes in phases with increasing temperature across the underlying lines.

Figure 22: Abundance of garnet (A), clinopyroxene (B) and orthopyroxene (C) in figure 21, in volume %.

Figure 23: Pseudosection of sample 280 with overlain isopleths modelled using Perple_X. Due to the complexity of the pseudosection, not all fields are specified with an assemblage. Microprobe mineral compositions have been used for the isopleths. Dark and light red indicates core and rim of garnet respectively; the marked pink section represents peak conditions (see section 3.3.3). The box represents the change in phases with increasing temperature across the underlying lines.

Figure 24: Abundance of garnet in figure 23, in volume %.

Figure 25: Representative CL images of zircons from sample 968. (A) shows a zircon with a relatively gradual increase in brightness from core to rim. Figures (B) and (C) show dark cores within brighter rims. Figure (D) shows a bright core in a darker rim. Figure (E) shows a uniform bright zircon. Figures (F) and (G) show irregular sector zoning. Dark red circles show analyzed spots. The scale bars are 50 µm in size.

Figure 26: Representative CL images of zircons from sample 280. (A) and (B) show zircons with a darker core than rim. Figure (C) shows a bright core within a darker rim. Figure (D) shows a relatively uniform dark zircon. Figure (E) shows sector zoning and (F) shows concentric zoning with clear zircon crystal faces. Figure (G) shows firtree zoning and (H) shows a faint and partly overgrown oscillatory zoning. Dark red or white circles show analyzed spots. The scale bars are 50 µm in size.

Figure 27: Tera-Wasserburg Concordia diagram of zircons from sample 968. MSWD=Mean Square Weighted Deviation.

Figure 28: Tera-Wasserburg Concordia diagram of zircons from sample 968 with a Th/U of 0.01 to 0.07. MSWD=Mean Square Weighted Deviation.

Figure 29: Tera-Wasserburg Concordia diagram of zircons from sample 280. MSWD=Mean Square Weighted Deviation.

Figure 30: Histogram of $^{238}U/^{206}Pb$ ages of zircons from sample 968.

Figure 31: Histogram of $^{238}U/^{206}Pb$ ages of zircons from sample 280.

Table 5: LA-ICPMS trace element analyses of minerals in sample 787. Values are in ppm. Sympl. is symplectites; mes. is mesosome; leuc. is leucosome; edge means far from the garnet porphyroblast; bdl=below detection limit.

Table 6: LA-ICP-MS trace element analyses of minerals in sample 968. Values are in ppm. Sympl. is symplectites; mes. is mesosome; leuc. is leucosome; garnet means near the garnet porphyroblast; center means in the center of the leucosome; edge means far from the garnet porphyroblast; bdl=below detection limit.

Figure 32: Chondrite normalized REE plots of sample 787. A: Garnets 1 and 2 are depicted in blue and red respectively, with dark to light coloured lines being the transition from core to rim respectively. B: Blue is apatite; red is magnetite; green is ilmenite+magnetite. C: Different colours represent different symplectites. All the analyses are Pl+Opx except for the green which also includes Mt. D: Dark blue represents biotite in the symplectite, others are located in the matrix. E: Squares (blue and red) represents clinopyroxene; triangles (green and purple) represents orthopyroxene in the matrix. F: Dark colours represents cores and light colours represent rims. Yellow represents quartz; blue squares represents matrix plagioclase, cores are dark blue and the rim light blue; purple is a ternary feldspar; green triangles represents plagioclase from the leucosome; orange represents antiperthites from the leucosome; red diamonds represents plagioclase from symplectites.

Figure 33: Chondrite normalized REE plots of sample 968. A: Garnets 1 and 2 are depicted in blue and red respectively, with dark to light colours being the transition from core to rim. B: Blue is rutile; red and green are magnetite in the symplectites and matrix respectively. C: Different colours represent different symplectites. All the analyses are Pl+Opx except for the light blue, which also includes Mt. Dark blue and dark orange represent edges of symplectites, i.e. furthest away from the garnet porphyroblast; light orange and intermediate blue represent analyses near the garnet. D: Amphibole in different locations. E: Blue represents clinopyroxene; red represents orthopyroxene in the matrix; orange represents orthopyroxene in the symplectites; green represent orthopyroxene in the corona. F: Dark colours represents cores and light colours represent rims. Yellow represents quartz; red and orange represents matrix plagioclase; blue represents plagioclase from the leucosome; green represents plagioclase from symplectites.

Table 7: Comparison of results from thermobarometry and Perple_X modelling. [1]: Ellis & Green (1979); [2]: Sen & Bhattacharya (1984); [3]: Ferry & Spear (1978); [4]: Zack et al. (2004); [5]: Henry et al. (2005); [6]: Moecher et al. (1988). NA: Not Available (due to the absence of a mineral in the sample). In the upper three rows, garnet core composition was used, while in the lower three rows garnet rim and biotite needle composition was used. Except for biotite needles, different biotite compositions did not give significantly different results.

Appendix 1: LA-ICP-MS analyses of zircons from sample 968. Values of 0.0 are below 0.0 but above detection limit. B in the analysis name is the fraction 180-250 µm, S is the fraction 120-180 µm and H is the fraction 90-120 µm. A, B, C and D indicates multiple analysis locations in a single zircon grain.

Appendix 2: LA-ICP-MS analyses of zircons from sample 280. Values of 0.0 are below 0.0 but above detection limit. P in the analysis name is the fraction 180-250 µm, O is the fraction 120-180 µm and I is the fraction 90-120 µm. A, B, C and D indicates multiple analysis locations in a single zircon grain.

Figures

Figure 1

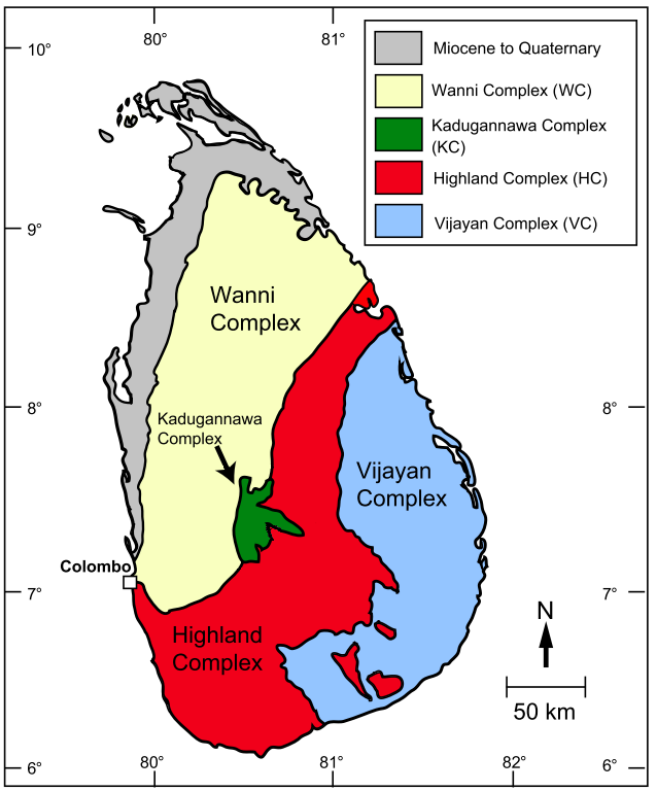

Table 1

	Main phases							Accessory phases						
Sample	Grt	Pl	Qtz	Opx	Cpx	Bt	Amp	Kfs	Ap	Mt	Ilm	Rt	Zrn	Ttn
787	X	X	X	X	X	X		X	X	X	X	X	X	
968	X	X	X	X	X		X		X	X	X	X	X	
280	X	X	X	X		X	X		X	X	X	X	X	X

Table 2

Mineral	Garnet (12O)						Biotite (22O)						Amphibole (23O)		Orthopyroxene (6O)					Clinopyroxene (6O)	
Sample	787		U968		U280		787				U280		U968	U280	787	787	U280	U968	U968	787	U968
Remark	Core	Rim	Core	Rim	Core	Rim	Mes. core	Mes. rim	Sympl.	Needle	Near garnet	Needle			Mes.	Sympl.	Mes.	Mes.	Corona+sympl.		
Na2O	0.01	0.00	0.00	0.03	0.00	0.02	0.05	0.05	0.03	0.03	0.02	0.03	1.46	1.40	0.00	0.03	0.00	0.00	0.02	0.39	0.49
Al2O3	21.74	21.59	21.73	21.76	20.99	20.97	13.13	13.25	14.50	14.13	14.57	14.30	11.13	11.61	1.73	3.47	1.04	1.59	3.40	2.60	2.85
CaO	5.14	4.19	7.47	4.63	6.16	5.76	0.01	0.07	0.02	0.07	0.00	0.08	11.40	10.86	0.35	0.72	0.45	0.60	0.32	21.49	21.83
MgO	8.45	7.29	8.76	7.59	4.54	4.34	13.56	15.76	16.62	18.89	12.63	12.85	12.67	9.61	19.90	20.06	16.63	23.29	21.00	12.74	14.17
FeO	25.23	27.96	22.78	25.76	28.31	28.64	15.95	12.50	12.18	11.42	17.68	18.28	13.70	18.69	27.59	24.21	31.69	22.11	24.48	10.93	8.61
TiO2	0.06	0.00	0.07	0.01	0.02	0.02	5.88	4.82	4.86	2.44	5.77	4.28	2.87	2.05	0.09	0.04	0.06	0.13	0.03	0.30	0.43
SiO2	38.50	38.26	38.97	38.62	37.42	37.11	36.71	38.33	37.67	38.55	35.92	36.42	41.99	41.07	50.79	52.25	49.49	51.71	50.40	50.71	51.07
MnO	0.73	1.57	1.06	2.54	2.78	3.05	0.04	0.01	0.05	0.02	0.10	0.08	0.12	0.26	0.46	0.40	0.90	0.43	0.82	0.18	0.20
K2O	0.00	0.00	0.00	0.00	0.00	0.00	10.11	10.09	10.51	10.53	10.37	10.26	1.72	1.59	0.00	0.00	0.00	0.00	0.00	0.00	0.00
ZrO2	0.00	0.03	0.00	0.01	0.00	0.00	0.00	0.00	0.00	0.00	0.00	0.01	0.00	0.01	0.04	0.04	0.01	0.06	0.00	0.00	0.04
Cr2O3	0.07	0.03	0.14	0.04	0.02	0.02	0.16	0.04	0.02	0.20	0.00	0.01	0.40	0.03	0.04	0.16	0.00	0.08	0.28	0.06	0.15
Cl	0.01	0.01	0.00	0.01	0.00	0.00	0.00	0.00	0.00	0.06	0.00	0.00	0.18	0.00	0.00	0.00	0.00	0.00	0.00	0.00	0.01
Total	99.93	100.93	100.99	100.99	100.25	99.92	95.60	94.92	96.46	98.12	97.32	96.84	97.78	97.18	100.99	101.36	100.27	100.00	100.74	99.40	99.86
Fe	1.62	1.80	1.44	1.65	1.86	1.90	2.06	1.59	1.52	1.41	2.26	2.34	1.71	2.39	0.87	0.75	1.03	0.68	0.76	0.34	0.27
Na	0.00	0.00	0.00	0.00	0.00	0.00	0.01	0.01	0.01	0.01	0.01	0.01	0.42	0.41	0.00	0.00	0.00	0.00	0.00	0.03	0.04
Al	1.97	1.96	1.94	1.97	1.95	1.96	2.39	2.38	2.55	2.45	2.63	2.58	1.96	2.09	0.08	0.15	0.05	0.07	0.15	0.12	0.12
Ca	0.42	0.35	0.61	0.38	0.52	0.49	0.00	0.01	0.00	0.01	0.00	0.01	1.83	1.78	0.01	0.03	0.02	0.02	0.01	0.87	0.87
Mg	0.97	0.84	0.99	0.87	0.53	0.51	3.12	3.58	3.70	4.14	2.88	2.94	2.83	2.19	1.11	1.11	0.96	1.29	1.16	0.72	0.78
Ti	0.00	0.00	0.00	0.00	0.00	0.00	0.68	0.55	0.55	0.27	0.66	0.49	0.32	0.24	0.00	0.00	0.00	0.00	0.00	0.01	0.01
Si	2.96	2.95	2.95	2.96	2.95	2.94	5.67	5.84	5.63	5.68	5.50	5.58	6.28	6.28	1.91	1.93	1.92	1.92	1.88	1.91	1.90
Mn	0.05	0.10	0.07	0.16	0.19	0.20	0.01	0.00	0.01	0.00	0.01	0.01	0.02	0.03	0.01	0.01	0.03	0.01	0.03	0.01	0.01
K	0.00	0.00	0.00	0.00	0.00	0.00	1.99	1.96	2.00	1.98	2.03	2.01	0.33	0.31	0.00	0.00	0.00	0.00	0.00	0.00	0.00
Zr	0.00	0.00	0.00	0.00	0.00	0.00	0.00	0.00	0.00	0.00	0.00	0.00	0.00	0.00	0.00	0.00	0.00	0.00	0.00	0.00	0.00
Cr	0.00	0.00	0.01	0.00	0.00	0.00	0.02	0.00	0.00	0.02	0.00	0.00	0.05	0.00	0.00	0.00	0.00	0.00	0.01	0.00	0.00
Cl	0.00	0.00	0.00	0.00	0.00	0.00	0.00	0.00	0.00	0.01	0.00	0.00	0.05	0.00	0.00	0.00	0.00	0.00	0.00	0.00	0.00
Tot. cation	8.03	8.05	8.05	8.04	8.05	8.06	15.96	15.93	15.97	15.98	15.99	15.98	15.73	15.78	4.03	3.99	4.04	4.03	4.03	4.02	4.03
XMg	0.37	0.32	0.41	0.34	0.22	0.21	0.60	0.69	0.71	0.75	0.56	0.56	0.62	0.48	0.56	0.60	0.48	0.65	0.60	0.68	0.75
Alm	0.53	0.56	0.44	0.52	0.58	0.59															
Py	0.33	0.28	0.33	0.29	0.18	0.17															
Spess	0.02	0.03	0.02	0.06	0.06	0.07															
Gross	0.14	0.12	0.20	0.13	0.18	0.17															

Table 3

Mineral	Feldspar (8 oxygen)																							
Sample	787		787			787					787			U968						U280 rim				
Location	Mesosome		Mesosome - ternary			Leucosome		Antiperthite			Symplectite	787 edge	Incl. Garnet	Mesosome		Symplectite		Leucosome		Mesosome		Incl. Garnet	Leucosome	
Remark	Core	Rim	Kfs	Core	Rim	Core	Rim	Kfs (30%)	Pl (70%)	Est.	Near garnet	Edge		Core	Rim	Garnet	Edge	Core	Rim	Core	Rim			
Na2O	5.71	5.12	0.24	5.27	2.98	5.89	5.05	0.58	5.53	4.04	1.45	3.04	4.95	4.86	3.04	1.51	5.23	4.93	5.39	5.30	2.26	4.96	5.25	
Al2O3	27.08	28.17	18.41	27.70	31.48	27.73	28.35	19.56	27.73	25.28	34.15	31.66	28.89	28.98	32.06	34.30	28.54	28.17	27.20	28.26	32.84	28.83	28.51	
CaO	9.39	10.52	0.09	10.47	14.87	9.57	10.14	0.11	9.96	7.00	17.11	14.46	10.85	11.24	14.55	16.93	10.50	11.40	10.67	10.68	15.92	11.16	10.70	
MgO	0.01	0.00	0.00	0.01	0.05	0.00	0.05	0.00	0.02	0.02	0.01	0.00	0.03	0.01	0.03	0.08	0.00	0.00	0.01	0.02	0.01	0.02	0.00	
FeO	0.15	0.31	0.04	0.22	0.25	0.15	0.20	0.09	0.20	0.17	0.46	0.26	0.40	0.14	0.50	0.63	0.32	0.17	0.18	0.18	0.21	0.68	0.13	
TiO2	0.01	0.00	0.01	0.00	0.02	0.00	0.02	0.04	0.01	0.01	0.00	0.00	0.00	0.00	0.00	0.00	0.01	0.00	0.00	0.00	0.02	0.00	0.00	
SiO2	56.22	54.45	64.54	55.27	49.63	56.10	55.01	65.52	54.77	58.00	46.07	49.38	54.59	53.89	49.71	46.26	54.92	55.50	56.47	54.28	47.51	53.89	54.38	
MnO	0.01	0.00	0.01	0.01	0.00	0.00	0.00	0.00	0.00	0.00	0.02	0.00	0.01	0.00	0.00	0.02	0.01	0.00	0.00	0.00	0.00	0.03	0.01	
K2O	0.62	0.46	16.89	0.50	0.19	0.40	0.38	16.51	0.24	5.12	0.08	0.17	0.44	0.40	0.21	0.06	0.42	0.38	0.38	0.34	0.11	0.30	0.35	
ZrO2	0.00	0.01	0.00	0	0	0.00	0.00	0.02	0.05	0.04	0.00	0.01	0.04	0.01	0.00	0.00	0.00	0.00	0.00	0.02	0.03	0.02	0.07	
Cr2O3	0.00	0.01	0.01	0	0	0.00	0.00	0.00	0.00	0.00	0.00	0.00	0.00	0.00	0.02	0.00	0.00	0.00	0.00	0.00	0.00	0.01	0.00	
Cl	0.00	0.00	0.00	0	0	0.00	0.01	0.01	0.00	0.00	0.01	0.00	0.00	0.01	0.00	0.00	0.00	0.00	0.00	0.01	0.01	0.00	0.00	
Total	99.21	99.04	100.24	99.461	99.473	99.84	99.23	102.43	98.53	99.70	99.37	98.98	100.20	99.56	100.12	99.79	99.95	100.56	100.34	99.09	98.93	99.91	99.45	
Fe	0.01	0.01	0.00	0.00	0.01	0.01	0.01	0.00	0.01	0.01	0.02	0.01	0.01	0.01	0.02	0.02	0.01	0.01	0.01	0.01	0.01	0.03	0.00	
Na	0.50	0.45	0.02	0.49	0.20	0.51	0.45	0.05	0.49	0.36	0.13	0.27	0.35	0.43	0.27	0.13	0.46	0.43	0.47	0.47	0.20	0.44	0.46	
Al	1.45	1.51	1.00	1.47	1.76	1.47	1.52	1.04	1.49	1.36	1.86	1.72	1.23	1.55	1.72	1.86	1.52	1.49	1.44	1.51	1.79	1.54	1.52	
Ca	0.46	0.51	0.00	0.48	0.79	0.46	0.49	0.01	0.49	0.34	0.85	0.71	0.42	0.55	0.71	0.84	0.51	0.55	0.51	0.52	0.79	0.54	0.52	
Mg	0.00	0.00	0.00	0.00	0.01	0.00	0.00	0.00	0.00	0.00	0.00	0.00	0.00	0.00	0.00	0.01	0.00	0.00	0.00	0.00	0.00	0.00	0.00	
Ti	0.00	0.00	0.00	0.00	0.00	0.00	0.00	0.00	0.00	0.00	0.00	0.00	0.00	0.00	0.00	0.00	0.00	0.00	0.00	0.00	0.00	0.00	0.00	
Si	2.55	2.48	2.98	2.53	2.21	2.52	2.50	2.95	2.50	2.64	2.13	2.28	1.97	2.45	2.27	2.13	2.48	2.50	2.54	2.47	2.20	2.44	2.47	
Mn	0.00	0.00	0.00	0.00	0.00	0.00	0.00	0.00	0.00	0.00	0.00	0.00	0.00	0.00	0.00	0.00	0.00	0.00	0.00	0.00	0.00	0.00	0.00	
K	0.04	0.03	0.99	0.03	0.01	0.02	0.02	0.95	0.01	0.29	0.00	0.01	0.02	0.02	0.01	0.00	0.02	0.02	0.02	0.02	0.01	0.02	0.02	
Zr	0.00	0.00	0.00	0.00	0.00	0.00	0.00	0.00	0.00	0.00	0.00	0.00	0.00	0.00	0.00	0.00	0.00	0.00	0.00	0.00	0.00	0.00	0.00	
Cr	0.00	0.00	0.00	0.00	0.00	0.00	0.00	0.00	0.00	0.00	0.00	0.00	0.00	0.00	0.00	0.00	0.00	0.00	0.00	0.00	0.00	0.00	0.00	
Cl	0.00	0.00	0.00	0.00	0.00	0.00	0.00	0.00	0.00	0.00	0.00	0.00	0.00	0.00	0.00	0.00	0.00	0.00	0.00	0.00	0.00	0.00	0.00	
Tot. cation	5.00	5.00	5.02	5.00	5.01	5.01	4.98	5.02	5.00	5.01	5.00	5.00	3.75	5.00	5.01	5.00	5.00	4.99	4.99	5.01	5.01	5.01	5.01	
An	0.46	0.52	0.00	0.48	0.79	0.46	0.51	0.01	0.49	0.34	0.86	0.72	0.53	0.55	0.72	0.86	0.51	0.55	0.51	0.52	0.79	0.54	0.52	
Ab	0.51	0.46	0.02	0.49	0.20	0.51	0.46	0.05	0.49	0.36	0.13	0.27	0.44	0.43	0.27	0.14	0.46	0.43	0.47	0.46	0.20	0.44	0.46	
Or	0.04	0.03	0.97	0.03	0.01	0.02	0.02	0.94	0.01	0.30	0.00	0.01	0.03	0.02	0.01	0.00	0.02	0.02	0.02	0.02	0.01	0.02	0.02	

Figure 2

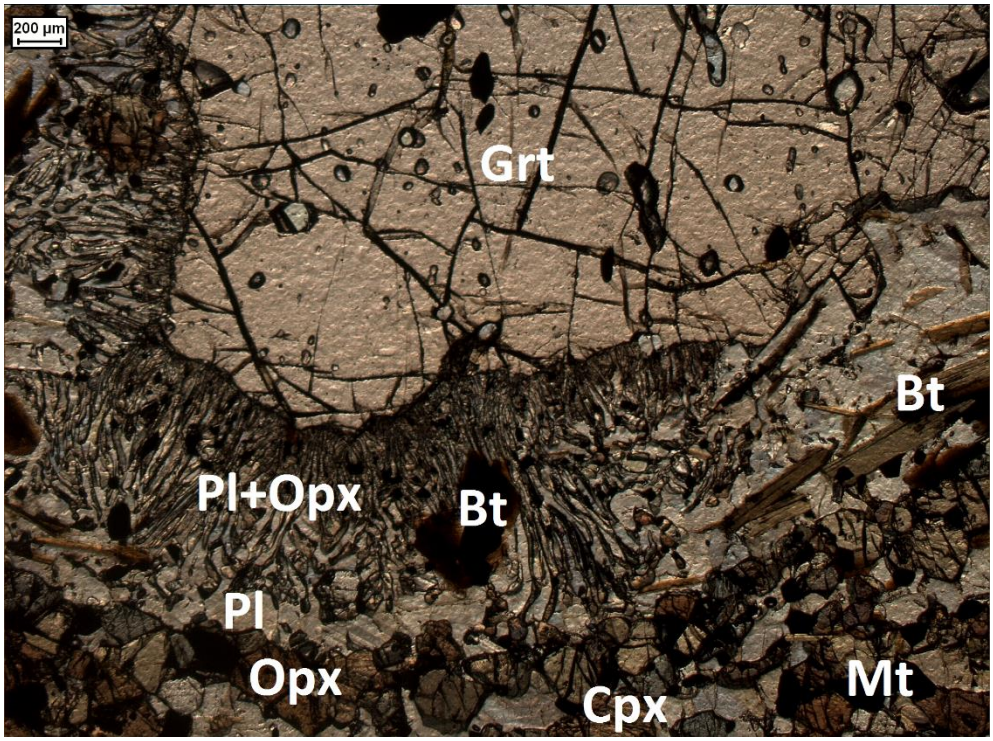

Figure 3

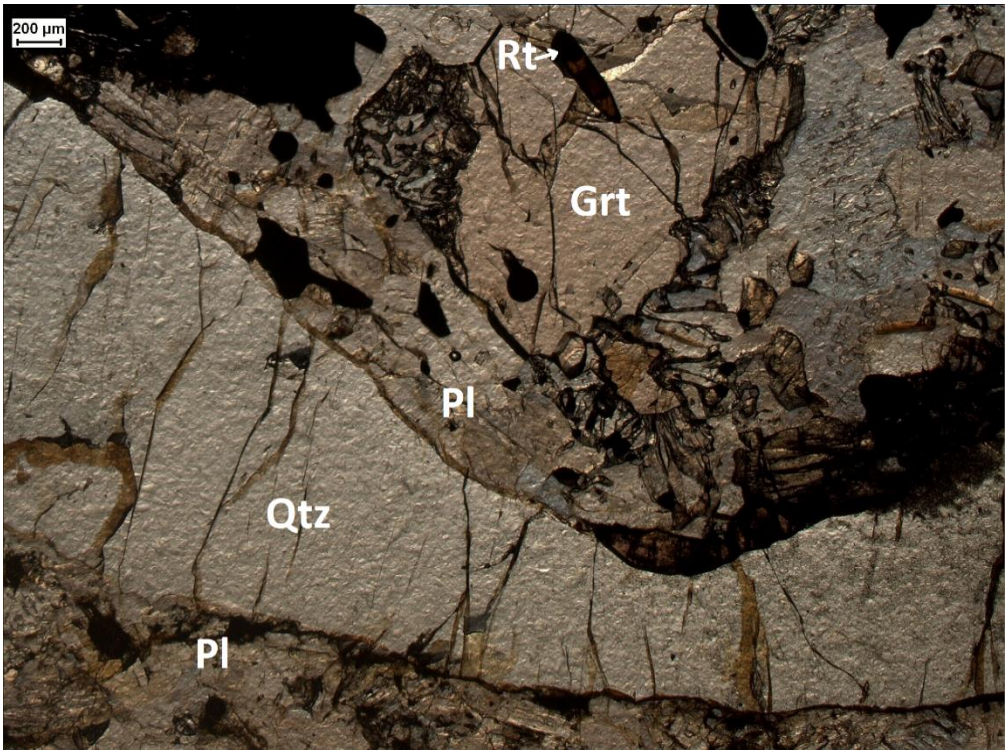

Figure 4

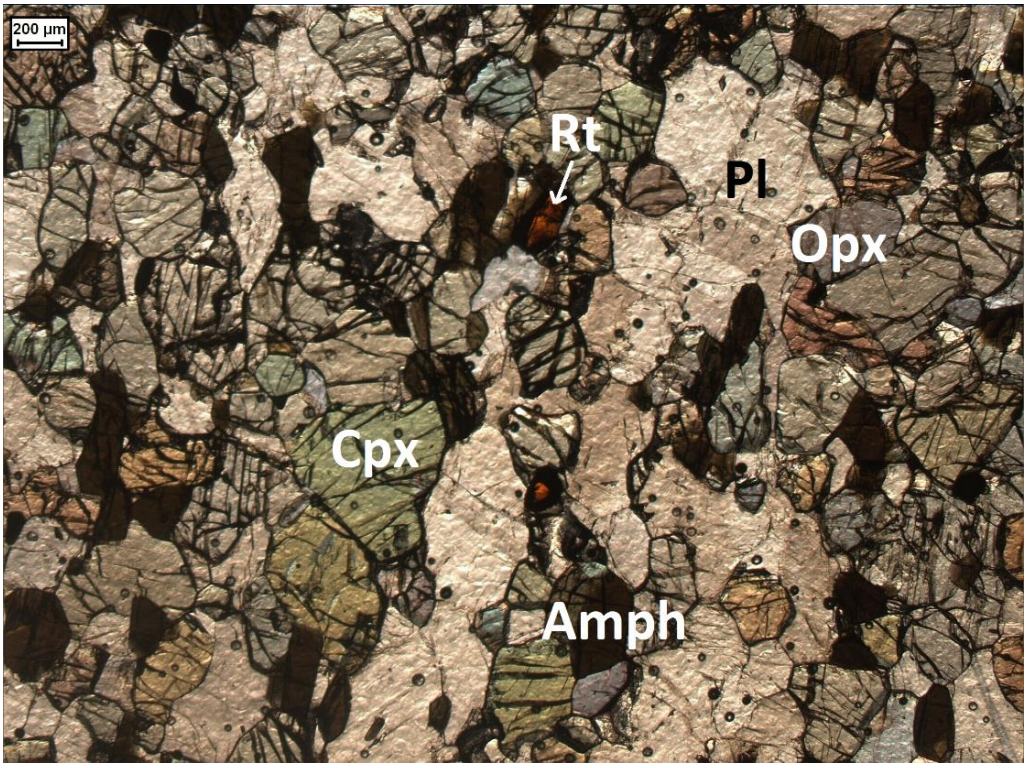

Figure 5

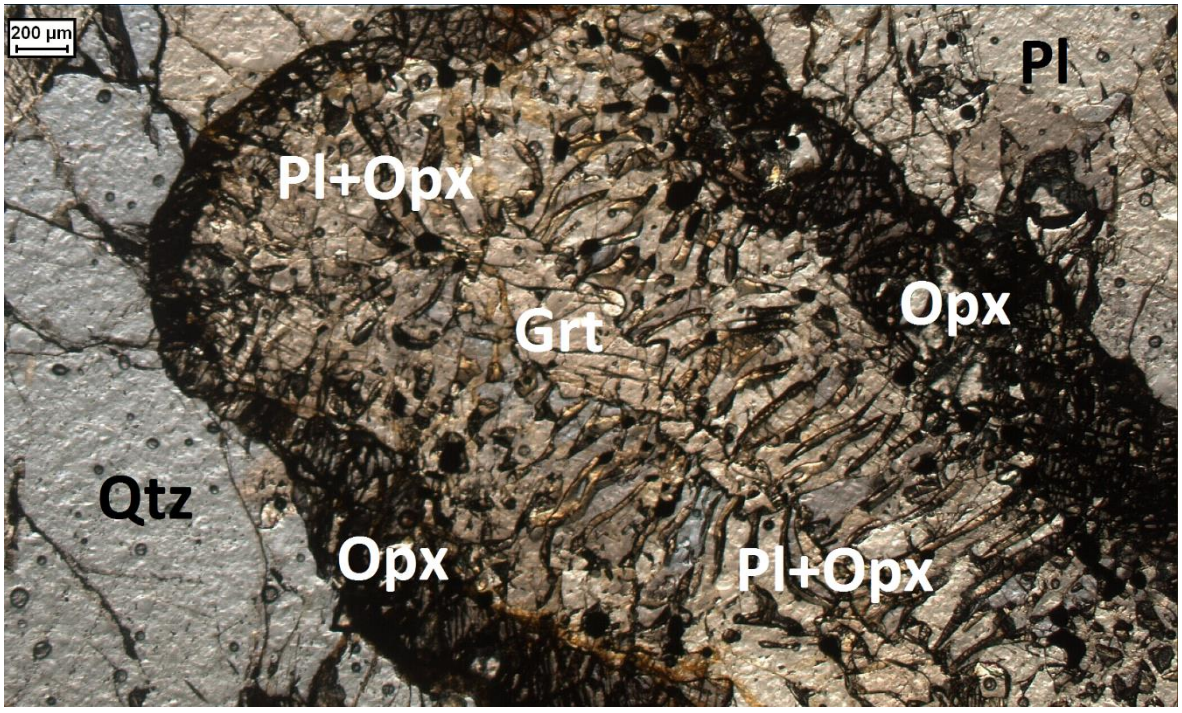

Figure 6

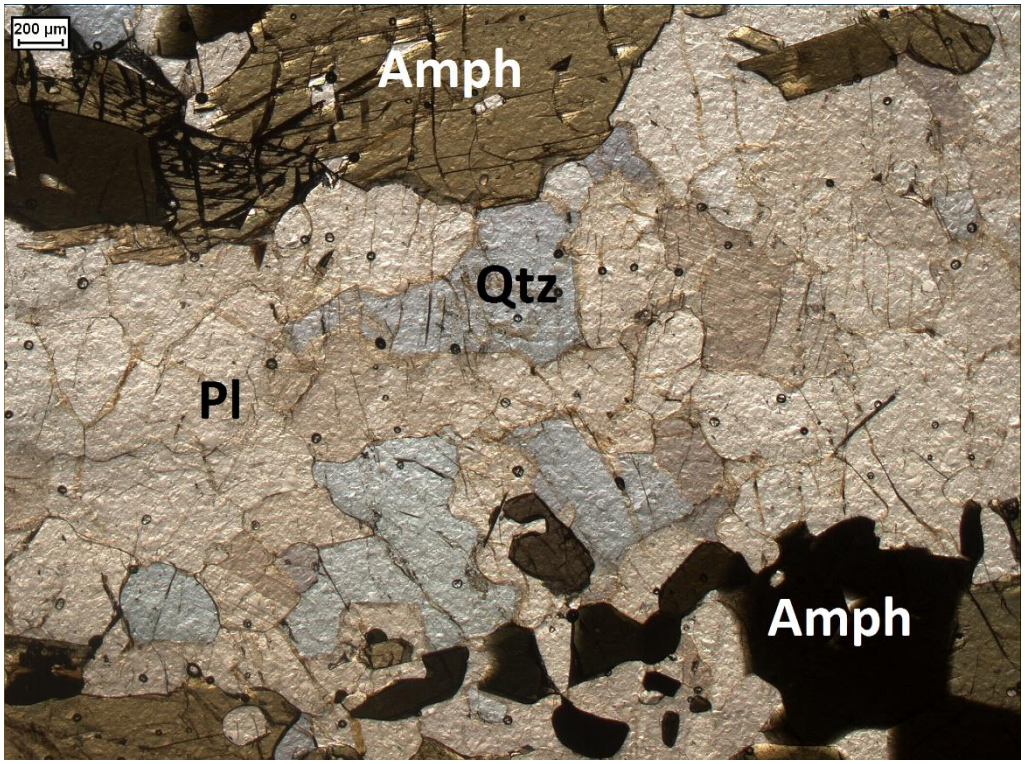

Figure 7

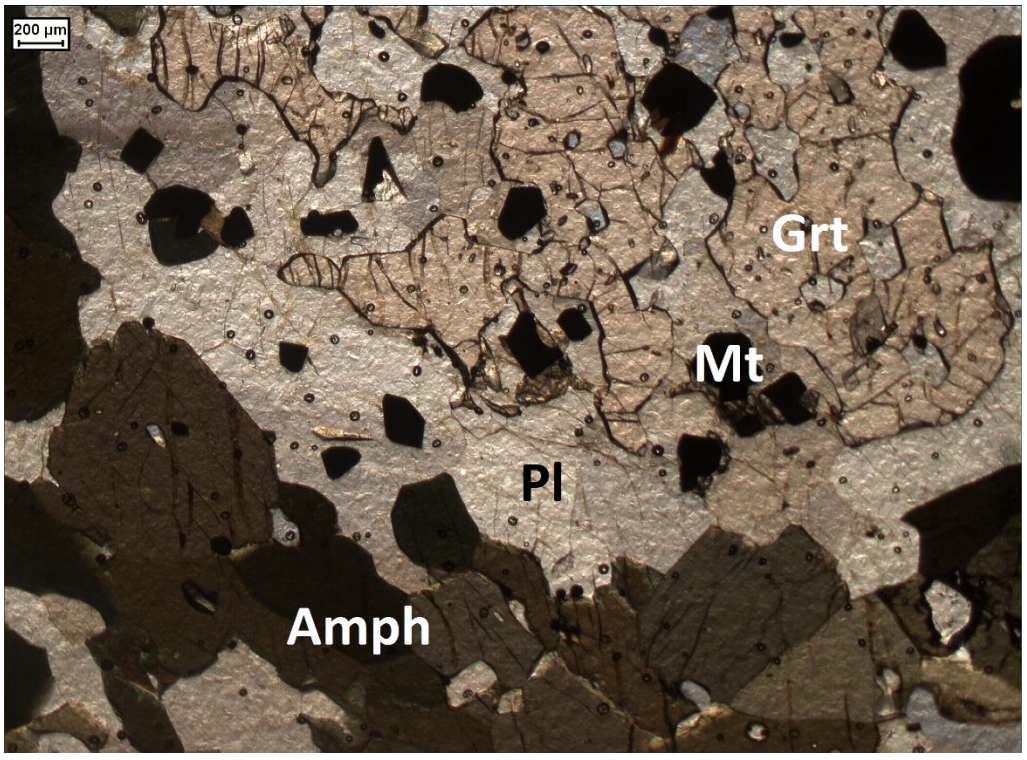

Figure 8

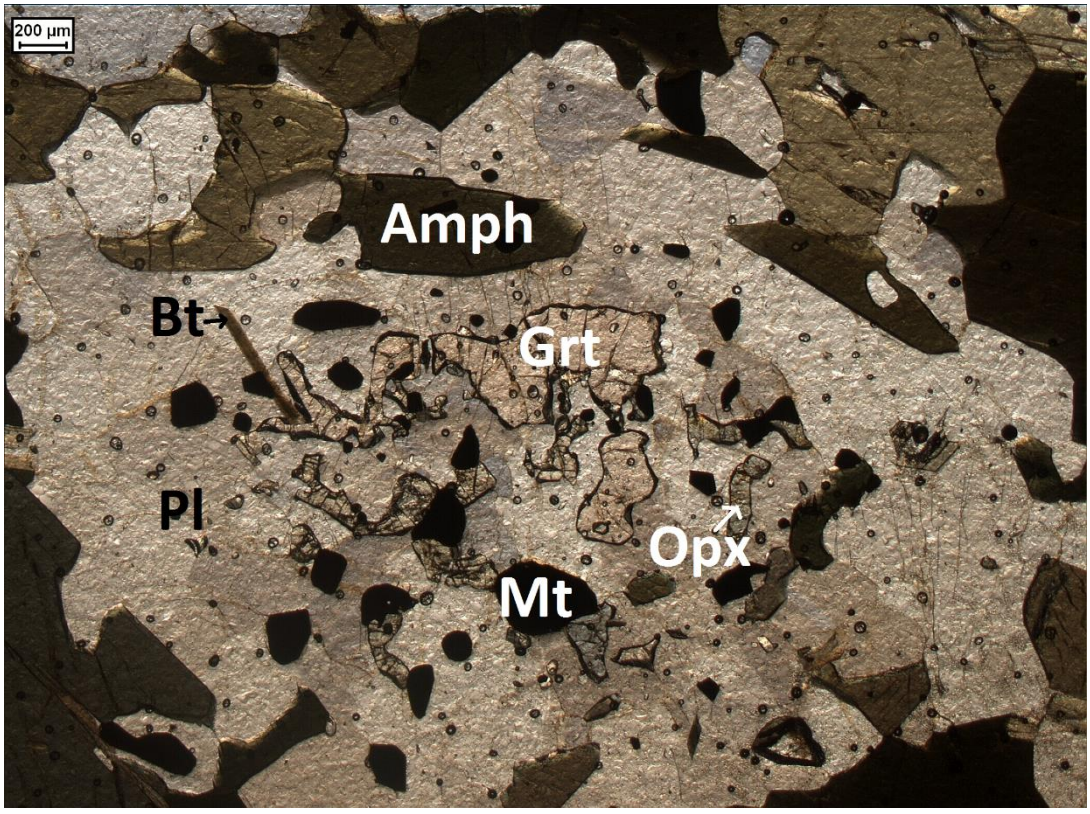

Figure 9

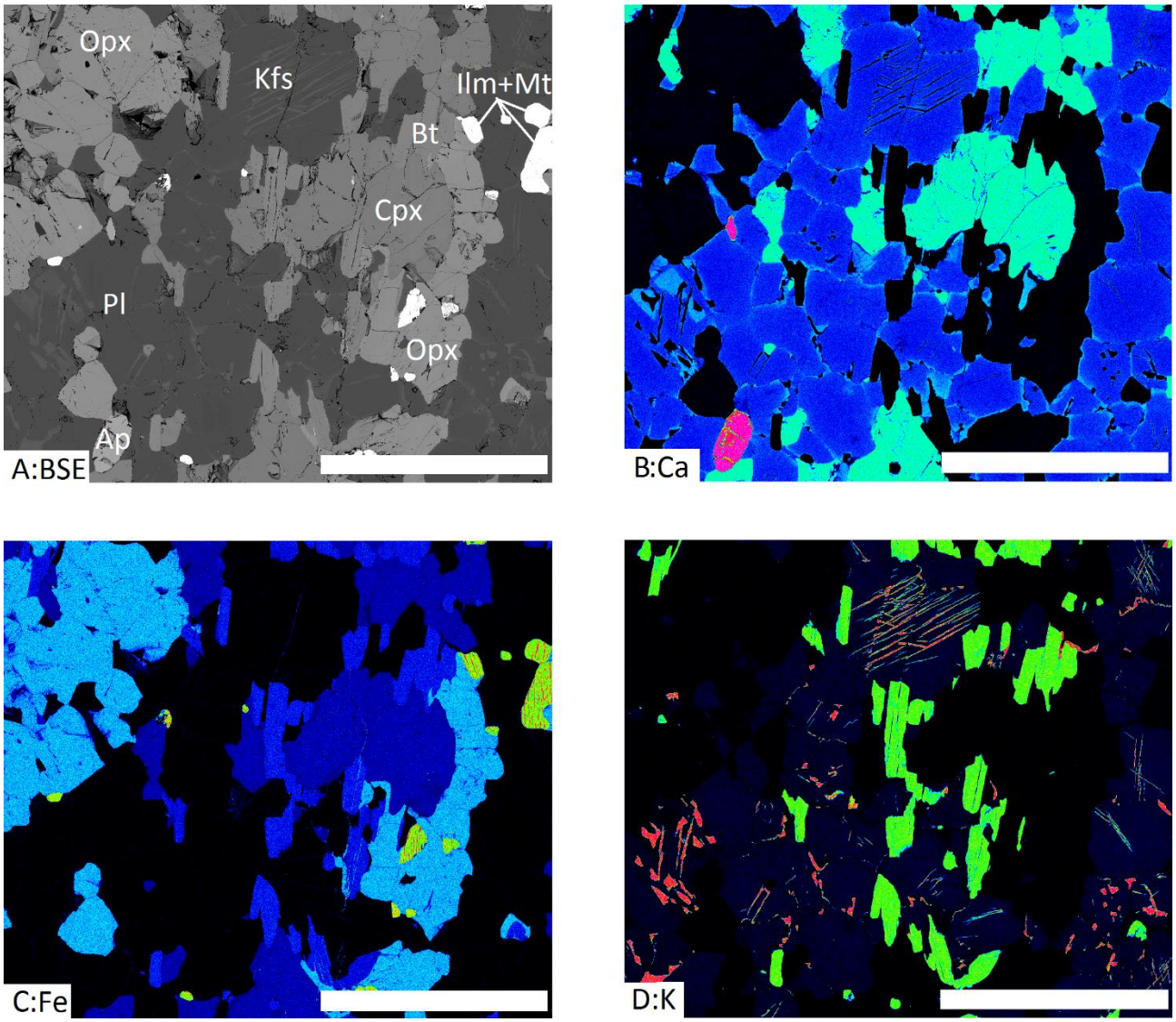

Figure 10

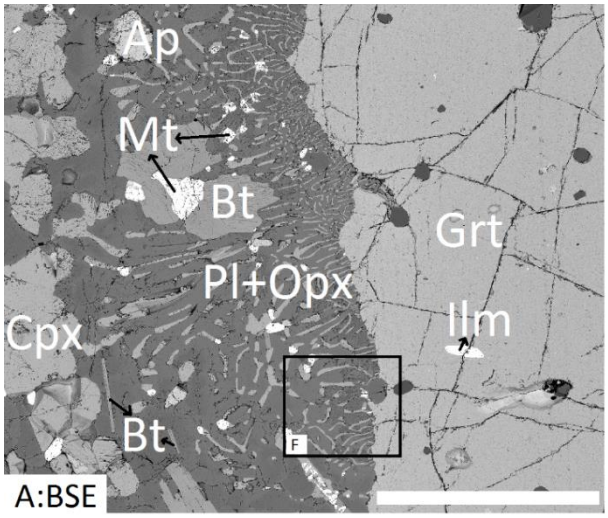
Ap
Mt
Bt
Grt
Pl+Opx
Ilm
Cpx
Bt
F
A:BSE

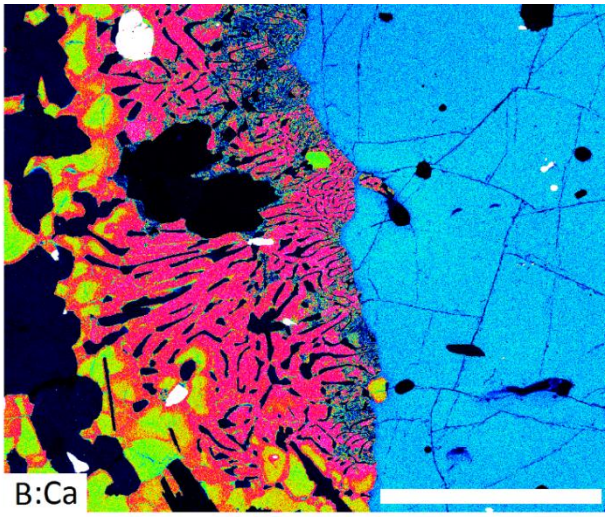
B:Ca

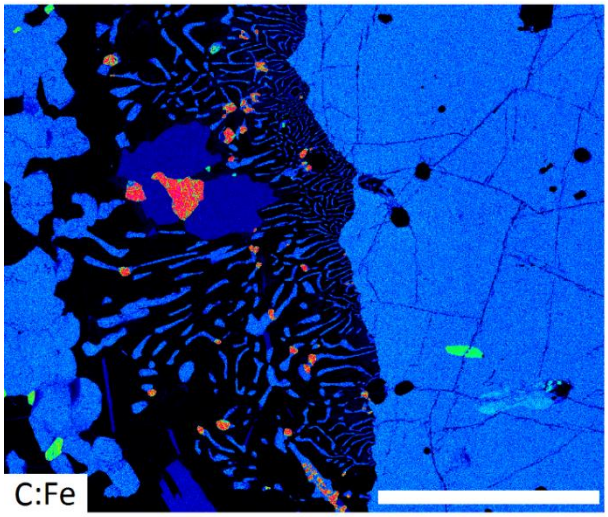
C:Fe

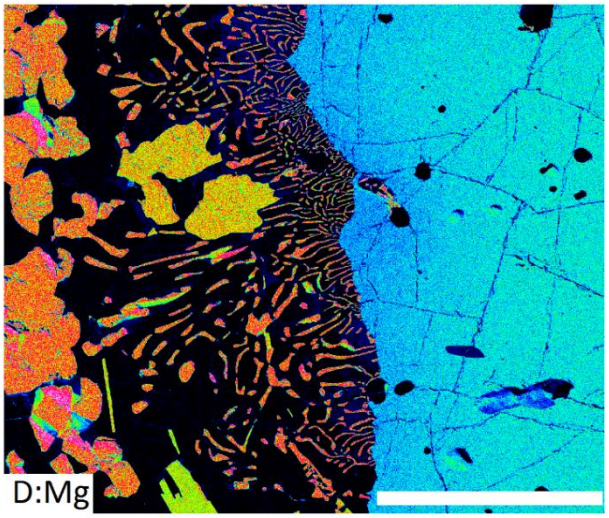
D:Mg

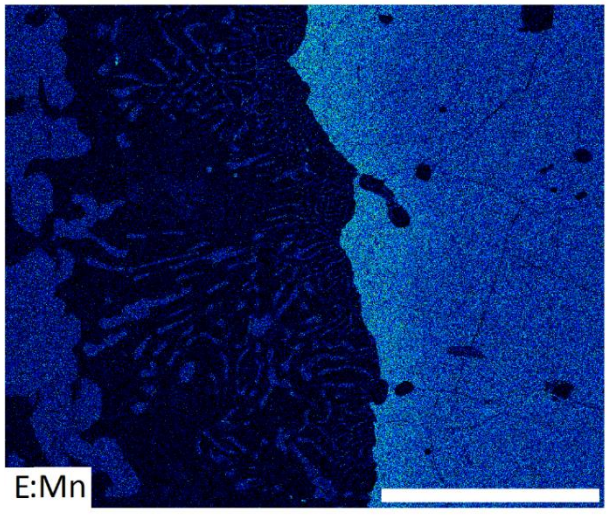
E:Mn

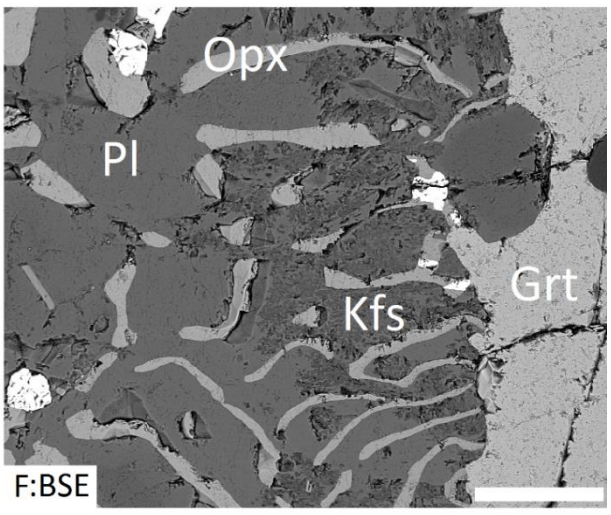
Opx
Pl
Grt
Kfs
F:BSE

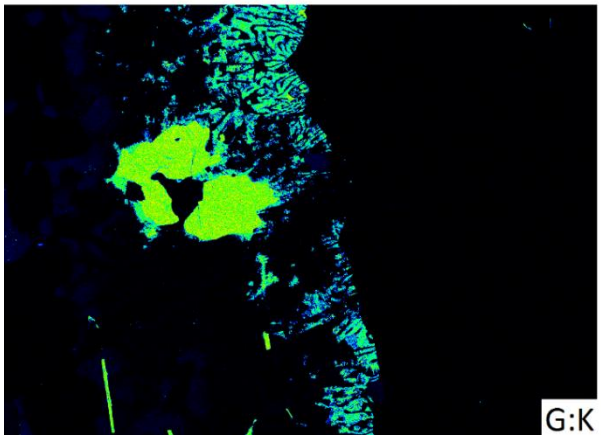
G:K

Figure 11

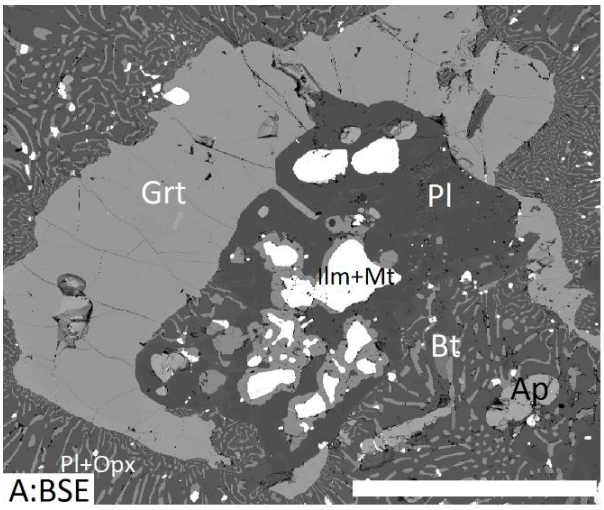

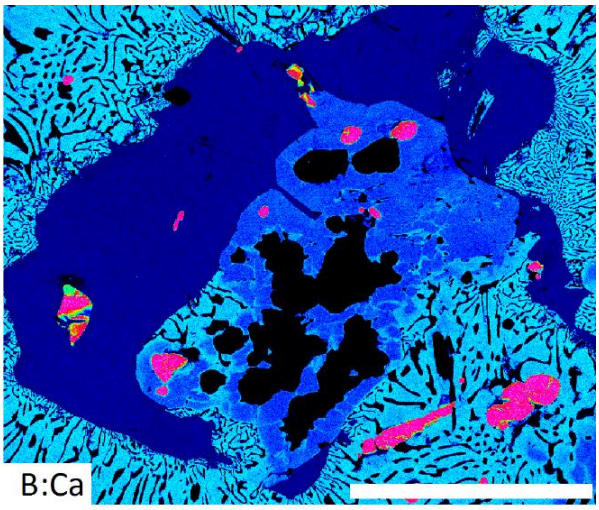

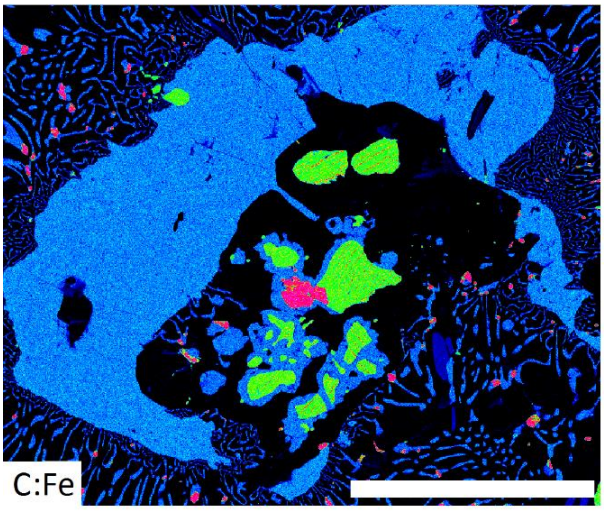

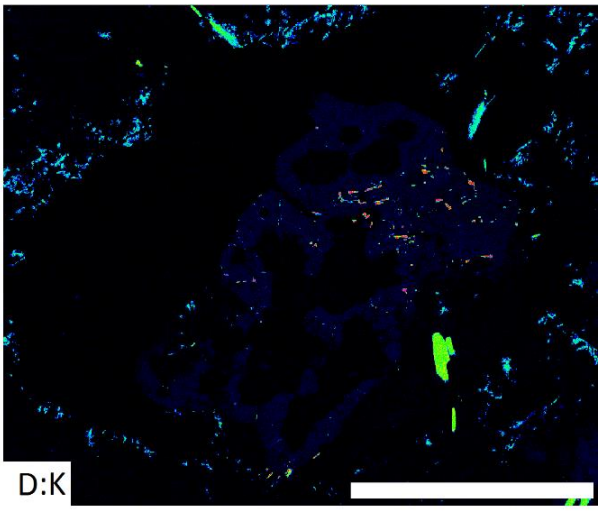

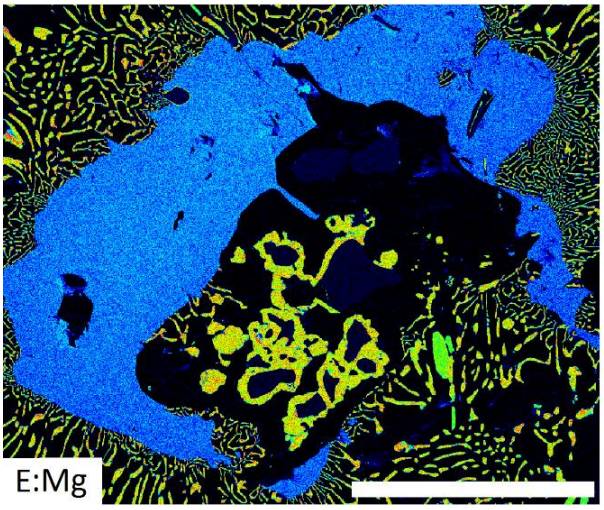

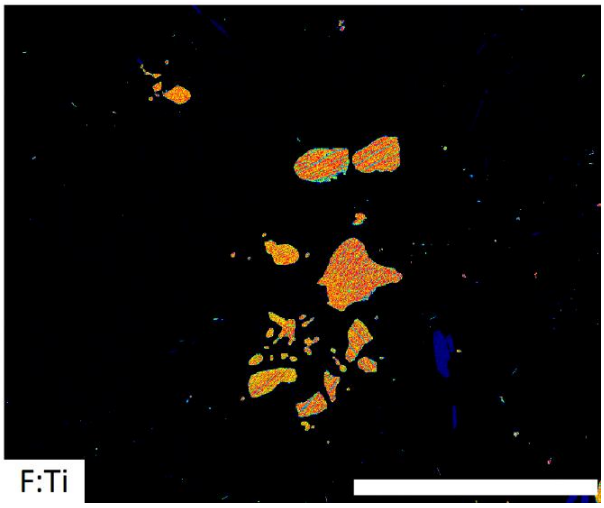

Figure 12

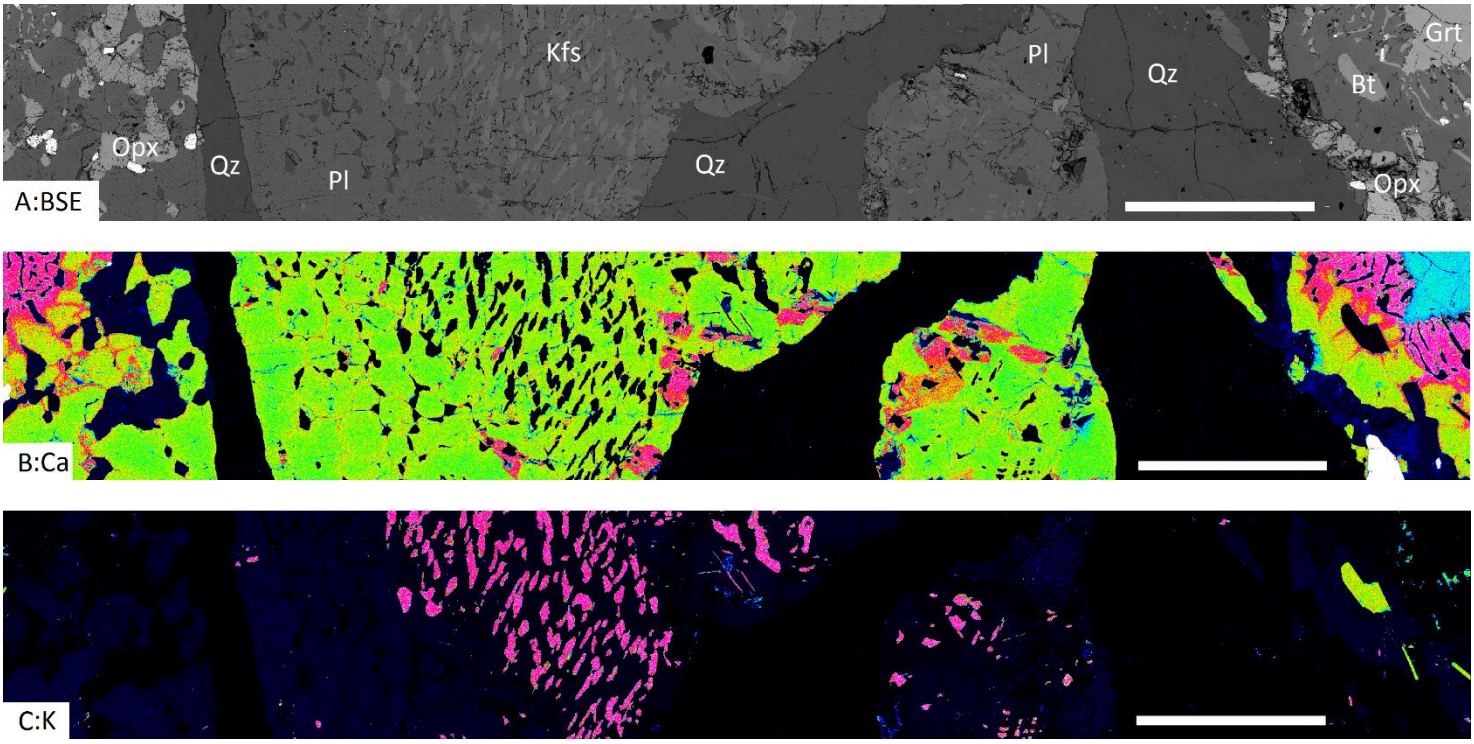

Figure 13

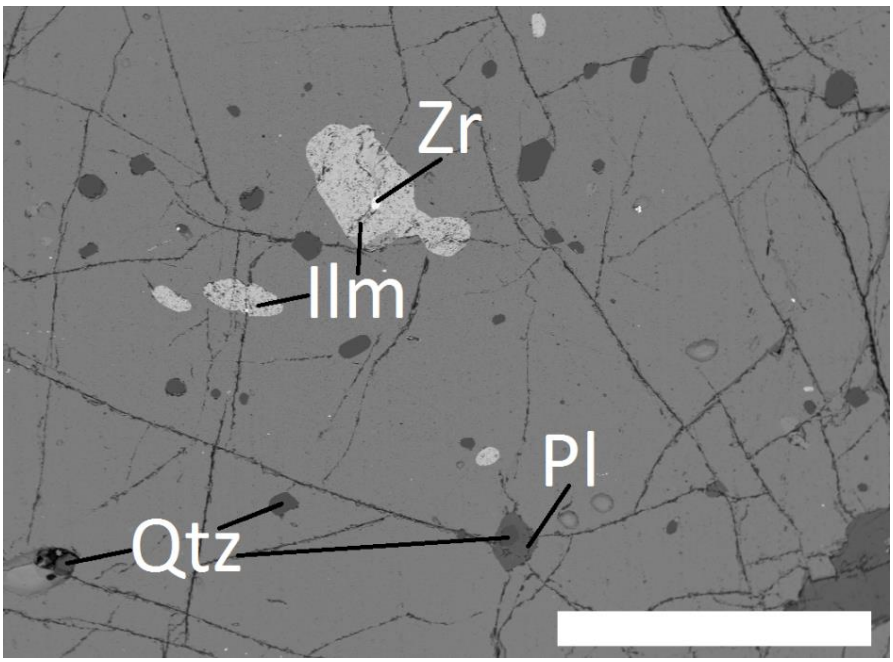

Figure 14

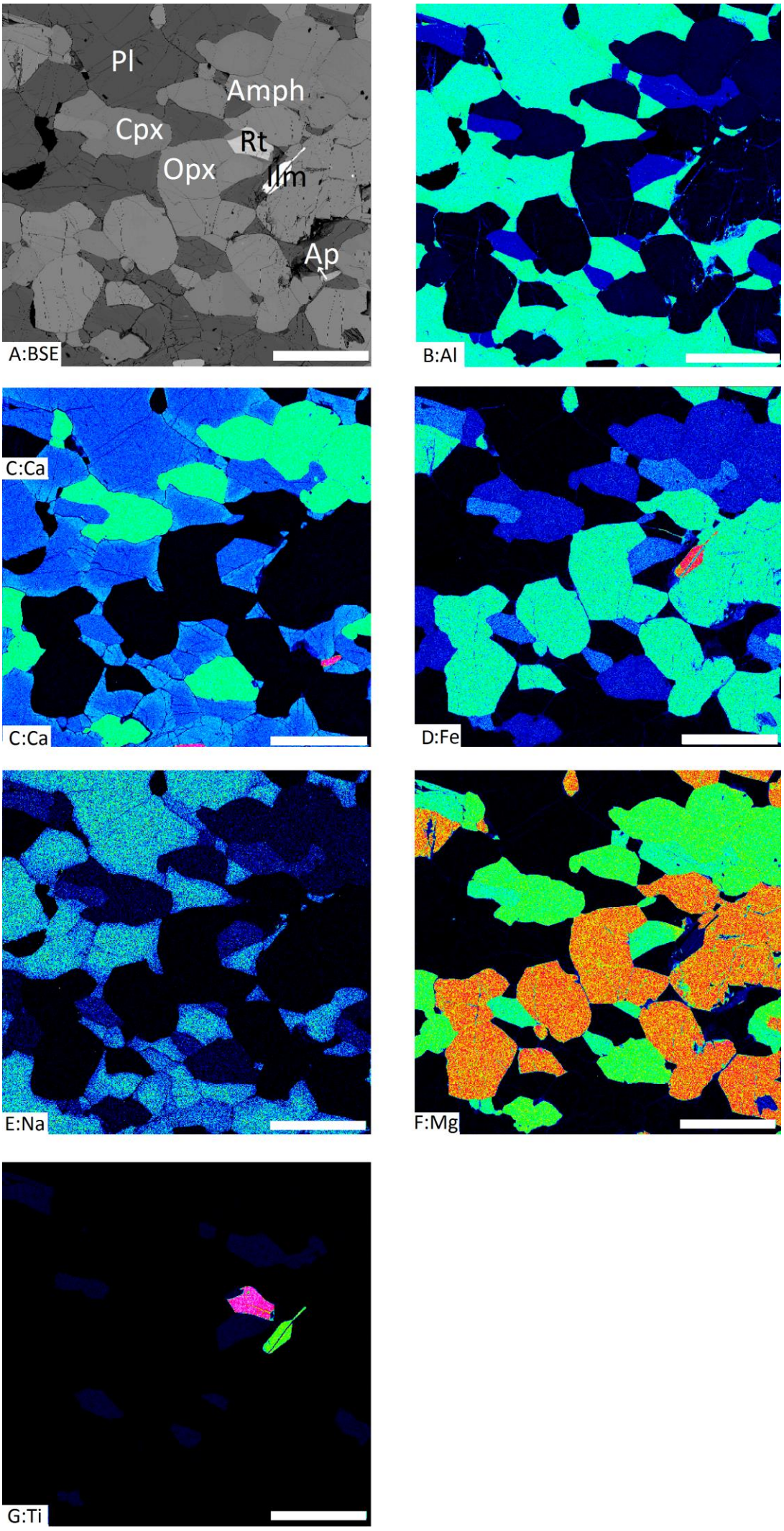

Figure 15

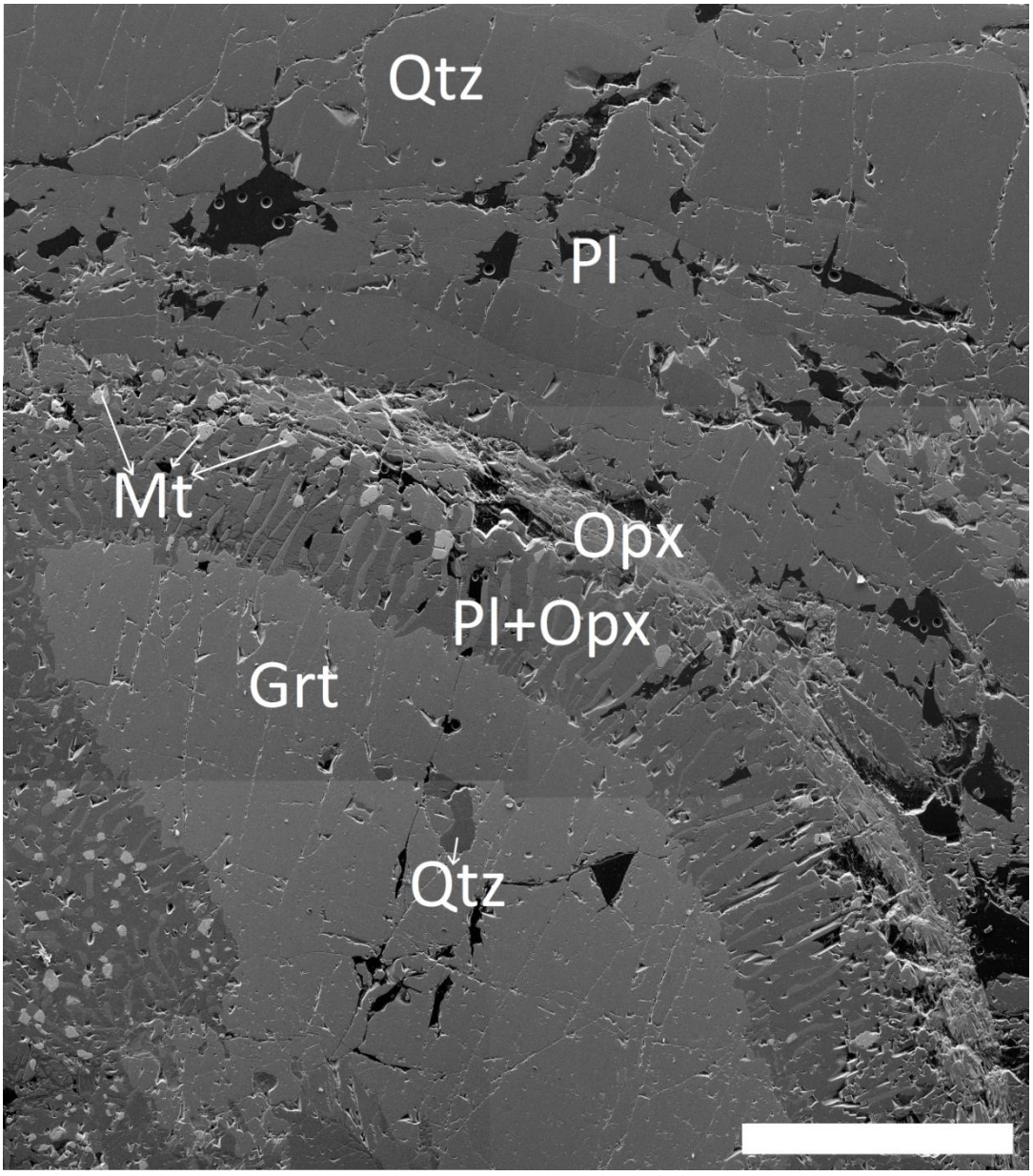

Figure 16

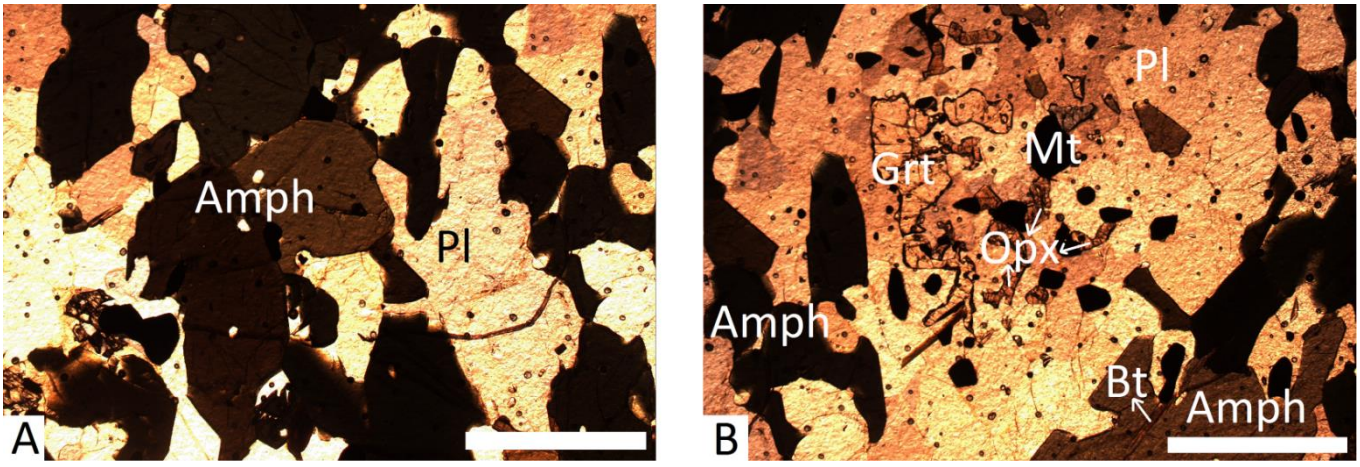

Figure 17

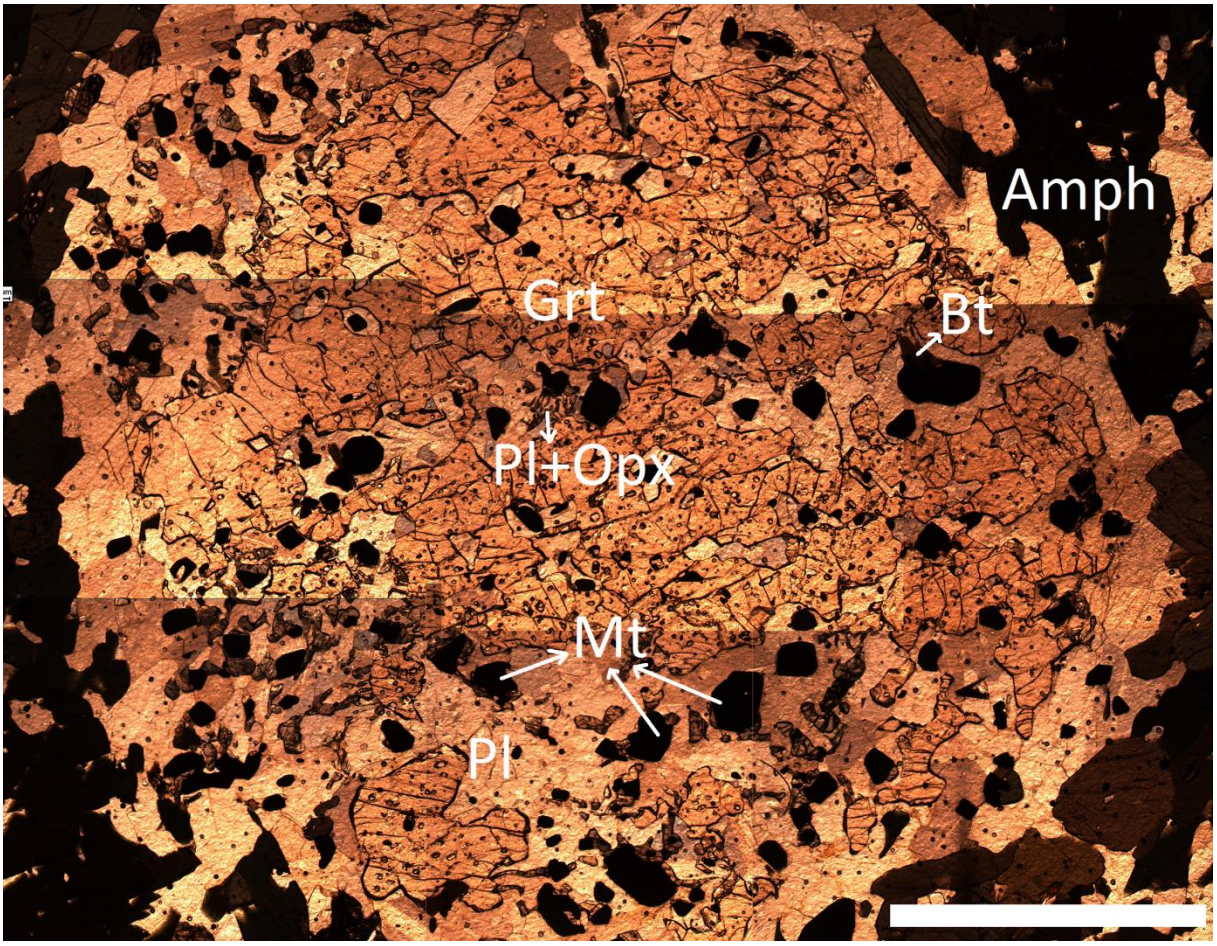

Table 4

	FeO	Na2O	Al2O3	CaO	MgO	TiO2	SiO2	MnO	K2O	ZrO2	Cr2O3	Cl	F	H2O
787	0.62	0.04	0.36	0.35	0.69	0.07	2.49	0.02	0.05	0.00	0.00	0.00	0.01	0.07
968	0.47	0.06	0.31	0.51	0.76	0.07	2.46	0.01	0.01	0.00	0.00	0.00	0.00	0.07
280	0.63	0.08	0.42	0.44	0.41	0.11	2.53	0.01	0.04	0.00	0.00	0.00	0.00	0.39
787sympl	0.66		0.45	0.29	0.63		3.03							

Figure 18

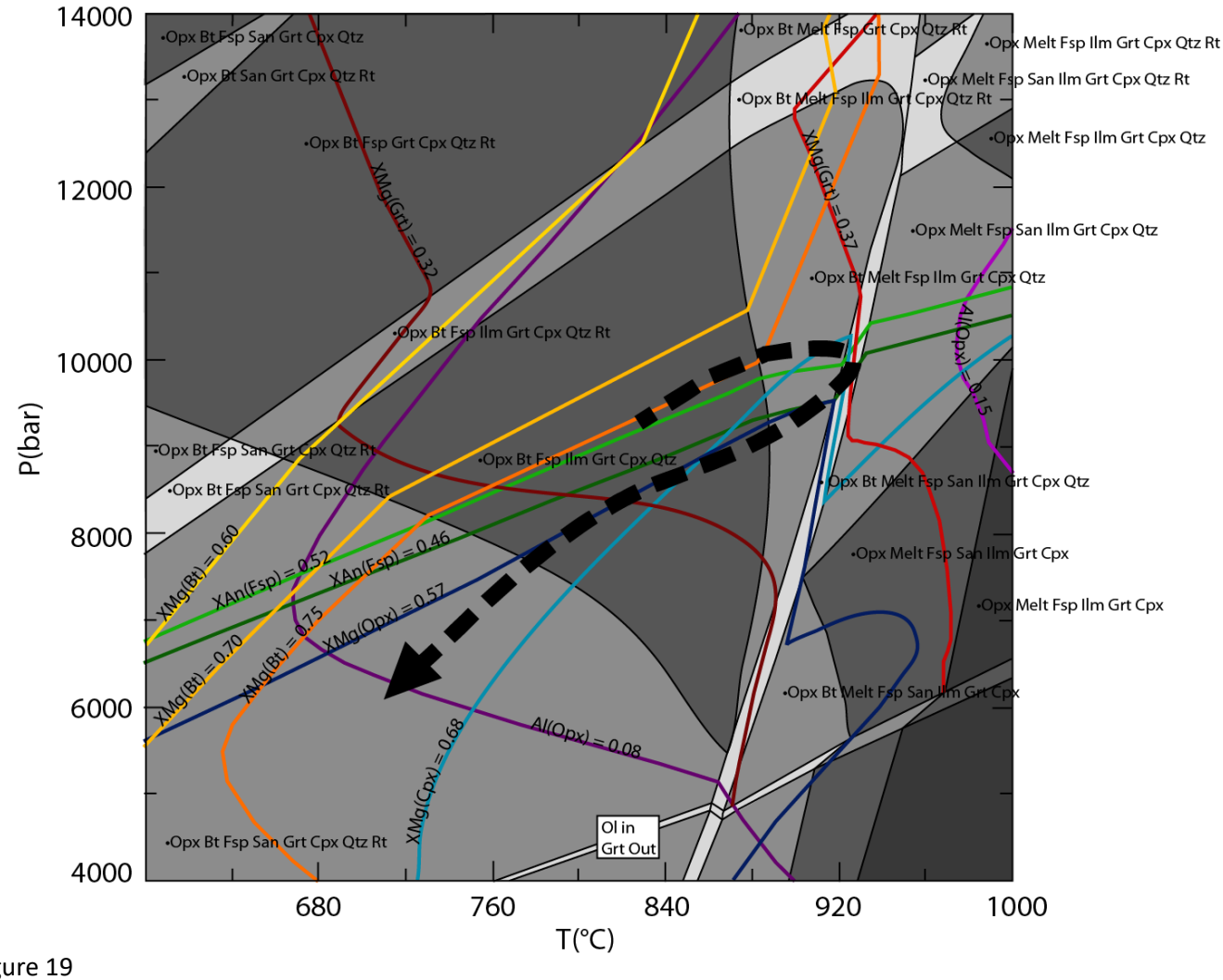

Figure 19

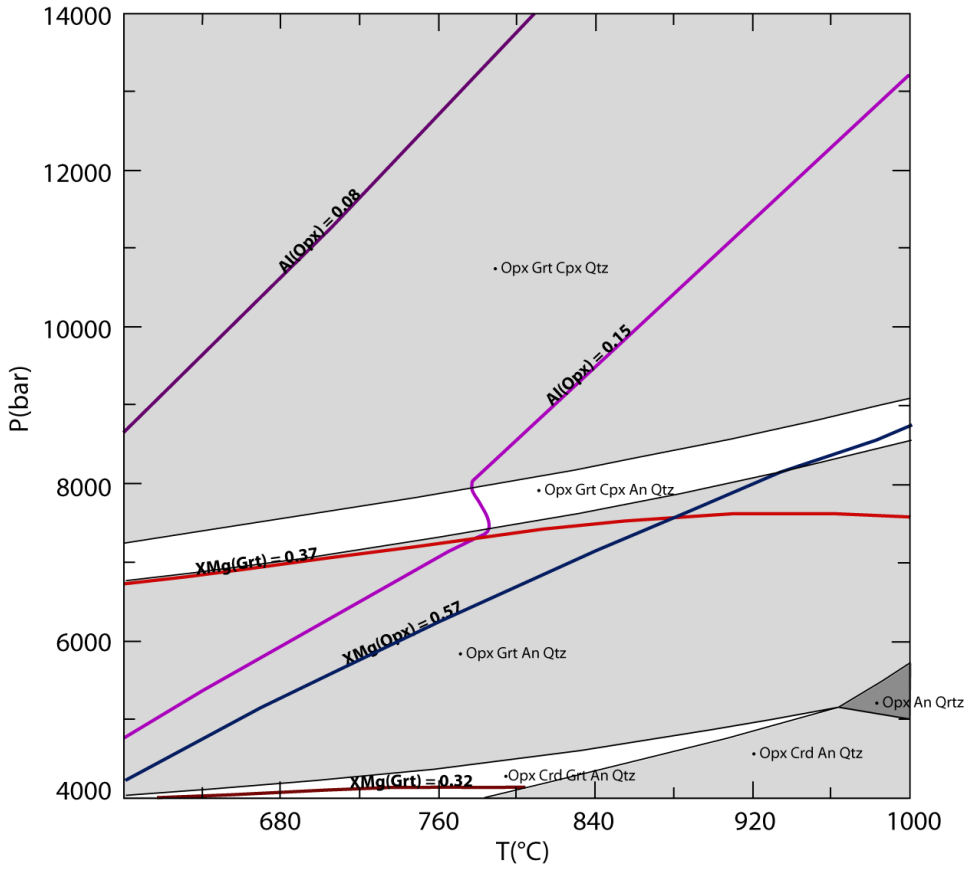

Figure 20

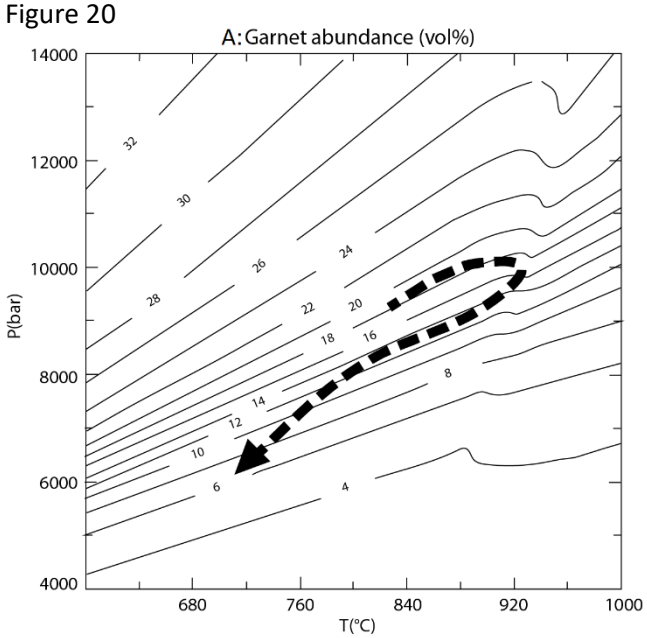
A: Garnet abundance (vol%)
P(bar)
T(°C)
14000
12000
10000
8000
6000
4000
680
760
840
920
1000
32
30
28
26
24
22
20
18
16
14
12
10
8
6
4

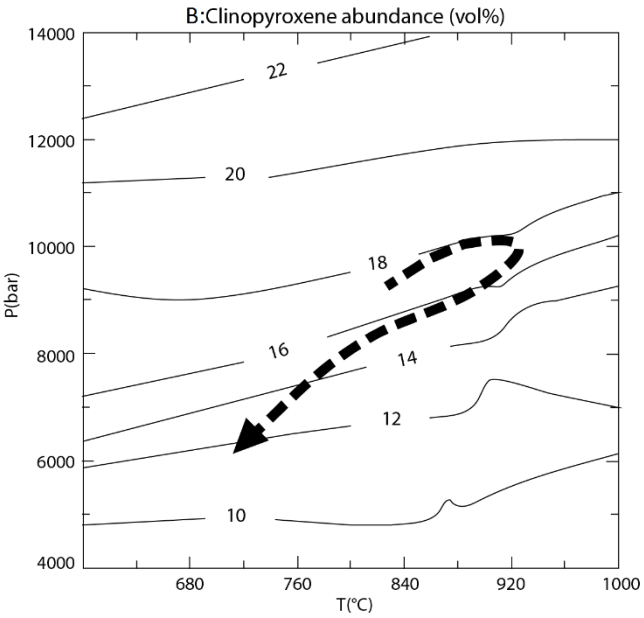
B: Clinopyroxene abundance (vol%)
P(bar)
T(°C)
14000
12000
10000
8000
6000
4000
680
760
840
920
1000
22
20
18
16
14
12
10

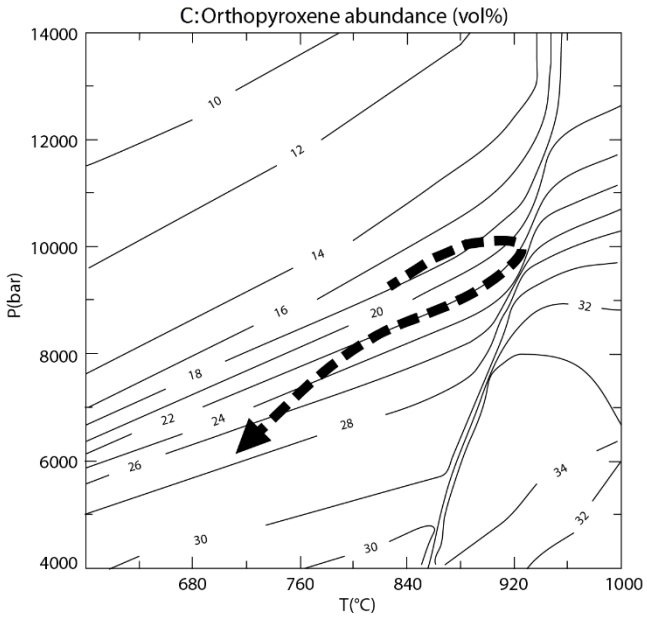
C: Orthopyroxene abundance (vol%)
P(bar)
T(°C)
14000
12000
10000
8000
6000
4000
680
760
840
920
1000
10
12
14
16
18
20
22
24
26
28
30
32
34

Figure 21

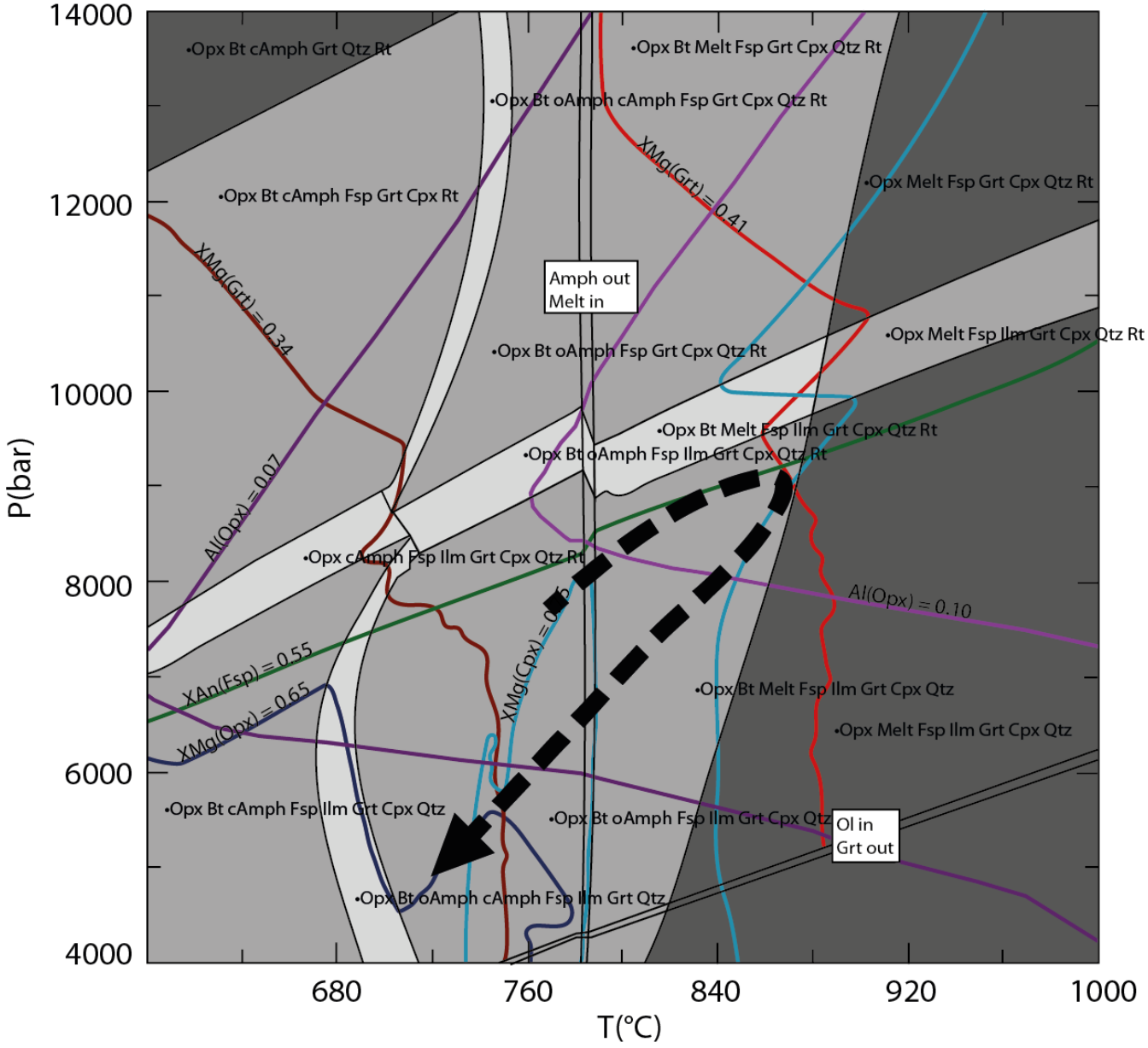
14000
12000
10000
8000
6000
4000
P(bar)
680
760
840
920
1000
T(°C)
•Opx Bt cAmph Grt Qtz Rt
•Opx Bt Melt Fsp Grt Cpx Qtz Rt
•Opx Bt oAmph cAmph Fsp Grt Cpx Qtz Rt
•Opx Bt cAmph Fsp Grt Cpx Rt
•Opx Melt Fsp Grt Cpx Qtz Rt
XMg(Grt) = 0.41
XMg(Grt) = 0.34
Amph out
Melt in
•Opx Bt oAmph Fsp Grt Cpx Qtz Rt
•Opx Melt Fsp Ilm Grt Cpx Qtz Rt
•Opx Bt Melt Fsp Ilm Grt Cpx Qtz Rt
•Opx Bt oAmph Fsp Ilm Grt Cpx Qtz Rt
Al(Opx) = 0.07
•Opx cAmph Fsp Ilm Grt Cpx Qtz Rt
Al(Opx) = 0.10
XMg(Cpx) = 0.6
XAn(Fsp) = 0.55
XMg(Opx) = 0.65
•Opx Bt Melt Fsp Ilm Grt Cpx Qtz
•Opx Melt Fsp Ilm Grt Cpx Qtz
•Opx Bt cAmph Fsp Ilm Grt Cpx Qtz
•Opx Bt oAmph Fsp Ilm Grt Cpx Qtz
Ol in
Grt out
•Opx Bt oAmph cAmph Fsp Ilm Grt Qtz

Figure 22

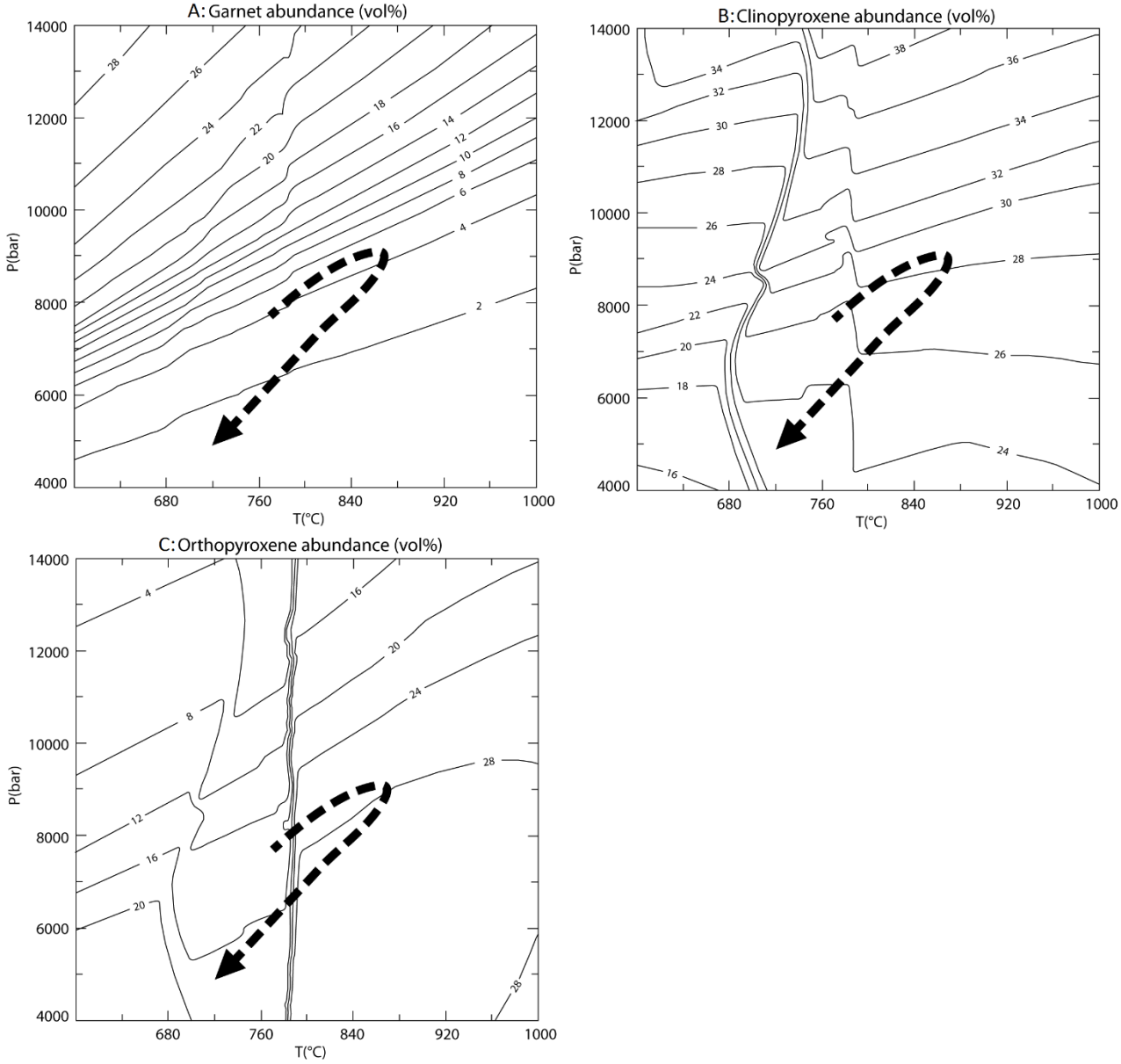
A: Garnet abundance (vol%)
B: Clinopyroxene abundance (vol%)
C: Orthopyroxene abundance (vol%)
P(bar)
T(°C)
14000
12000
10000
8000
6000
4000
680
760
840
920
1000

Figure 23

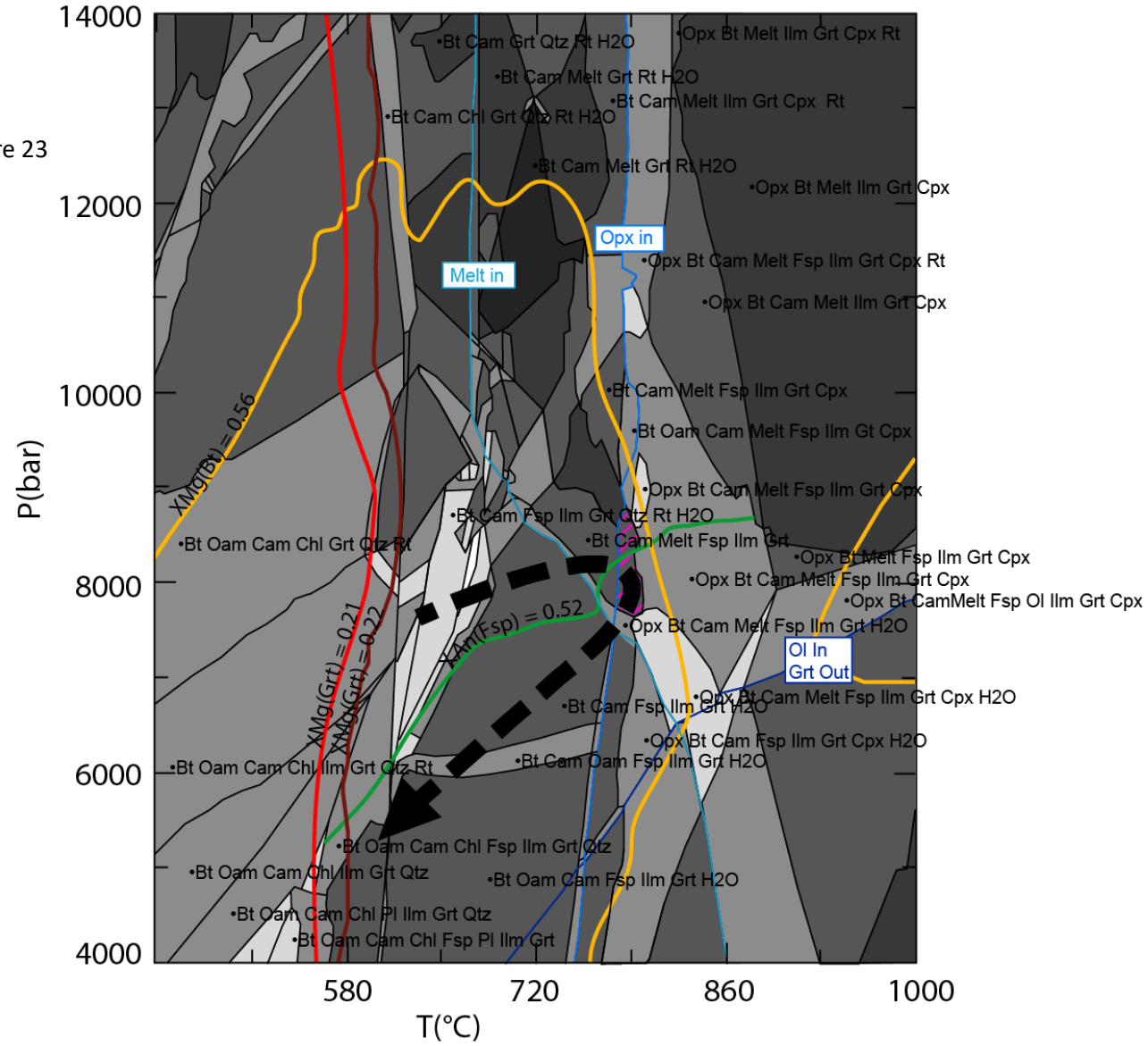

Figure 24

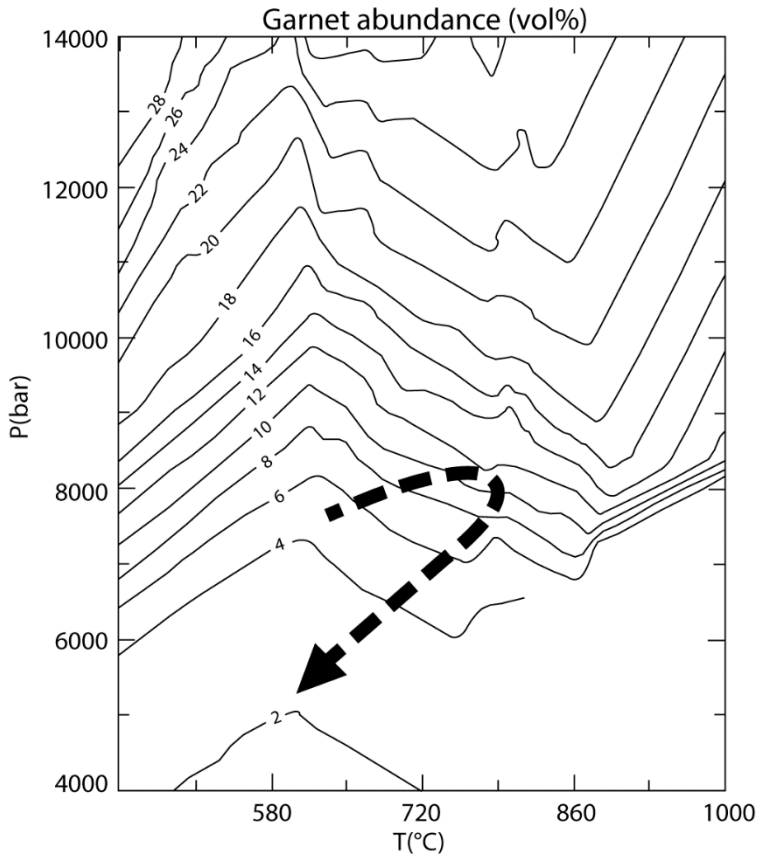

Figure 25

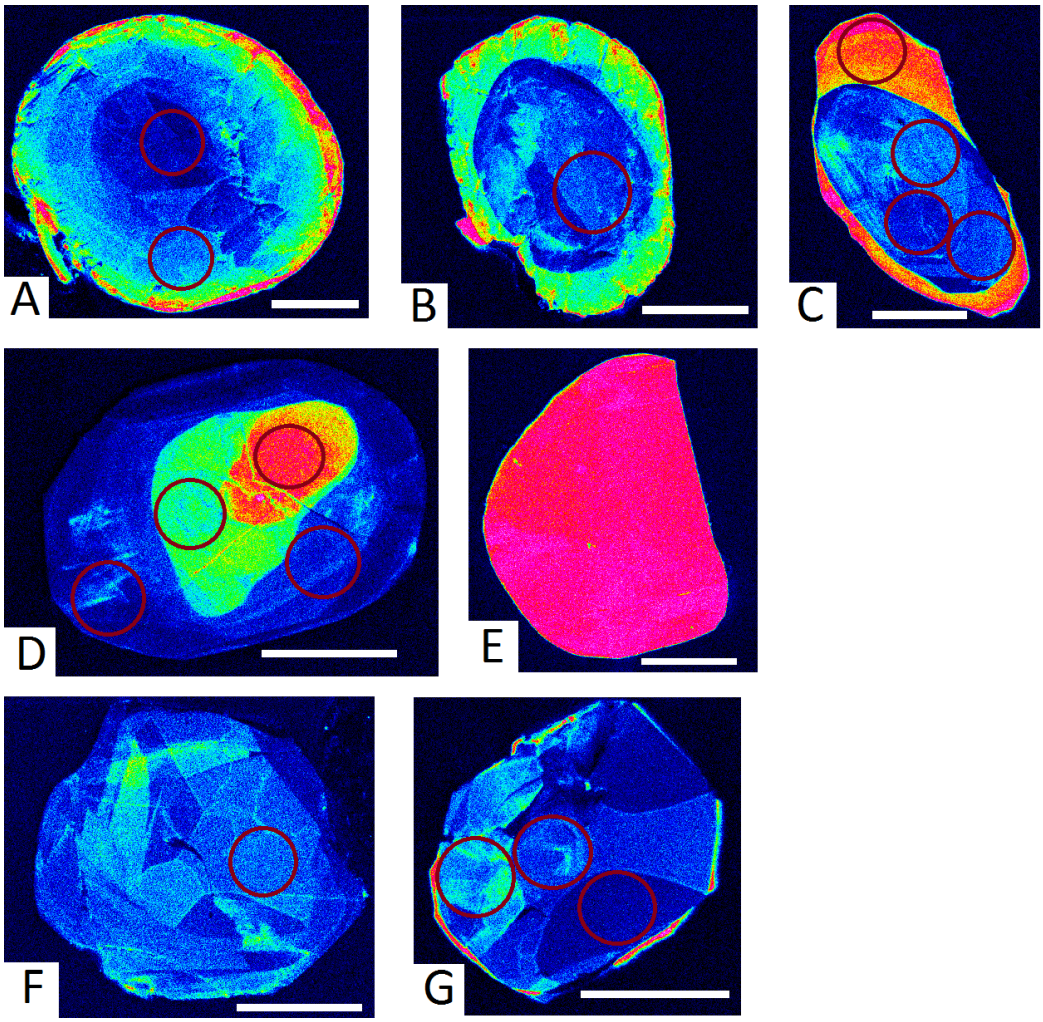

Figure 26

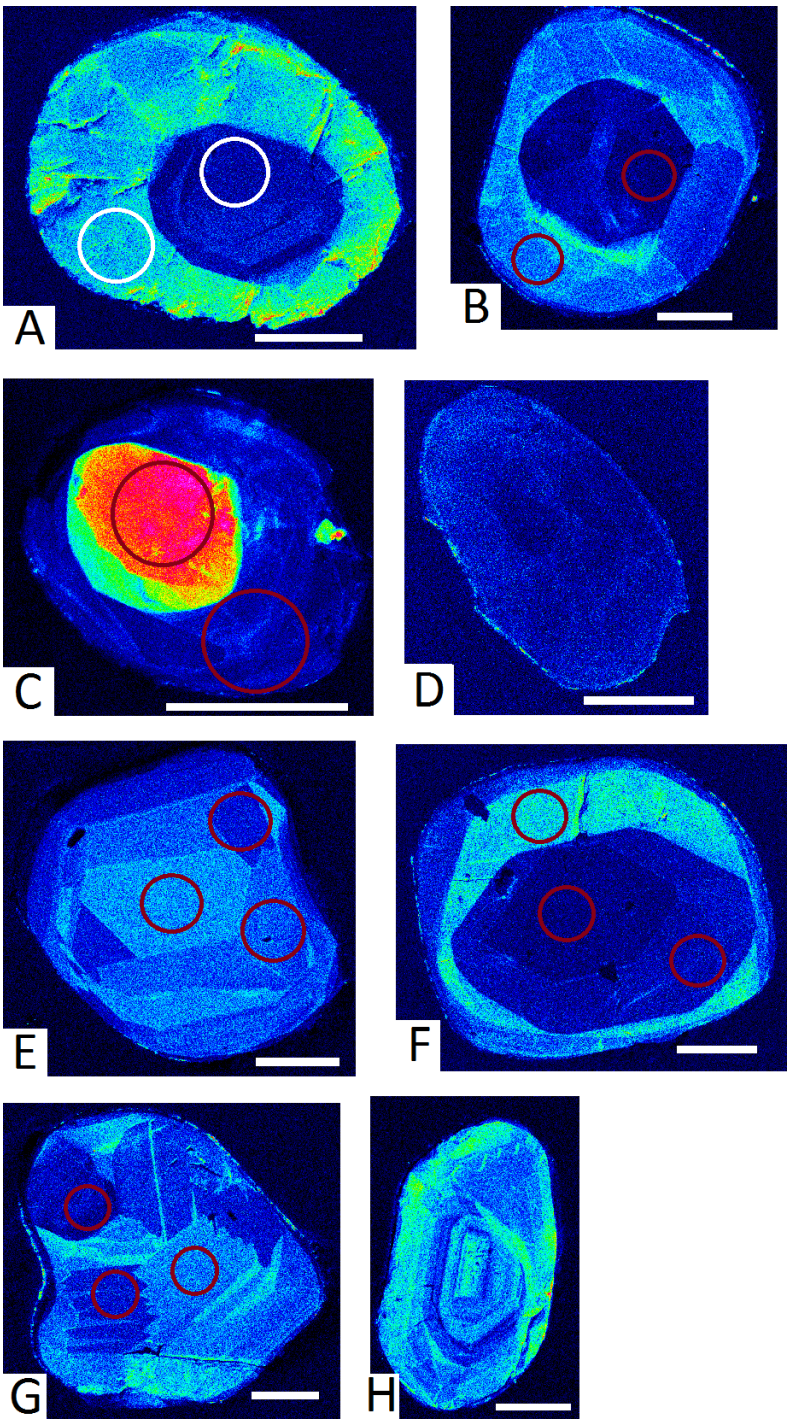

Figure 27

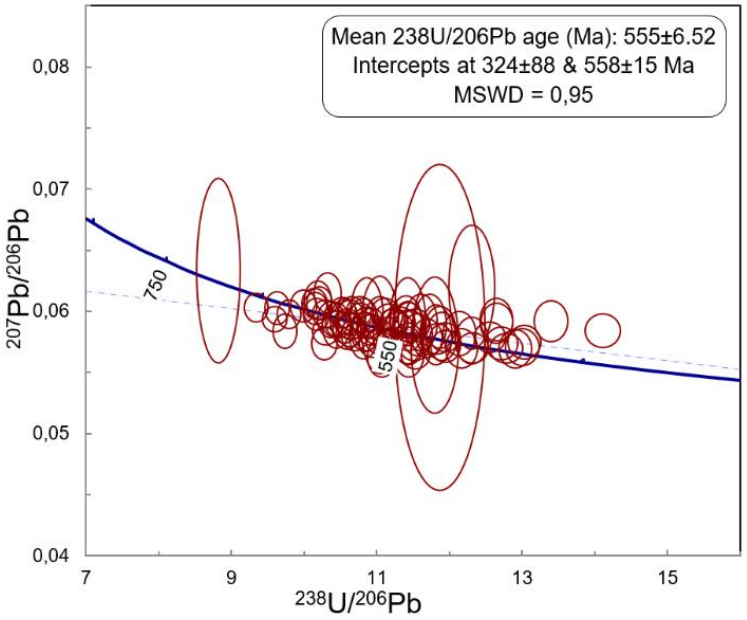

Figure 28

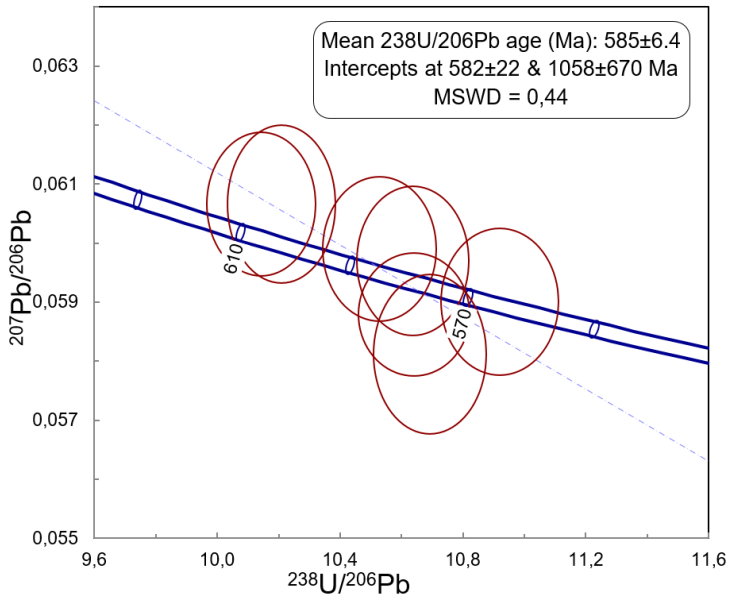

Figure 29

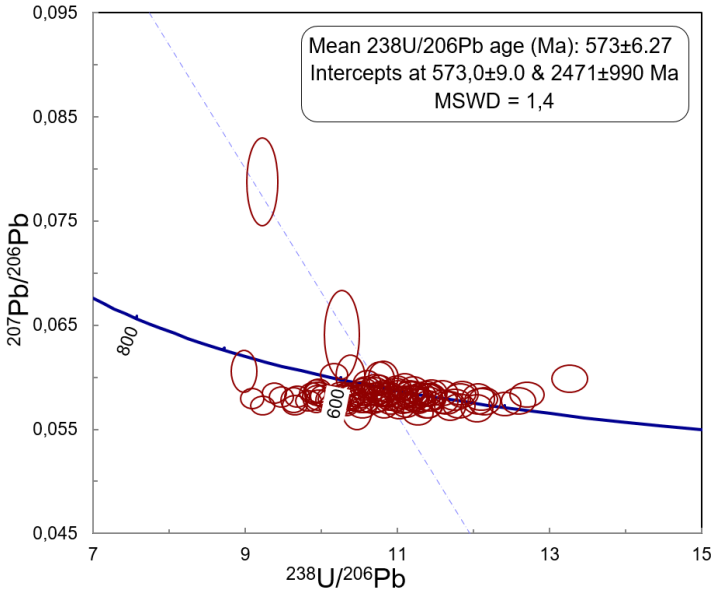

Figure 30

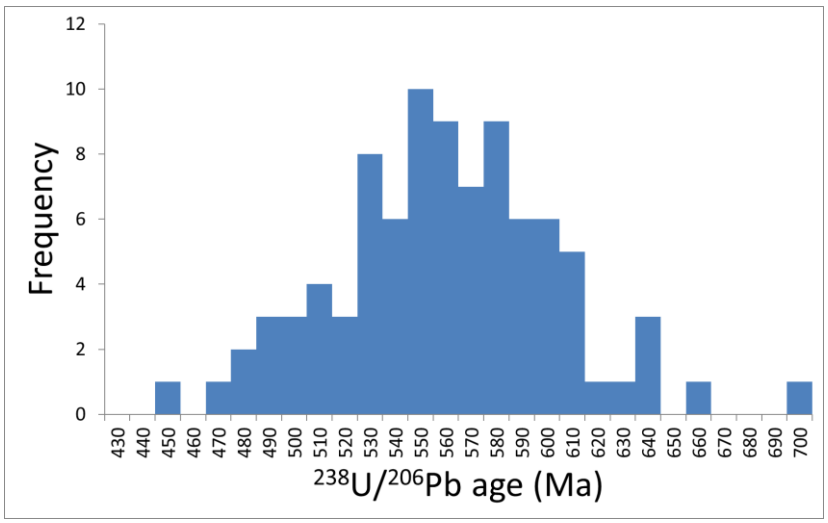

Figure 31

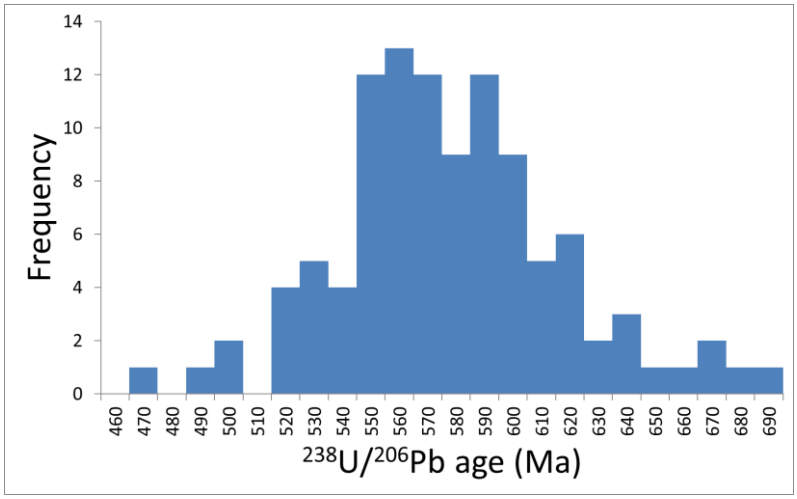

Table 5

	Mt	Ilm+Mt	Grt				Ap	Bt					Cpx	Opx	Pl - Mesosome			Sympl.			Leuc. - Qtz	Leuc.- Pl		Leuc. - Perthite		
Remark			Core1	Rim1	Core2	Rim2		Sympl.	Mes.	Mes.	Mes.	Mes.			Core	Rim	Ternary	Pl+Opx	Pl+Opx Edge	Pl		Core	Rim	Kfs+Pl	Pl	Kfs
Sc45	0.1	1.3	26	320	40	151	0.0	12	14	1.9	17	32	72	18	bdl	0.4	bdl	55	63	1.4	0.5	bdl	0.3	bdl	bdl	0.3
Ti47	4283	8635	2713	332	431	110	1.8	26138	28158	6304	3596	9958	1708	379	31	61	13	165	1697	145	88	30	41	132	46	76
V51	11	22	59	75	61	60	0.3	650	1037	198	146	406	502	158	0.3	1.1	bdl	33	146	2.0	1.1	0.3	0.3	0.3	bdl	0.2
Cr52	5.5	10	262	215	288	210	0.0	800	1248	269	276	472	613	296	0.5	1.4	bdl	266	537	7.3	2.0	0.3	0.5	bdl	bdl	0.3
Co59	2.5	2.7	52	48	61	40	0.0	104	135	29	86	60	56	100	0.3	1.2	0.2	34	54	2.7	0.3	0.8	0.4	0.2	bdl	0.4
Cu63	0.0	0.0	bdl	1.0	0.5	bdl	0.6	3.4	4.1	1.8	3.5	3.9	7.2	19	1.4	5.2	1.0	13	5.9	2.6	bdl	bdl	0.5	0.3	bdl	0.8
Zn66	5.3	1.4	59	34	70	37	0.1	199	253	45	351	101	119	436	5.0	8.8	4.6	105	195	13	bdl	5.1	5.1	7.3	2.5	2.9
Ga69	0.1	0.1	5.0	4.8	4.6	12	0.0	57	99	35	8.1	34	15	13	37	38	70	25	22	25	0.5	37	40	49	48	53
Rb85	0.1	0.0	bdl	<0.044	bdl	37	0.0	474	635	131	1.9	294	bdl	0.1	2.3	0.4	105	164	3.3	0.4	1.8	0.9	0.4	100	60	115
Sr88	0.1	0.0	bdl	<0.064	bdl	41	2.4	5.8	17	281	0.8	45	11	3.6	497	502	420	185	275	434	4.9	504	555	584	593	635
Y89	0.0	0.0	98	61	75	287	3.7	0.0	3.4	0.3	6.6	30	89	10	0.3	0.5	0.4	6.9	8.7	1.3	0.4	0.4	0.2	0.2	0.1	0.1
Zr90	bdl	0.6	5.6	26	20	12	bdl	bdl	2	bdl	0.3	10	33	0.9	bdl	bdl	bdl	bdl	bdl	bdl	6.8	bdl	bdl	bdl	bdl	bdl
Nb93	2.5	7.9	1.6	0.0	0.1	0.1	0.0	14	14	3.3	3.2	3.0	0.1	0.0	bdl	bdl	bdl	0.1	0.6	bdl	0.0	bdl	bdl	bdl	bdl	bdl
Cs133	bdl	bdl	bdl	bdl	bdl	0.1	bdl	6.4	16	2.1	0.0	3.6	bdl	bdl	bdl	bdl	0.8	0.2	bdl	bdl	bdl	bdl	bdl	0.6	0.4	0.8
Ba137	bdl	0.0	bdl	bdl	bdl	145	0.0	1186	2729	359	3.5	722	0.5	0.4	83	45	1411	469	14	21	12	11	10	631	381	801
La139	0.0	0.0	bdl	0.1	bdl	3.2	6.5	bdl	1.0	12	0.2	5.8	16	0.6	18	21	15	26	16	21	26	22	24	19	26	17
Ce140	0.0	0.0	0.3	0.4	0.5	6.6	19.6	0.0	2.4	19	0.6	32	87	1.7	28	34	24	46	27	35	0.7	35	36	27	32	25
Pr141	0.0	0.0	0.2	0.1	0.3	0.7	2.8	bdl	0.4	1.6	0.1	6.7	18	0.2	2.4	2.9	2.1	4.4	2.5	3.2	0.1	3.0	3.1	2.2	2.6	2.0
Nd146	0.0	0.0	2.5	3.2	4.2	4.4	12.6	bdl	1.7	5.1	0.4	39	105	1.4	7.3	9.2	6.5	15	7.7	10	0.4	9.1	8.9	6.3	7.7	5.5
Sm147	bdl	0.0	2.6	4.2	3.0	4.1	2.6	bdl	0.5	0.6	0.2	13	37	0.7	0.7	1.0	0.7	2.2	1.1	1.2	0.1	0.8	0.7	0.6	0.6	0.5
Eu151	bdl	0.0	1.1	1.3	1.6	1.3	0.2	0.0	0.2	1.5	0.0	1.6	3.4	0.1	2.6	2.5	2.6	1.3	1.6	2.9	bdl	1.7	1.9	2.2	2.2	2.5
Eu153	bdl	0.0	1.1	1.3	1.6	1.3	0.2	0.1	0.2	1.5	0.0	1.6	3.4	0.1	2.5	2.5	2.6	1.3	1.6	2.9	0.0	1.8	1.9	2.3	2.1	2.4
Gd157	bdl	0.0	5.9	5.6	5.9	9.5	2.1	bdl	0.5	0.2	0.5	12	34	1.1	0.3	0.4	0.3	1.7	1.0	0.7	bdl	0.3	0.3	0.2	0.2	0.1
Tb159	0.0	0.0	1.5	1.2	1.5	2.6	0.2	bdl	0.1	0.0	0.1	1.6	4.8	0.2	0.0	0.0	0.0	0.2	0.2	0.1	0.0	0.0	0.0	0.0	0.0	0.0
Dy163	bdl	0.0	14	9.7	12	28	1.0	bdl	0.7	0.1	1.1	8.7	25	1.9	0.1	0.1	0.1	1.4	1.4	0.4	0.1	0.1	0.1	0.0	0.0	0.0
Ho165	bdl	0.0	3.6	2.2	2.6	8.0	0.1	bdl	0.1	0.0	0.3	1.3	4.0	0.4	0.0	0.0	0.0	0.3	0.3	0.1	0.0	0.0	0.0	0.0	0.0	0.0
Er166	bdl	0.0	12	6.8	7.3	31	0.3	bdl	0.4	0.0	0.9	2.8	8.5	1.2	0.0	0.0	0.0	0.7	1.2	0.1	bdl	0.0	bdl	0.0	bdl	bdl
Yb172	bdl	0.0	15	6.8	8.7	44	0.1	0.0	0.4	bdl	1.0	1.5	4.4	1.2	bdl	0.0	bdl	0.9	1.5	0.1	bdl	bdl	bdl	bdl	0.0	bdl
Lu175	bdl	0.0	2.4	1.0	1.1	6.6	0.0	0.0	0.1	bdl	0.1	0.2	0.5	0.2	bdl	bdl	bdl	0.2	0.2	0.0	bdl	bdl	bdl	bdl	bdl	bdl
Hf178	0.0	0.1	0.2	0.5	0.2	0.2	bdl	0.1	0.3	0.0	0.1	0.8	2.6	0.1	bdl	bdl	bdl	0.0	0.0	bdl	0.2	bdl	bdl	bdl	bdl	bdl
Ta181	0.2	0.5	0.1	bdl	bdl	bdl	bdl	0.7	0.7	0.2	0.2	0.1	0.0	bdl	bdl	bdl	bdl	0.0	0.1	bdl	bdl	bdl	bdl	bdl	bdl	bdl
Pb208	0.0	0.0	0.0	0.0	bdl	1.5	0.0	2.4	2.7	7.8	0.0	4.7	0.7	0.1	12	11	19	3.3	7.5	12	0.6	11	10	22	18	24
Th232	0.0	0.0	0.2	0.1	0.0	0.1	0.1	0.0	0.1	0.1	0.4	1.0	0.2	0.2	0.0	0.2	0.1	5.6	0.2	0.0	0.0	0.1	0.0	0.0	0.0	0.0
U238	0.0	0.0	0.0	0.3	0.2	0.2	0.2	0.0	0.0	0.0	0.1	0.2	0.5	0.1	0.0	0.0	0.0	0.4	0.1	0.0	0.0	0.2	0.0	0.0	0.0	0.0

Table 6

	Rt	Mt		Grt				Amph	Opx	Cpx	Pl - Mesosome				Sympl. - Pl+Opx						Sympl. - Pl			Sympl. - Opx	Corona (Opx)		Leuc.	
Remark		Sympl.	Mes.	Core1	Rim1	Core2	Rim2				Core1	Rim1	Core2	Rim2	Center	Edge1	+Mt	Center2	Garnet2	Edge2	Garnet1	Edge1	Center2				Pl	Qtz
Sc45	bdl	0.4	2.0	72	155	330	225	58	24	72	bdl	1.0	1.2	bdl	33	24	7.3	19	80	91	22	3.2	12	67	103	76	0.4	0.9
Ti47	bdl	31	8006	917	518	227	110	17118	1303	29225	489	73	338	67	1360	87	196	286	167	210	bdl	28	224	339	584	372	122	217
V51	bdl	85	105	121	124	106	51	786	215	1217	2.2	6.1	7.9	0.3	69	19	206	78	30	32	15	3.7	37	102	99	69	2.0	0.1
Cr52	bdl	136	126	762	649	189	484	2459	933	3018	4.3	17	29	1.0	940	372	813	466	647	283	262	50	233	942	625	441	1.7	1.4
Co59	bdl	5.6	5.4	57	52	41	28	53	103	83	bdl	0.7	0.7	bdl	32	23	17	44	35	65	7.8	3.6	30	110	26	93	3.2	0.2
Cu63	bdl	12	8.8	bdl	bdl	bdl	4.5	6.6	9.2	1.4	bdl	13	bdl	bdl	16	5.7	23	24	30	30	22	7.4	12	14	906	23	5.2	bdl
Zn66	bdl	2.9	26	32	10	11	9.2	63	227	92	2.3	4.1	3.4	2.3	39	32	17	89	41	78	bdl	5.4	56	125	88	132	1.6	bdl
Ga69	bdl	0.8	0.1	7.4	6.3	4.9	4.2	19	9.2	25	23	25	22	23	8.3	7.5	6.9	17	7.0	5.0	13	8.5	19	3.6	8.0	4.2	17	bdl
Rb85	bdl	0.1	0.0	bdl	bdl	bdl	0.2	2.2	bdl	3.4	0.1	0.4	0.2	0.2	bdl	0.2	0.7	0.2	0.2	0.3	bdl	0.2	0.2	0.1	13	0.2	0.1	bdl
Sr88	bdl	0.2	0.3	bdl	bdl	bdl	65	98	1.0	71	327	342	331	334	125	166	133	184	148	65	215	196	246	0.5	25	3.0	294	bdl
Y89	bdl	0.1	0.2	101	250	132	1123	63	3.8	85	0.3	0.5	1.5	0.2	10	7.7	2.5	1.6	36	21	150	2.8	1.1	18	2.9	23	1.0	bdl
Zr90	bdl	bdl	0.9	32	17	17	4.2	56	3.8	113	0.8	bdl	bdl	bdl	1.5	0.9	bdl	bdl	1.9	2.8	bdl	bdl	bdl	6.1	9.1	3.8	bdl	bdl
Nb93	4475	bdl	3.8	0.0	0.0	bdl	0.0	4.3	1.5	2.5	2.4	0.5	0.3	bdl	12	bdl	bdl	bdl	bdl	bdl	bdl	bdl	bdl	bdl	0.1	bdl	bdl	bdl
Cs133	bdl	0.0	bdl	bdl	bdl	bdl	bdl	bdl	bdl	bdl	bdl	bdl	bdl	bdl	bdl	bdl	bdl	bdl	bdl	bdl	bdl	bdl	bdl	bdl	0.9	bdl	bdl	bdl
Ba137	bdl	0.4	0.4	bdl	bdl	bdl	10	79	2.7	137	48	47	52	51	19	37	39	21	19	14	38	48	25	1.1	43	4.2	52	0.5
La139	0.0	0.2	0.2	bdl	bdl	bdl	1.3	13.3	0.5	20.0	6.0	7.0	5.9	6.0	4.6	4.0	3.2	4.6	3.1	1.0	8.3	4.8	6.0	0.0	0.9	0.2	4.7	109
Ce140	0.0	0.0	0.1	0.2	0.0	0.0	1.9	51	0.1	83	7.8	8.5	8.3	8.0	6.8	5.8	3.9	5.7	4.5	1.4	12	6.9	7.6	0.0	0.2	0.1	6.2	0.0
Pr141	0.0	0.1	0.0	0.5	0.2	0.0	0.2	8.0	0.2	14	0.9	1.1	0.9	0.8	1.7	1.3	0.9	0.9	0.5	0.1	3.2	1.6	1.0	0.0	0.3	0.0	0.5	bdl
Nd146	0.0	0.2	0.1	2.0	1.4	0.6	0.8	38	0.6	64	1.9	2.3	2.2	1.7	2.8	2.3	1.7	1.6	1.6	0.5	5.3	2.7	1.8	0.1	0.5	0.1	1.5	bdl
Sm147	0.0	0.1	0.0	3.4	8.7	4.6	1.6	10	0.2	18	0.2	0.3	0.4	0.2	1.6	1.1	0.7	0.2	0.6	0.2	3.6	1.3	0.2	0.3	0.2	0.1	0.4	0.0
Eu151	0.0	0.0	0.0	2.2	2.9	0.8	0.4	2.1	0.1	3.1	0.8	0.8	0.8	0.7	1.5	1.6	1.2	0.6	0.5	0.2	3.1	1.9	0.7	0.0	0.2	0.0	0.6	bdl
Eu153	0.0	0.0	0.0	2.3	2.8	0.8	0.3	2.0	0.1	3.2	0.8	0.8	0.7	0.7	1.6	1.6	1.3	0.6	0.5	0.2	3.0	1.8	0.8	0.0	0.2	0.0	0.6	bdl
Gd157	0.0	0.0	0.0	7.2	18	26	22	11	0.3	19	0.1	0.2	0.3	0.1	1.8	1.3	0.8	0.1	1.9	1.0	6.5	1.2	0.1	1.3	0.3	1.0	0.4	bdl
Tb159	0.0	0.0	0.0	4.2	11	6.8	12	1.8	0.1	3.0	0.0	0.0	0.1	0.0	0.5	0.4	0.2	0.0	0.6	0.4	3.8	0.3	0.0	0.6	0.1	0.4	0.1	bdl
Dy163	0.0	0.0	0.0	15	32	31	131	12	0.5	18	0.1	0.1	0.3	0.0	1.8	1.4	0.6	0.2	5.3	3.3	20	0.7	0.2	3.3	0.4	3.7	0.3	0.0
Ho165	0.0	0.0	0.0	5.4	10	4.7	44	2.3	0.2	3.2	0.0	0.0	0.1	0.0	0.5	0.4	0.1	0.1	1.5	0.9	8.5	0.1	0.0	1.0	0.1	1.0	0.0	bdl
Er166	0.0	0.0	0.0	15	26	9.1	152	6.1	0.6	7.8	bdl	0.1	0.2	0.0	1.3	1.0	0.3	0.2	5.1	3.1	27	0.3	0.1	2.8	0.3	3.1	0.1	bdl
Yb172	0.0	0.0	0.0	22	38	8.7	191	5.2	1.1	5.7	bdl	0.1	0.1	bdl	1.6	1.3	0.4	0.4	6.4	3.5	35	0.2	0.3	3.2	0.5	3.5	0.0	bdl
Lu175	0.0	0.0	0.0	5.4	8.2	1.3	33	0.7	0.2	0.7	0.0	0.0	0.0	bdl	0.3	0.3	0.1	0.1	1.1	0.6	8.8	0.0	0.1	0.7	0.1	0.6	0.0	0.0
Hf178	165	0.1	0.1	0.0	0.0	0.2	0.1	2.2	0.3	4.4	0.1	0.0	0.1	bdl	1.5	0.4	0.1	0.1	0.1	0.1	0.8	bdl	0.1	0.6	1.0	0.1	bdl	bdl
Ta181	156	0.0	0.2	0.0	0.0	bdl	bdl	0.1	0.1	0.0	0.2	0.0	bdl	bdl	0.7	bdl	bdl	bdl	bdl	bdl	bdl	bdl	bdl	bdl	bdl	bdl	bdl	bdl
Pb208	0.0	0.1	0.1	0.0	bdl	bdl	1.0	1.5	0.0	1.6	4.2	4.3	4.2	4.2	3.5	4.1	3.2	2.8	2.0	0.9	6.1	5.3	3.3	0.0	0.3	0.0	3.4	bdl
Th232	bdl	0.0	0.0	0.0	0.0	0.0	0.0	0.1	0.0	0.3	bdl	0.0	0.0	bdl	0.5	0.0	0.1	0.1	0.0	0.0	2.3	0.2	0.0	0.0	0.1	0.0	0.0	bdl
U238	10.7	0.0	0.0	0.0	0.0	0.0	0.0	0.0	0.0	0.0	0.0	0.0	bdl	bdl	bdl	bdl	0.0	0.0	0.0	0.0	bdl	bdl	bdl	bdl	0.2	bdl	bdl	bdl

Figure 32

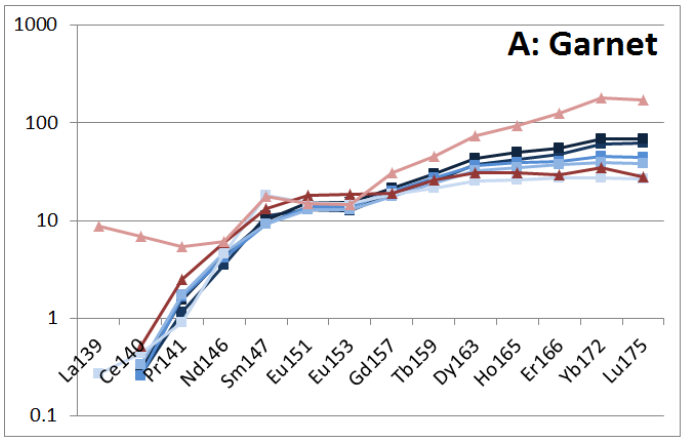
A: Garnet
1000
100
10
1
0.1
La139
Ce140
Pr141
Nd146
Sm147
Eu151
Eu153
Gd157
Tb159
Dy163
Ho165
Er166
Yb172
Lu175

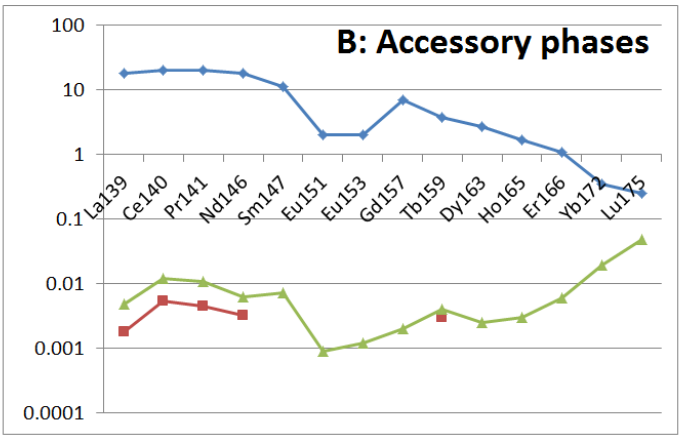
B: Accessory phases
100
10
1
0.1
0.01
0.001
0.0001
La139
Ce140
Pr141
Nd146
Sm147
Eu151
Eu153
Gd157
Tb159
Dy163
Ho165
Er166
Yb172
Lu175

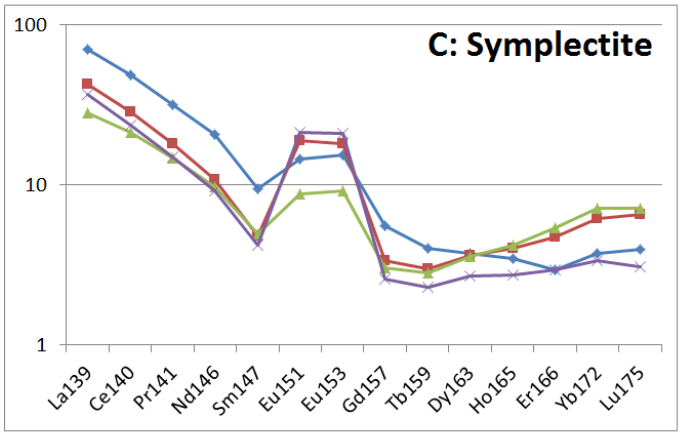
C: Symplectite
100
10
1
La139
Ce140
Pr141
Nd146
Sm147
Eu151
Eu153
Gd157
Tb159
Dy163
Ho165
Er166
Yb172
Lu175

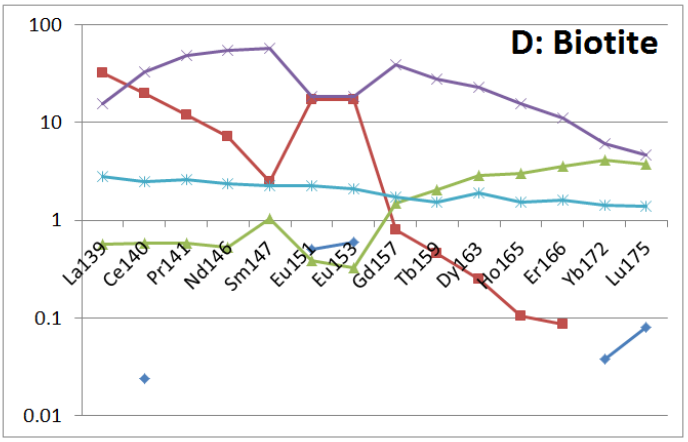
D: Biotite
100
10
1
0.1
0.01
La139
Ce140
Pr141
Nd146
Sm147
Eu151
Eu153
Gd157
Tb159
Dy163
Ho165
Er166
Yb172
Lu175

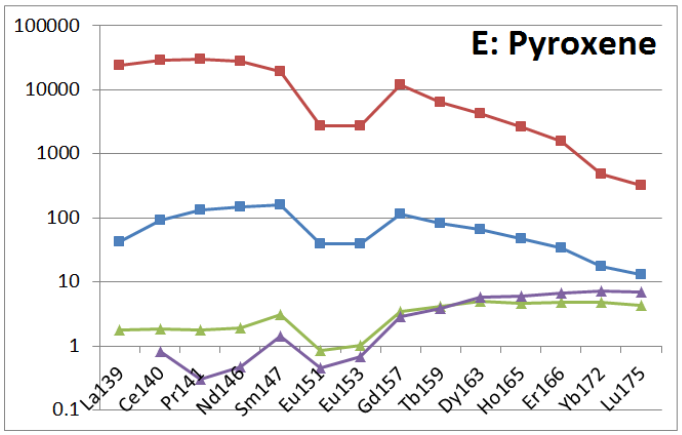
E: Pyroxene
100000
10000
1000
100
10
1
0.1
La139
Ce140
Pr141
Nd146
Sm147
Eu151
Eu153
Gd157
Tb159
Dy163
Ho165
Er166
Yb172
Lu175

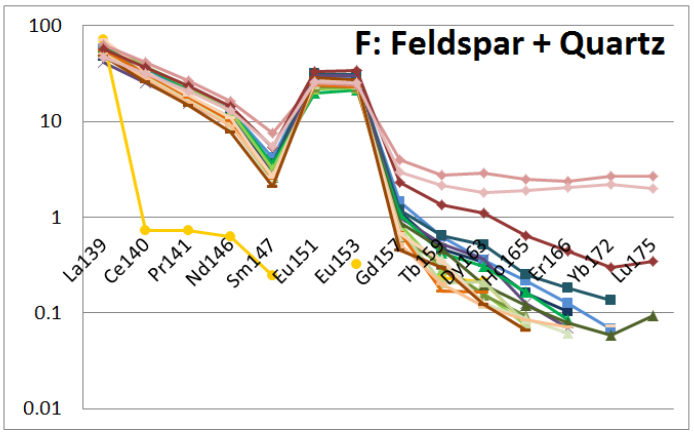
F: Feldspar + Quartz
100
10
1
0.1
0.01
La139
Ce140
Pr141
Nd146
Sm147
Eu151
Eu153
Gd157
Tb159
Dy163
Ho165
Er166
Yb172
Lu175

Figure 33

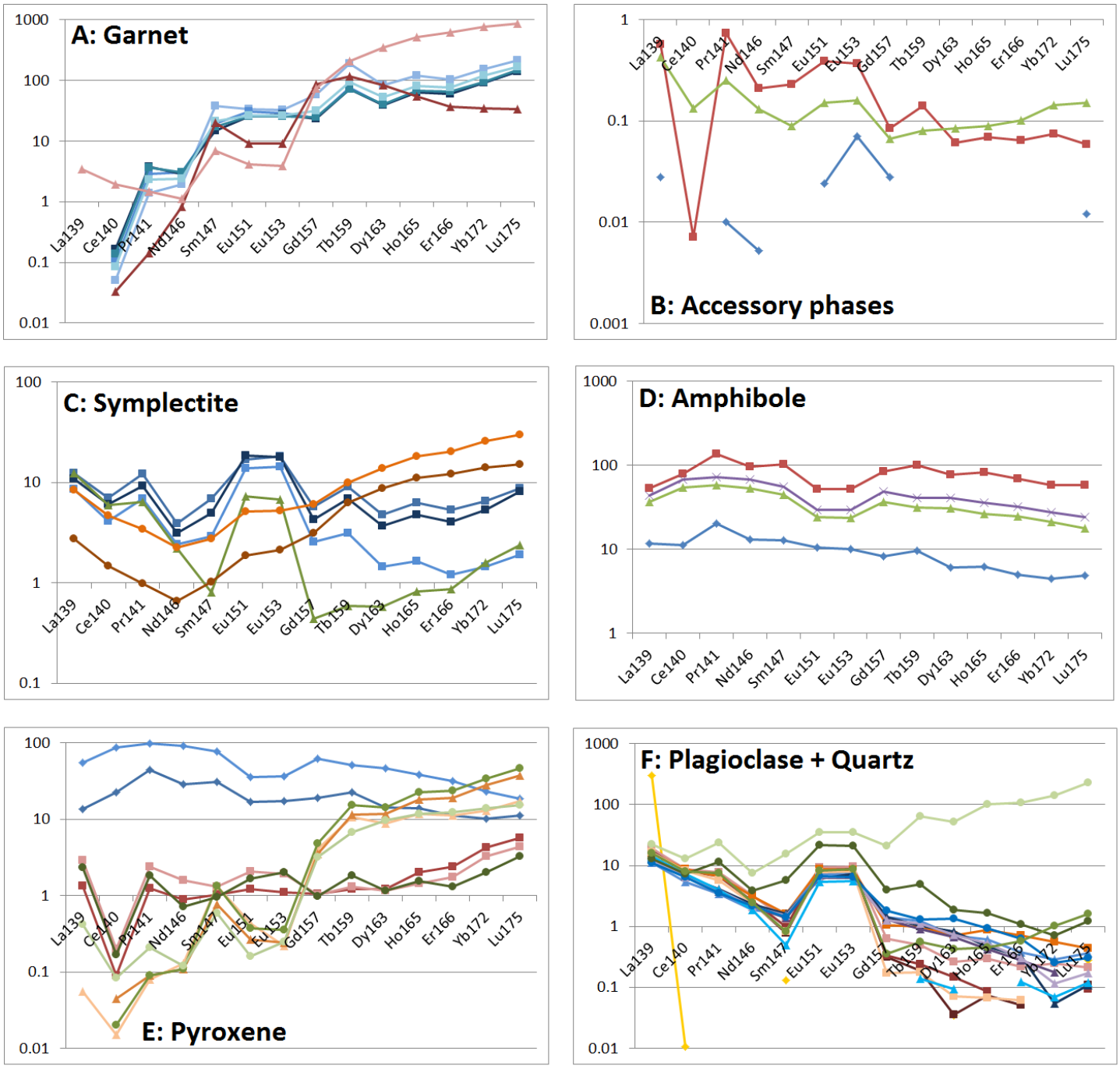

Table 7

	Sample	Grt-Cpx[1]	Grt-Opx[2]	Grt-Bt[3]	Zrn-Rt[4]	Ti-Bt[5]	HD[6]	DI[6]	FS[6]	Perple_X	Perple_X
Grt core	787	790 °C	993 °C	978 °C	725 °C	800 °C	9.2 kbar	8 kbar	11 kbar	925 °C	9.8 kbar
	968	810 °C	923 °C	NA	NA	NA	11 kbar	9.5 kbar	11 kbar	875 °C	9.2 kbar
	280	NA	746 °C	735 °C	NA	785 °C	NA	NA	10 kbar	810 °C	8 kbar
Grt rim/Bt needle	787	701 °C	801 °C	831 °C		725 °C				840 °C	8.3 kbar
	968	663 °C	695 °C	NA		NA				735 °C	6 kbar
	280	NA	714 °C	711 °C		749 °C				?	?

Appendix 1

	CPS										Age (Ma)				
Analysis #	Th/U	Pb206	Pb207	Pb208	U235	U238	$^{238}U/^{206}Pb$	1σ	$^{207}Pb/^{206}Pb$	1σ	$^{238}U/^{206}Pb$	1σ	$^{207}Pb/^{206}Pb$	1σ	Discordance
B1-A-4	0.26	34179	2045	3070	3110	430589	11.4	0.13	0.059	0.0011	541	6	572	39	5.5
B1-B-5	0.23	53787	3060	4441	4631	656438	11.1	0.13	0.056	0.0011	558	6	461	41	-21.0
B1-C-6	0.30	92182	5601	9385	7789	1094878	10.8	0.12	0.060	0.0008	572	6	605	27	5.5
B2-A-7	0.25	50881	2954	4539	4170	576531	10.3	0.12	0.057	0.0009	599	7	506	33	-18.3
B2-B-8	0.25	83507	5051	7164	6440	901712	9.8	0.11	0.060	0.0008	627	7	595	29	-5.3
B3-A-11	0.23	38497	2275	3061	2976	413240	9.7	0.11	0.058	0.0009	630	7	545	34	-15.6
B3-B-12	0.26	36736	2167	3250	3218	439063	10.8	0.13	0.058	0.0011	569	6	541	40	-5.2
B3-C-13	0.23	83779	5044	6566	6992	995477	10.8	0.12	0.060	0.0008	572	6	585	27	2.3
B4-14	0.30	19180	1125	1987	1706	228740	10.8	0.13	0.058	0.0013	570	7	529	47	-7.7
B5-A-15	0.24	76423	4522	6266	6569	919098	10.9	0.12	0.058	0.0008	566	6	548	31	-3.2
B5-B-16	0.24	43516	2516	3502	4094	572975	11.9	0.14	0.057	0.0009	518	6	496	33	-4.5
B7-46	0.04	76933	4647	1053	6349	902365	10.6	0.12	0.060	0.0008	579	6	593	29	2.4
S3-A-78	0.20	64007	3758	4552	6104	867857	11.9	0.14	0.058	0.0008	519	6	525	30	1.1
S3-B-79	0.22	126719	7631	8892	10350	1381588	9.6	0.11	0.059	0.0007	639	7	580	25	-10.2
S5-A-80	0.17	16417	965	1021	1596	221849	11.9	0.15	0.058	0.0013	521	6	527	50	1.3
S5-B-79	0.27	59119	3537	5231	5284	753942	11.2	0.13	0.059	0.0008	550	6	566	29	2.8
S5-C-80	0.24	28230	1650	2330	2880	394742	12.3	0.15	0.058	0.0013	504	6	516	48	2.3
S8-A-82	0.21	64015	3828	4582	5941	832284	11.4	0.13	0.059	0.0008	540	6	565	28	4.4
S8-B-83	0.24	88047	5268	7198	7353	1048216	10.5	0.12	0.059	0.0007	588	6	566	27	-3.8
S9-84	0.13	70320	4073	3226	6460	919777	11.5	0.13	0.057	0.0008	537	6	494	30	-8.6
S11-A-85	0.02	77023	4681	424	6493	921323	10.5	0.12	0.060	0.0008	585	6	600	29	2.5
S11-B-86	0.01	70973	4368	179	5754	817968	10.1	0.12	0.061	0.0008	606	7	627	28	3.4
S11-C-87	0.02	58552	3506	358	5172	726528	10.9	0.13	0.059	0.0008	565	6	568	30	0.5
S11-D-88	0.78	3970	230	998	387	53231	11.8	0.21	0.057	0.0037	525	9	501	136	-4.7
S12-A-91	0.32	5404	347	625	399	54171	8.8	0.20	0.063	0.0050	692	15	719	159	3.8
S12-B-92	0.29	52961	3174	5367	4660	653170	10.9	0.13	0.059	0.0008	568	6	570	30	0.2
S13-A-93	0.20	23554	1397	1711	2005	283336	10.6	0.13	0.058	0.0010	582	7	548	38	-6.2
S13-B-94	0.22	120234	7217	9226	10337	1446364	10.6	0.12	0.059	0.0007	582	6	573	26	-1.5
S16-97	0.26	60131	3688	5305	4848	682490	10.0	0.12	0.060	0.0009	615	7	620	31	0.8
S17-144	0.23	42025	2446	3339	4366	606900	12.7	0.15	0.057	0.0009	488	6	505	34	3.3
S18-A-98	0.22	79720	4767	5808	7357	1037038	11.4	0.13	0.059	0.0007	540	6	565	27	4.4
S18-B-99	0.27	96088	5805	8731	8672	1218796	11.2	0.13	0.060	0.0007	553	6	587	26	5.8
S19-100	1.49	4796	301	2452	509	67086	12.3	0.21	0.062	0.0033	504	8	673	111	25.2
S20-101	0.26	22014	1294	1877	1981	278914	11.1	0.13	0.058	0.0011	554	6	527	40	-5.1
S21-102	1.05	9162	549	3204	836	120790	11.6	0.15	0.059	0.0015	533	7	572	55	6.7
S23-A-103	0.24	15864	947	1339	1372	188207	10.4	0.13	0.059	0.0012	590	7	562	45	-4.9
S23-B-104	0.28	27527	1634	2607	2426	332370	10.6	0.13	0.059	0.0009	580	7	549	34	-5.7
S24-105	0.25	64022	3855	5574	5476	754269	10.4	0.12	0.059	0.0010	594	7	580	35	-2.4
S25-106	0.21	62653	3628	4360	6410	925527	13.0	0.15	0.057	0.0010	478	5	494	38	3.3
S26-107	0.59	1896	112	400	191	25564	11.9	0.41	0.059	0.0088	522	17	557	297	6.3
S27-A-108	0.24	114272	6813	9455	9799	1383239	10.7	0.12	0.059	0.0007	578	6	558	26	-3.6
S27-B-109	0.20	63057	3784	4404	5745	811334	11.3	0.13	0.059	0.0008	546	6	572	29	4.7
S29-A-110	0.39	23145	1430	3041	1942	267869	10.2	0.12	0.061	0.0010	604	7	636	36	5.1
S29-B-111	0.40	24168	1508	3202	2051	283449	10.3	0.12	0.062	0.0011	596	7	657	37	9.3
S29-C-112	0.31	7443	445	777	709	99213	11.7	0.15	0.059	0.0016	527	6	565	59	6.6
S30-A-113	0.25	45903	2807	3923	3644	502229	9.6	0.11	0.060	0.0009	637	7	614	31	-3.8
S30-B-114	0.25	75530	4584	6304	6218	883191	10.3	0.12	0.060	0.0008	598	7	597	27	-0.1
S31-A-115	0.84	7683	465	2066	705	94828	10.9	0.15	0.060	0.0020	568	7	595	71	4.5
S31-B-116	0.36	19719	1164	2439	1950	271926	12.1	0.15	0.058	0.0012	510	6	537	45	4.9
S32-117	0.61	4677	281	1038	425	60718	11.4	0.16	0.059	0.0023	541	7	576	84	6.0
S34-118	0.24	35379	2046	2869	3531	495195	12.3	0.14	0.057	0.0008	503	6	491	33	-2.4
S35-A-81	0.28	41214	2499	3968	3416	476254	10.2	0.12	0.060	0.0009	605	7	595	31	-1.7
S35-B-119	0.26	60580	3707	5278	4569	642783	9.3	0.11	0.060	0.0008	656	7	615	28	-6.6
S37-A-120	0.33	6784	405	830	646	85117	11.0	0.17	0.059	0.0026	559	8	562	95	0.6
S37-B-121	0.22	39086	2293	2922	3614	519090	11.7	0.14	0.058	0.0010	529	6	523	39	-1.2
S38-A-122	0.29	20891	1245	2093	1976	271416	11.4	0.14	0.059	0.0013	541	6	559	47	3.3
S38-B-123	0.38	37941	2296	4956	3342	459488	10.7	0.13	0.060	0.0010	578	7	591	37	2.2
S39-124	0.20	113460	6718	8062	9338	1327752	10.3	0.12	0.058	0.0007	597	7	543	27	-10.0
S41-A-125	0.51	21637	1304	3796	1903	271477	11.0	0.13	0.059	0.0012	559	6	582	43	3.9
S41-B-126	0.37	13270	797	1684	1275	171887	11.4	0.14	0.059	0.0014	542	6	576	49	5.9
S42-A-127	0.19	77804	4528	4971	6826	968433	11.0	0.13	0.057	0.0007	563	6	505	28	-11.5
S42-B-128	0.21	123719	7228	8958	10995	1551750	11.0	0.13	0.058	0.0007	559	6	514	27	-8.9
S42-C-129	0.19	117059	6916	8040	10431	1467044	11.0	0.13	0.058	0.0007	560	6	538	27	-4.0
S44-A-131	0.25	10757	618	891	1007	139787	11.4	0.14	0.057	0.0014	540	6	478	52	-13.2
S44-B-132	0.19	17477	1050	1073	1516	209616	10.6	0.13	0.059	0.0012	584	7	575	43	-1.5
S46-133	0.26	18154	1049	1570	1725	250934	12.2	0.15	0.057	0.0011	509	6	491	41	-3.8
S47-A-134	0.20	58118	3360	4033	6057	843790	12.8	0.15	0.057	0.0008	486	5	490	31	0.9
S47-B-135	0.25	46692	2735	4002	4388	627544	11.8	0.14	0.058	0.0008	523	6	520	31	-0.7
S47-C-136	0.32	27611	1626	3093	2548	362602	11.6	0.14	0.058	0.0011	535	6	532	42	-0.6
H3-A-19	0.21	38614	2310	2887	3925	538454	12.6	0.15	0.059	0.0010	491	5	572	37	14.2
H3-B-20	0.27	63473	3843	5844	5486	777543	11.1	0.12	0.060	0.0008	556	6	598	29	7.0
H5-A-21	0.21	54466	3250	3948	4847	692327	11.5	0.13	0.059	0.0008	536	6	566	30	5.2
H5-B-22	0.26	10199	599	890	958	132856	11.8	0.15	0.058	0.0016	524	6	533	60	1.7
H5-C-23	0.25	18977	1101	1673	1745	239350	11.4	0.13	0.057	0.0011	540	6	504	43	-7.2
H6-A-26	0.21	22791	1353	1697	2078	298194	11.9	0.14	0.059	0.0011	522	6	555	41	6.1
H6-B-27	0.23	22468	1346	1690	2243	313219	12.6	0.15	0.059	0.0012	491	6	575	44	14.6
H12-A-28	0.04	56332	3331	775	6261	876502	14.1	0.16	0.058	0.0009	441	5	547	34	19.3
H12-B-29	0.02	45087	2651	392	3794	531614	10.7	0.12	0.058	0.0009	576	6	534	34	-8.0
H15-A-30	0.21	55483	3250	3921	5506	767837	12.6	0.14	0.058	0.0008	494	5	526	31	6.0
H15-B-31	0.14	127174	7593	6256	10525	1461418	10.4	0.12	0.059	0.0007	591	6	567	26	-4.1
H17-A-34	0.27	64704	3842	5930	5823	805860	11.3	0.13	0.059	0.0008	547	6	556	30	1.5
H17-B-35	0.25	57292	3491	4861	4622	641616	10.2	0.11	0.060	0.0009	605	7	612	31	1.0
H21-A-36	0.19	62989	3773	4286	6587	930382	13.4	0.16	0.059	0.0011	464	5	574	41	19.2
H21-B-37	0.21	30118	1735	2222	3061	428380	12.9	0.15	0.057	0.0010	481	5	489	40	1.5
H27-A-38	0.24	40794	2457	3248	3508	486620	10.8	0.13	0.060	0.0010	570	6	587	36	2.9
H27-B-39	0.04	46637	2862	889	3744	524965	10.2	0.12	0.061	0.0009	602	7	627	31	3.9
H27-C-40	0.30	99785	5973	10461	8674	1236592	11.2	0.13	0.059	0.0008	550	6	573	27	4.1
H16-43	0.18	68739	3998	4351	6927	987412	13.0	0.15	0.057	0.0009	477	5	510	35	6.4
H20-44	0.07	143713	8550	3303	12315	1686117	10.6	0.12	0.059	0.0007	579	6	560	26	-3.5
H26-45	0.16	64770	3699	3409	5803	823490	11.5	0.13	0.056	0.0007	536	6	469	29	-14.3

Appendix 2

	CPS											Age (Ma)				
Analysis #	Th/U	Pb206	Pb207	Pb208	U235	U238	$^{238}U/^{206}Pb$	1σ	$^{207}Pb/^{206}Pb$	1σ		$^{238}U/^{206}Pb$	1σ	$^{207}Pb/^{206}Pb$	1σ	Discordance
P1-A-49	0.21	38017	2237	2724	3083	416333	9.9	0.12	0.0582	0.0010		618	7	536	39	-15.4
P1-B-50	0.19	52728	3118	3543	4700	648985	11.2	0.13	0.0584	0.0008		553	6	546	31	-1.2
P1-C-51	0.31	73108	4238	7860	6421	896249	11.1	0.12	0.0573	0.0007		555	6	502	28	-10.5
P2-A-52	0.15	130392	7699	6669	11628	1637515	11.4	0.13	0.0584	0.0007		543	6	543	26	0.1
P2-B-53	0.01	158810	9398	407	13615	1883665	10.8	0.12	0.0585	0.0007		573	6	548	25	-4.6
P3-A-55	0.14	137566	7950	6622	12635	1727112	11.4	0.13	0.0571	0.0007		543	6	495	26	-9.6
P3-B-56	0.23	223029	13011	15621	20479	2588172	10.5	0.12	0.0577	0.0007		585	6	516	24	-13.3
P6-A-57	0.25	166235	9785	13169	13741	1775348	9.7	0.11	0.0582	0.0007		633	7	536	25	-18.2
P6-B-58	0.21	166164	9719	11451	14163	1917363	10.5	0.12	0.0578	0.0007		588	6	522	25	-12.7
P6-C-59	0.22	175489	10525	12562	16241	2073393	10.7	0.12	0.0593	0.0007		575	6	577	24	0.3
P6-D-60	0.19	167983	9788	10714	15138	2059852	11.1	0.12	0.0576	0.0007		555	6	514	25	-8.1
P8-A-63	0.21	59815	3483	4166	4834	673682	10.2	0.12	0.0576	0.0008		602	7	513	32	-17.5
P8-B-64	0.22	135631	7998	10085	11197	1572497	10.5	0.12	0.0583	0.0007		586	6	540	26	-8.5
P9-A-65	0.22	205769	11960	14894	17104	2338953	10.3	0.11	0.0574	0.0006		597	6	508	24	-17.5
P9-B-66	0.28	262673	15545	22182	21895	2717401	9.4	0.10	0.0585	0.0006		653	7	548	24	-19.2
P13-A-69	0.16	72738	4253	4210	5512	772765	9.6	0.11	0.0578	0.0008		637	7	522	30	-22.0
P13-B-70	0.31	311284	18255	27349	26053	3118289	9.1	0.10	0.0580	0.0006		673	7	528	24	-27.5
P13-C-71	0.20	201810	11893	12613	16733	2214539	10.0	0.11	0.0582	0.0007		617	7	538	25	-14.7
P10-A-72	0.29	82397	4845	8415	6700	943998	10.4	0.12	0.0581	0.0007		592	6	534	28	-11.0
P10-B-73	0.20	57943	3361	3981	4913	691665	10.8	0.12	0.0573	0.0008		570	6	504	30	-13.0
P10-74	0.21	54428	3256	3741	4722	665883	11.1	0.13	0.0591	0.0008		556	6	572	30	2.7
P14-A-76	0.18	120115	7013	7601	10256	1422586	10.7	0.12	0.0577	0.0007		574	6	518	26	-10.7
P14-B-77	0.21	160825	9502	11585	14174	2006210	11.3	0.13	0.0584	0.0007		546	6	545	25	-0.3
P14-C-78	0.19	99157	5834	6571	8264	1149191	10.5	0.12	0.0582	0.0007		586	6	535	27	-9.6
P16-A-79	0.23	171411	10040	12997	14404	1914952	10.1	0.11	0.0579	0.0007		607	6	525	25	-15.6
P16-B-80	0.18	63485	3746	3915	5318	728027	10.4	0.12	0.0583	0.0008		592	6	541	29	-9.4
P19-A-81	0.18	128534	7594	8232	10470	1462743	10.3	0.12	0.0584	0.0007		596	6	544	26	-9.5
P19-B-82	0.23	178752	10625	13200	14948	1963788	10.0	0.11	0.0587	0.0007		617	7	558	27	-10.6
P24-A-85	0.19	134893	8033	8988	11241	1570388	10.6	0.12	0.0589	0.0007		583	6	562	25	-3.9
P24-B-86	0.19	215416	12678	13531	19129	2579578	10.9	0.12	0.0582	0.0007		568	6	535	25	-6.1
P24-C-87	0.23	190156	11203	14574	16672	2257808	10.8	0.12	0.0582	0.0007		573	6	538	25	-6.5
P25-A-88	0.12	186230	10895	6820	15772	2045956	10.0	0.11	0.0578	0.0007		617	7	523	25	-18.0
P25-B-89	0.13	149846	8929	7137	12817	1813248	11.0	0.12	0.0589	0.0007		562	6	563	25	0.1
P27-A-90	0.28	275077	15952	22837	23687	2926224	9.6	0.11	0.0573	0.0006		636	7	503	24	-26.4
P27-B-91	0.17	67850	3969	3966	5988	845198	11.3	0.13	0.0578	0.0007		547	6	522	28	-4.7
P28-A-94	0.18	67221	3922	4115	5873	820143	11.1	0.12	0.0577	0.0007		558	6	517	28	-8.0
P28-B-95	0.25	108634	6380	9218	9565	1327840	11.1	0.12	0.0580	0.0007		557	6	531	27	-4.9
P30-A-96	0.25	153628	9165	13345	13020	1812773	10.7	0.12	0.0590	0.0007		576	6	566	25	-1.8
P30-B-97	0.18	75224	4443	4451	6511	899448	10.8	0.12	0.0584	0.0008		569	6	544	28	-4.6
P31-A-98	0.18	124606	7372	7636	10154	1409025	10.3	0.11	0.0585	0.0007		600	6	548	26	-9.6
P31-B-99	0.27	219540	12828	19789	17319	2379395	9.8	0.11	0.0578	0.0007		625	7	520	25	-20.1
P31-C-113	0.20	156151	9100	11227	13055	1820812	10.6	0.12	0.0576	0.0007		583	6	514	25	-13.3
P33-A-101	0.32	56963	3332	6203	4481	634144	10.1	0.11	0.0578	0.0008		609	7	522	29	-16.6
P33-B-102	0.19	32990	1916	2203	3029	414690	11.4	0.13	0.0574	0.0009		542	6	507	33	-6.9
P38-A-103	0.18	106456	6287	6464	9085	1256979	10.7	0.12	0.0584	0.0007		576	6	544	26	-5.9
P38-B-104	0.17	67147	3970	3947	5966	830583	11.2	0.13	0.0584	0.0008		551	6	546	29	-0.8
P39-A-105	0.20	102522	6080	7104	8880	1244751	11.0	0.12	0.0586	0.0007		560	6	553	26	-1.4
P39-B-106	0.18	72196	4215	4456	6378	897673	11.3	0.13	0.0577	0.0008		548	6	518	29	-5.7
P41-A-62	0.30	279459	16437	24660	23869	2917691	9.5	0.10	0.0581	0.0006		647	7	534	24	-21.2
P41-B-108	0.17	72943	4242	4412	7162	998684	12.4	0.14	0.0575	0.0007		499	5	509	28	2.0
P44-A-109	0.19	122178	7192	8212	9598	1350975	10.0	0.11	0.0582	0.0007		613	7	536	26	-14.3
P44-B-110	0.36	106626	6317	13134	9396	1311657	11.2	0.12	0.0586	0.0007		553	6	550	26	-0.5
P44-C-111	0.21	62588	3733	4641	5456	758855	11.0	0.12	0.0590	0.0008		561	6	565	28	0.7
O4-A-4	0.15	75279	4453	4050	7707	1086785	12.7	0.15	0.0583	0.0008		488	5	540	30	9.6
O4-B-5	0.24	178193	10314	12606	17406	2133854	10.5	0.12	0.0571	0.0006		584	6	493	25	-18.6
O4-C-6	0.22	241854	14111	16100	22872	2934413	10.7	0.12	0.0575	0.0006		577	6	510	24	-13.1
08-A-7	0.20	65999	3915	4515	6217	869370	11.6	0.13	0.0585	0.0008		533	6	547	29	2.6
O8-B-8	0.24	189268	11345	14141	17742	2277155	10.6	0.12	0.0591	0.0007		582	6	570	24	-2.1
O23-A-11	0.05	108360	6623	1785	9821	1251381	10.2	0.12	0.0602	0.0007		605	7	612	26	1.2
023-B-12	0.18	42758	2484	2803	4120	568087	11.7	0.14	0.0573	0.0009		529	6	502	34	-5.5
O24-A-13	0.17	85657	5010	5108	8088	1128741	11.6	0.13	0.0577	0.0007		533	6	516	28	-3.3
O24-B-14	0.29	299829	17789	25776	27691	3366411	9.9	0.11	0.0585	0.0006		621	7	548	24	-13.5
O25-A-15	0.18	67700	4112	4721	7217	1020042	13.3	0.15	0.0599	0.0009		469	5	599	32	21.7
O25-B-16	0.19	136882	8147	8156	13042	1683088	10.8	0.12	0.0587	0.0007		570	6	554	25	-2.8
O25-C-17	0.21	148915	8847	9579	14257	1779442	10.5	0.12	0.0586	0.0007		586	6	550	25	-6.4
O28-A-20	0.22	70479	4144	5333	6415	912834	11.4	0.13	0.0580	0.0008		542	6	527	29	-2.8
O28-B-21	0.18	60000	3531	3639	5385	764818	11.2	0.13	0.0580	0.0008		550	6	529	30	-4.0
O28-C-22	0.15	53880	3166	2863	5310	738182	12.1	0.14	0.0579	0.0010		514	6	526	36	2.4
O34-A-23	0.22	45676	2775	3300	3987	558826	10.8	0.13	0.0599	0.0011		573	7	599	37	4.5
O34-B-24	0.23	186138	11023	14752	17865	2500976	11.8	0.14	0.0584	0.0007		523	6	544	25	3.7
O35-A-27	0.30	258692	15361	23014	23727	2924472	9.9	0.11	0.0585	0.0006		617	7	549	24	-12.4
O35-B-28	0.19	173588	10212	10953	16148	2182180	11.1	0.13	0.0580	0.0007		558	6	529	25	-5.5
O35-C-29	0.18	57324	3398	3500	5296	741351	11.4	0.13	0.0584	0.0008		543	6	546	29	0.6
O38-A-30	0.22	128132	7582	9238	11264	1545103	10.6	0.12	0.0583	0.0007		581	6	541	26	-7.3
O38-B-31	0.18	70782	4145	4340	7109	1012582	12.6	0.15	0.0577	0.0008		493	6	519	32	5.0
O40-A-33	0.08	31161	1792	941	2654	370633	10.5	0.13	0.0567	0.0012		588	7	479	45	-22.7
O40-B-34	0.17	53672	3156	3246	4690	669541	11.0	0.13	0.0580	0.0008		562	6	528	30	-6.5
O40-C-35	0.29	80499	4701	7796	7636	1065012	11.6	0.13	0.0576	0.0007		531	6	513	27	-3.6
O32-36	0.19	158653	9389	10434	13866	1957399	10.9	0.12	0.0583	0.0007		568	6	541	26	-4.9
O33-37	0.01	52679	3127	139	4891	685248	11.4	0.13	0.0585	0.0008		540	6	549	30	1.7
O27-38	0.18	41321	2419	2533	4103	570164	12.1	0.14	0.0577	0.0009		510	6	518	33	1.5
O14-41	0.20	183083	10584	11890	17366	2293574	11.0	0.13	0.0570	0.0007		560	6	490	25	-14.2
O11-42	0.17	40443	2341	2351	3935	553468	12.0	0.14	0.0571	0.0009		514	6	493	33	-4.3
O10-A-43	0.18	62453	3582	3838	5683	799734	11.3	0.13	0.0565	0.0007		548	6	473	29	-16.0
O10-B-44	0.15	38973	2300	2007	3435	482535	10.9	0.13	0.0582	0.0009		566	6	536	34	-5.6
O9-45	0.01	56733	3295	227	5471	761176	11.8	0.14	0.0573	0.0008		524	6	501	29	-4.7
O1-46	0.08	57106	3438	1435	4876	687871	10.6	0.12	0.0593	0.0009		581	6	579	31	-0.3
I5-A-49	0.16	114676	6752	6586	9892	1457921	11.2	0.13	0.0580	0.0008		552	6	531	30	-4.0
I9-A-51	0.14	11535	708	690	846	117726	9.0	0.11	0.0606	0.0013		681	8	624	46	-9.1
I9-B-52	0.19	144791	8497	9084	14095	1933563	11.8	0.13	0.0578	0.0007		526	6	523	25	-0.6
I3-53	0.19	3336	216	208	273	38921	10.3	0.15	0.0641	0.0028		599	9	745	90	19.5
I4-54	0.01	57478	3499	362	4960	706494	10.8	0.13	0.0600	0.0010		570	6	604	36	5.6
I6-56	0.23	233050	13580	17226	20920	2692278	10.2	0.12	0.0574	0.0006		605	7	508	24	-19.1
I12-A-57	0.03	21566	1264	317	1806	253165	10.3	0.12	0.0578	0.0010		596	7	522	38	-14.1
I12-B-58	0.01	11827	721	75	1020	139527	10.4	0.13	0.0601	0.0013		593	7	608	47	2.5
I12-C-59	0.01	53979	3225	249	4867	687376	11.2	0.13	0.0589	0.0008		551	6	563	29	2.1
I15-A-60	0.18	57297	3373	3623	4817	675140	10.4	0.12	0.0580	0.0008		594	7	530	31	-11.9
I15-B-61	0.18	128938	7577	8161	12478	1772988	12.1	0.14	0.0579	0.0007		512	6	526	26	2.8
I18-A-65	0.01	50094	2930	268	4361	620766	10.9	0.13	0.0577	0.0008		566	6	517	30	-9.5
I19-67	0.01	53094	3177	133	4680	649061	10.8	0.13	0.0590	0.0008		573	6	566	30	-1.2
I21-68	0.02	45116	2659	289	4228	586338	11.4	0.13	0.0581	0.0009		540	6	533	32	-1.3
I22-A-71	0.01	4068	325	291	312	42636	9.2	0.13	0.0788	0.0028		664	9	1167	68	43.1
I22-B-72	0.18	46990	2768	2957	4445	610407	11.4	0.13	0.0581	0.0009		541	6	532	32	-1.7
I23-73	0.21	77827	4609	5627	7456	1048231	11.9	0.14	0.0584	0.0008		522	6	544	31	4.0
I24-74	0.14	408368	23739	16629	36783	4282147	9.2	0.11	0.0573	0.0006		663	7	502	23	-32.1
I25-75	0.20	164759	9714	10779	15563	2107884	11.3	0.13	0.0581	0.0007		549	6	533	26	-2.8